Spin-Orbit Coupling and Phosphorescence Rate of Dinuclear Iridium(III) Complexes

Dissertation

zur Erlangung des Doktorgrades der Naturwissenschaften (Dr. rer. nat.)
an der Fakultät für Chemie und Pharmazie
der Universität Regensburg

vorgelegt von

Marsel Z. Shafikov

2021

The dissertation was submitted: 22 July 2021

Date of the colloquium: 13 October 2021

The work was carried out at the University of Regensburg, Institute of Physical and Theoretical Chemistry, under the supervision of Dr. Rafał Czerwieniec.

Board of Examiners: Prof. Dr. Antje Bäumner (Chairman)

Dr. Rafał Czerwieniec (1st Referee)

Prof. Dr. Bernhard Dick (2nd Referee)

Prof. Dr. Manfred Scheer (Examiner)

Parts of this thesis have been published in

Shafikov, M. Z.; Martinscroft, R.; Hodgson, C.; Hayer, A.; Auch, A.; Kozhevnikov, V. N. Non-Stereogenic Dinuclear Ir(III) Complex with a Molecular Rack Design to Afford Efficient Thermally Enhanced Red Emission. *Inorg. Chem.* **2021,** *60*, 1780-1789.

Shafikov, M. Z.; Zaytsev, A. V.; Kozhevnikov, V. N. Halide-Enhanced Spin-Orbit Coupling and the Phosphorescence Rate in Ir(III) Complexes. *Inorg. Chem.* **2021,** *60*, 642–650.

Shafikov, M. Z.; Zaytsev, A.; Suleymanova, A. F.; Brandl, F.; Kowalczyk, A.; Gapinska, M.; Kowalski, K.; Kozhevnikov, V. N.; Czerwieniec, R. Near Infrared Phosphorescent Dinuclear Ir(III) Complex Exhibiting Unusually Slow Intersystem Crossing and Dual Emissive Behavior. *J. Phys. Chem. Lett.* **2020,** *11*, 5849-5855.

Shafikov, M. Z.; Daniels, R.; Kozhevnikov, V. N. Unusually Fast Phosphorescence from Ir(III) Complexes via Dinuclear Molecular Design. *J. Phys. Chem. Lett.* **2019,** *10*, 7015-7024.

Shafikov, M. Z.; Tang, S.; Larsen, C.; Bodensteiner, M.; Kozhevnikov, V. N.; Edman, L. An Efficient Heterodinuclear Ir(III)/Pt(II) Complex: Synthesis, Photophysics and Application in Light-Emitting Electrochemical Cells. *J. Mater. Chem. C* **2019,** *7*, 10672-10682.

Further publications

Shafikov, M. Z.; Suleymanova, A. F.; Kutta, R. J.; Brandl, F.; Gorski, A.; Czerwieniec, R., Dual Emissive Dinuclear Pt(II) Complexes and Application to Singlet Oxygen Generation. *J. Mater. Chem. C* **2021,** *9*, 5808-5818.

Shafikov, M. Z.; Pander, P.; Zaytsev, A. V.; Daniels, R.; Martinscroft, R.; Dias, F. B.; Williams, J. A. G.; Kozhevnikov, V. N. Extended Ligand Conjugation and Dinuclearity as a Route to Efficient Platinum-based Near-infrared (NIR) Triplet Emitters and Solution-processed NIR-OLEDs. *J. Mater. Chem. C* **2021,** *9*, 127-135.

Shafikov, M. Z.; Daniels, R.; Pander, P.; Dias, F. B.; Williams, J. A. G.; Kozhevnikov, V. N. Dinuclear Design of a Pt(II) Complex Affording Highly Efficient Red Emission: Photophysical Properties and Application in Solution-Processible OLEDs. *ACS Appl. Mater. Interfaces* **2019,** *11*, 8182-8193.

Shafikov, M. Z.; Brandl, F.; Dick, B.; Czerwieniec, R. Can Coumarins Break Kasha's Rule? *J. Phys. Chem. Lett.* **2019,** *10*, 6468-6471.

Shafikov, M. Z.; Suleymanova, A. F.; Schinabeck, A.; Yersin, H. Dinuclear Ag(I) Complex Designed for Highly Efficient Thermally Activated Delayed Fluorescence. *J. Phys. Chem. Lett.* **2018,** *9*, 702-709.

Shafikov, M. Z.; Suleymanova, A. F.; Czerwieniec, R.; Yersin, H. Design Strategy for Ag(I)-Based Thermally Activated Delayed Fluorescence Reaching an Efficiency Breakthrough. *Chem. Mater.* **2017,** *29*, 1708-1715.

Shafikov, M. Z.; Suleymanova, A. F.; Czerwieniec, R.; Yersin, H. Thermally Activated Delayed Fluorescence from Ag(I) Complexes: A Route to 100% Quantum Yield at Unprecedentedly Short Decay Time. *Inorg. Chem.* **2017,** *56*, 13274-13285.

Yersin, H.; Czerwieniec, R.; **Shafikov, M. Z.**; Suleymanova, A. F. TADF Material Design: Photophysical Background and Case Studies Focusing on Cu(I) and Ag(I) Complexes. *ChemPhysChem* **2017,** *18*, 3508-3535.

Shafikov, M. Z.; Suleymanova, A. F.; Kozhevnikov, D. N.; König, B. Tuning the Excimer Emission of Amphiphilic Platinum(II) Complexes Mediated by Phospholipid Vesicles. *Inorg. Chem.* **2017,** *56*, 4885-4897.

Shafikov, M. Z.; Kozhevnikov, D. N.; Bodensteiner, M.; Brandl, F.; Czerwieniec, R. Modulation of Intersystem Crossing Rate by Minor Ligand Modifications in Cyclometalated Platinum(II) Complexes. *Inorg. Chem.* **2016,** *55*, 7457-7466.

Kozhevnikov, D. N.; Kozhevnikov, V. N.; **Shafikov, M. Z.**; Prokhorov, A. M.; Bruce, D. W.; Williams, J. A. Phosphorescence vs Fluorescence in Cyclometalated Platinum(II) and Iridium(III) Complexes of (Oligo)thienylpyridines. *Inorg. Chem.* **2011,** *50*, 3804-3815.

Patent

Yersin, H.; Czerwieniec, R.; **Shafikov, M. Z.**; Suleymanova, A. F. Silberkomplexe mit nido-Carboran-Liganden mit thermisch-aktivierter verzögerter Fluoreszenz für opto-elektronische Vorrichtungen. Patent DE 10 2016 115 633.7, **2016**

Table of Contents

Introduction

Materials emitting light in the visible optical range have been attracting attention reportedly since the Middle Ages.[1] The nature of the phenomenon, however, eluded investigators' understanding until after the theory of quantum mechanics has been established. It was then that the electronic composition of the polyatomic molecules could be modelled to have electronic configurations corresponding to states of different energies and to predict transitions between those states.[2]

A higher state can relax to a lower state radiatively with the release of a quantum of light (photon emission)[3] of the wavelength corresponding to the energy difference between the two states. Such emission of light in the optical range from ultraviolet to infra-red, which includes visible light, is called *luminescence* (from Greek *lumen*, meaning light). Typically, luminescence occurs with the transition between the lowest energy excited state of a certain multiplicity and the state of the lowest possible energy (ground state) of the molecule as relaxation processes between different excited states typically take ultrafast non-radiative paths.[4]

A molecule in the ground state can be agitated to populate its luminescent excited state via different excitation mechanisms. Luminescence occurring after optical excitation, by absorbing a photon upon the irradiation with light of appropriate wavelength, is termed *photoluminescence*[5], whereas luminescence occurring after electroexcitation, by injecting the electricity-driven hole and electron, is termed *electroluminescence*[6,7].

The characteristics of luminescence deal with the quantum mechanical allowedness of the corresponding electronic transition which is subject to selection rules. For instance, one such rule is the spin-selection rule, stating that the total spin of the electronic state (S, sum of all the electronic spins in the molecule) should not change upon the transition ($\Delta S = 0$), allows transitions between the states of the same multiplicity ($M = 2S + 1$) and forbids (in zeroth order) those between the states of different multiplicities, such as singlet ($S = 0$, $M = 1$) and triplet ($S = 1$, $M = 3$). Therefore, spin-forbidden transitions are much slower compared to the transitions with no restrictions from the selection rules. Indeed, the luminescence associated with spin-allowed transition, called *fluorescence*, typically has a decay time in the order of nanoseconds which is several orders of magnitude shorter (faster) compared to that of luminescence occurring at the spin-forbidden transition called *phosphorescence*. The decay time of phosphorescence spans from microseconds to seconds and strongly depends on the perturbation effects, such as spin-orbit coupling (SOC), that can relax the $\Delta S = 0$ rule.

The vast majority of strongly luminescent organic molecules and their complexes with metals, stable under ambient conditions, have closed-shell electronic configuration of the ground state which therefore has singlet multiplicity (S_0). Consequently, the luminescence of such compounds

can stem either from the lowest excited singlet state (S_1, one possible mutual orientation of the spins of two unpaired electrons), $S_1 \rightarrow S_0$ fluorescence, or from the lowest excited triplet state (T_1, three possible mutual orientations of the spins of two unpaired electrons), $T_1 \rightarrow S_0$ phosphorescence. It was understood that a heavy atom, such as a transition metal, in the chromophoric molecule can induce a strong spin-orbit coupling[8] to enhance the population of the lowest triplet state and make the subsequent phosphorescence $T_1 \rightarrow S_0$ efficient under ambient conditions. This stimulated the researchers to investigate the molecular design principles affording phosphorescent transition metal complexes and the application venues that would allow exploiting the properties of T_1 state and the relatively long, compared to the non-forbidden $S_1 \rightarrow S_0$ fluorescence, decay time of $T_1 \rightarrow S_0$ phosphorescence.

Nowadays, phosphorescent materials are applied in different areas. One application field is phosphorescent bio-imaging.[9,10] Phosphorescent metal complexes, featuring specifically designed structures, can accumulate in and lit up targeted cell organelles with the relatively long decay time of phosphorescence allowing time-resolved cut-off of the background fluorescence of the biological tissues.[11] Another application of the phosphorescent materials is inspired by the sensitivity of phosphorescence's intensity to molecular dioxygen, which, interacting with the T_1 state, brings about additional non-radiative $T_1 \rightarrow S_0$ relaxation processes. This allows mapping the oxygen concentration and is utilized to measure the oxygenation of biological tissues.[12] Moreover, the oxygen quenching typically occurs with energy transfer to the ground state (triplet, T_0) oxygen and thus generates very reactive oxygen molecules in the excited singlet state – *singlet oxygen.* Therefore, phosphorescent sensitizers of singlet oxygen are also used in photodynamic therapy as combined with bioimaging.[13] It is noteworthy that phosphorescent bio-imaging probes are often designed to emit in the red optical range where the biological tissues are more transparent than in shorter wavelengths.

The major research driving interest in the design of new efficient phosphorescent materials, though, was ignited relatively recently by the fast-growing application field of Organic Light Emitting Diodes (OLEDs). The first OLED devices of multilayer design were built using fluorescent emitters, in particular tris(8-hydroxyquinolinato)aluminium (Alq_3).[6] Fluorescent emitter materials could utilize only the singlet excitons (bound electron-hole pairs), which is just 25 % of all the excitons formed in the emitting layer as, according to the spin-statistics, the holes and electrons with initially uncorrelated spins form singlet and triplet excitons in the ratio of 1:3. The triplet excitons, 75% of all, in such devices are lost and their energy is dissipated as the heat. This, apart from the low device efficiency, also causes fast degradation of the emitting layer which strongly limited the commercial success of fluorescent OLEDs. The challenge of improving the internal efficiency of OLEDs was addressed in the groundbreaking work of Thompson and co-

workers who suggested using phosphorescent emitters instead of fluorescent ones.[7] It was shown that phosphorescent emitters can utilize 100 % of the formed excitons by converting the singlet excitons to triplet excitons in the course of the *intersystem crossing* (ISC) process and utilize all the excitons via $T_1 \rightarrow S_0$ phosphorescence. Efficient ISC and phosphorescence, however, require a SOC of state T_1 with singlet states that is fulfilled in complexes of transition metal complexes, such as Ir(III) complexes. Those complexes, therefore, became the main group of phosphorescent materials utilized in today's most efficient OLED devices.

An actual challenge, in the design of the next generation of phosphorescent materials, is increasing the radiative rate (k_r) of $T_1 \rightarrow S_0$ transition (or decreasing radiative decay time), while keeping a high ratio of radiative to non-radiative relaxation rates, (k_r/k_{nr}) that ensures a high emission quantum yield. Conventional phosphors with the highest radiative rates, representing mononuclear Ir(III) complexes, are characterized with the shortest radiative decay times of the emitting state (T_1) down to 1.5 μs[14]. Materials with larger k_r values would result in a larger number of emitted photons per unit of time since the cycle of excitation and emission would become faster. Applied in bio-imaging, this would afford a higher imaging brightness and/or reduction of the probe's concentration. Applied in an OLED, a faster emitter would help to counter the efficiency roll-off at high electrical currents through the diode and thus afford higher brightness without compromising the efficiency. It is worth noting that a simple increase of the emitter's concentration in the emitting layer of OLED, as to handle more excitons per unit of time, is fraught with an increase of triplet-triplet annihilation rate which also diminishes the device's efficiency.

The development of design approaches to new efficient phosphors with enhanced radiative rates is of especial interest for materials working in the longer wavelengths optical range (red, near infra-red). This is because the relatively low energy of the emitting state in such case is accompanied with (i) a relatively small Einstein's coefficient of spontaneous emission, which is proportional to the inverse of the cube of the emission wavelength $(1/\lambda^3)^3$; (ii) higher non-radiative relaxation rates due to the stronger vibrational overlap with the ground state as stated by the energy gap law.[15] The vibrational overlap of the emitting and ground states, defined by the Frank-Condon factor, can be tuned through the rigidity of molecular structure which is the typical approach to increase the emission quantum yields of red-emitting complexes. On the other hand, increasing the radiative rate, despite the relatively low Einstein's coefficient of spontaneous emission, requires to deal with the electronic factor to increase the oscillator strength of $T_1 \rightarrow S_0$ transition, $f(T_1 \rightarrow S_0)$, and is often left without due attention.

It was shown in recent years that the dinuclear design of metal complexes, in particular Ir(III) and Pt(II), can afford enhancement of the $f(T_1 \rightarrow S_0)$ value over the mononuclear analogues, and show relatively red-shifted and faster phosphorescence.[16,17] It was suggested that this might be due

to the additional SOC paths of state T_1 with singlets, brought by the second metal ion. However, SOC is a short-range phenomenon with its strength proportional to the fourth power of the nucleus' charge (Z^4) and to the inverse of the cube of the distance to the nucleus ($1/r^3$) and thus can be efficient only very close at a heavy atom with a large SOC constant.[18] Therefore, it is mechanistically unclear how separate metal centers within one molecule could cooperate to enhance the SOC of state T_1 with singlet states. Meanwhile, a profound understanding of such cooperation and investigation of its dependencies are essential for the elaboration of design principles targeted to the next generation of efficient and fast phosphors. A systematic study of interconnection between electronic structure and photophysical properties of dinuclear complexes, conducted in comparison to the mononuclear analogues, might help to gain such understanding and therefore is the objective and motivation of the present work.

In Chapter 1 a comparative study of two analogous Ir(III) complexes, featuring mono- and dinuclear design, is carried out by means of steady-state optical spectroscopy and density functional theory. It is shown that electronic coupling of the two coordination sites in the dinuclear complex doubles the number of excited singlet states suited for SOC with the state T_1, compared to the mononuclear complex, and thus enhances the rate of phosphorescence.

Chapter 2 investigates the analogue of the dinuclear structure from Chapter 1 with the iodides instead of chlorides. It is shown that the metal coordinated halides, unlike the organic ligands, contribute to SOC of the state T_1 with singlet states along with the metals, and, upon exchange of chlorides for iodides, the importance of halide induced SOC exceeds even that of the metal centers.

In Chapter 3 the design of the bridging chromophoric ligand is investigated as a tool to red-shift the phosphorescence of the Ir(III) dinuclear complex. Using a chromophoric ligand of strongly π-excessive character indeed shifted the phosphorescence to far-red and near-infrared optical ranges, but it also resulted in a significantly reduced metal contribution to the highest occupied molecular orbital (HOMO) of the complex. Consequently, due to the weak SOC of state T_1 with singlets, the phosphorescence rate of the complex is rendered low.

Chapter 4 investigates the utilization of a ditopic bis-tridentate bridging ligand of π-deficient electronic character to prepare a highly efficient red-emitting dinuclear Ir(III) complex. It is demonstrated that the dinuclear complex affords strongly red-shifted and yet a few times faster phosphorescence than the mononuclear analogue.

Chapter 5 investigates a hetero-dinuclear Ir(III)/Pt(II) complex, where Pt(II) and Ir(III) metal centers are bridged by a chromophoric ligand of π-deficient electronic character. The introduction of a Pt(II) center, in addition to Ir(III), afforded significant expansion of the chromophoric system, due to its square-planar geometry, and also introduced an additional SOC center. As a result, the material shows highly efficient red-phosphorescence with sub-microsecond radiative decay time.

1. Phosphorescence rates of mononuclear and dinuclear Ir(III) complexes with metal coordinated chlorides

A few works published in recent years demonstrated the dinuclear molecular design of transition metal complexes as advantageous to enhance the rate and efficiency of phosphorescence.[16,17] Although the effect was linked to the additional SOC brought by the second metal ion, no detailed investigation from the electronic structure perspective was carried out. For instance, one of the pioneering works by Kozhevnikov and co-workers only stated -*" The consistency with which k_r is enhanced in our recently studied multinuclear complexes featuring such bis-cyclometallating ligands supports the notion that spin–orbit coupling pathways may be enhanced by the presence of a second heavy metal center"*[17]- without any mechanistic details (k_r - radiative rate).

To understand the electronic nature of the effect, a comparative study involving analogous mono- and dinuclear Ir(III) complexes **IrCl** and **Ir_2Cl_2** (Chart 1.1) was carried out.

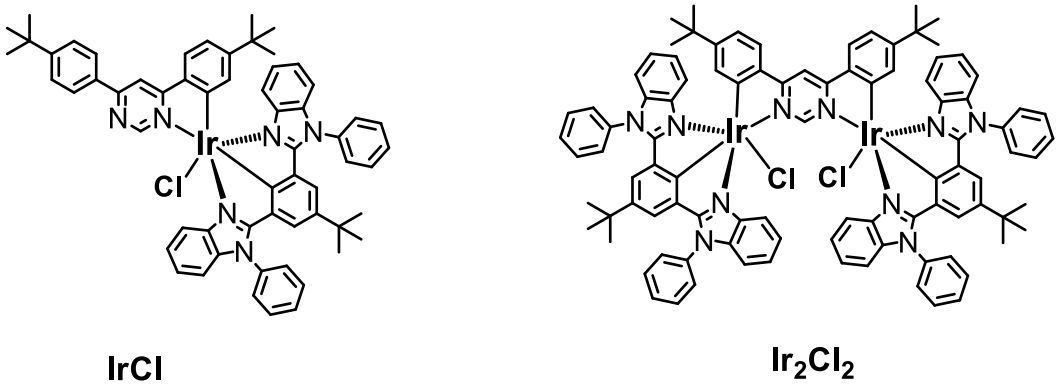

Chart 1.1 Chemical structures of mononuclear complex **IrCl** and dinuclear complex **Ir_2Cl_2**. For synthetic details see ref.[19]

1.1 X-ray diffraction analysis. The x-ray quality crystals of both **IrCl** and **Ir_2Cl_2** were obtained by slow convectional diffusion of methanol into a dichloromethane solution of the complex. The detailed description of the x-ray diffraction analyses and the data obtained are given in the Experimental (Section 7.6, Table 7.1). The x-ray determined molecular structures are shown in Figure 1.1. The crystal of **IrCl** has an asymmetric unit cell containing two independent molecules. However, the geometrical parameters of the two molecules are nearly identical (Table 8.1 in Supplementary Information), and further only one of them will be referred (Molecule 1 in Table 8.1). The coordination center of **IrCl** has an octahedral geometry, as expected for an Ir(III) complex. Due to a strong *trans* influence exerted by the metalated carbon atoms, the coordinated carbons of the two organic ligands are positioned in *cis* configuration to each other.[20] The N^C^N ligand (1,3-bis(N-phenylbenzimidazolyl)-5-*tert*-butylbenzene derivative – Phbib) is coordinated

with Ir–N3 and Ir–N4 bond lengths of 2.049 Å and 2.059 Å, respectively, and with a shorter Ir–C10 bond length of 1.945 Å. The ditopic C^N ligand (4,6-di-(4-tert-butylphenyl)pyrimidine derivative – dpp) features slightly longer coordination bonds with Ir−C1 and Ir−N1 bond lengths of 2.011 Å and 2.152 Å, respectively. The chloride ion is positioned *trans* to the metalated carbon of the dpp ligand (C1), with an Ir–Cl bond length of 2.458 Å. The phenyl substituents of the diazoles of the Phbib ligand are twisted from the ligand's plane by 59-80 degrees.

The geometry parameters of the two coordination centers of complex **Ir_2Cl_2** overall are similar to those found for the coordination center of complex **IrCl**. The Phbib1 and Phbib2, the two N^C^N ligands coordinated to Ir1 and Ir2 respectively, are sterically hindered by each other, thus slightly twisting the bridging dpp ligand and the whole molecular geometry out of C_{2v} point group symmetry. A comprehensive list of coordination center geometry parameters is given in the Supplementary Information (Section 8.2, Table 8.2).

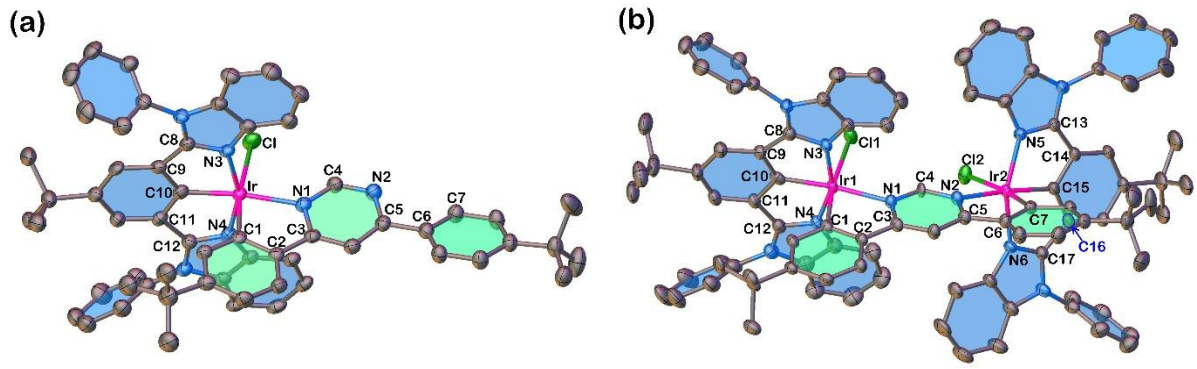

Figure 1.1. The XRD determined molecular structure of complex **IrCl** (a) and complex **Ir_2Cl_2** (b). Thermal ellipsoids are shown at the 50% probability level, and hydrogen atoms are omitted for clarity. (cf. ref.[19])

1.2 Optical spectroscopy. The absorption spectrum of **IrCl** in toluene ($c \approx 10^{-5}$ M) spans the optical range of $550 \geq \lambda_{abs} \geq 280$ nm (Figure 1.2a). With the help of TD-DFT calculations, the lower intensity bands ($\varepsilon < 1\times10^4\ M^{-1}cm^{-1}$) appearing at $550 \geq \lambda_{abs} \geq 450$ nm are assigned to the transitions of predominant metal to ligand charge transfer (MLCT) plus halide to ligand charge transfer (XLCT) characters. A relatively weak spatial overlap of the orbitals localized on the metal and the halide with the orbitals localized on the chromophoric (organic) ligand rationalize the relatively low intensity of these bands. The absorption bands of relatively higher intensity at $450 \geq \lambda_{abs} \geq 350$ nm are assigned to transitions carrying larger ligand centered (LC, $\pi\rightarrow\pi^*$), character admixtures to MLCT and XLCT. The highest intensity bands at $\lambda_{abs} < 350$ nm are assigned to the transitions of predominant LC that are localized on the Phbib and dpp ligands.

Complex **Ir$_2$Cl$_2$** in toluene shows an absorption spectrum of a similar shape compared to that of **IrCl** (Figure 1.2b). The relative red shift of the absorption bands of **Ir$_2$Cl$_2$** is probably due to the presence of the second coordination center that expands the conjugation system of the bridging (dpp) ligand. Similarly to the case of **IrCl**, absorption bands of **Ir$_2$Cl$_2$** of longer wavelengths ($580 \leq \lambda_{abs} \leq 480$) and lower intensity ($\varepsilon < 2\times10^4\ M^{-1}cm^{-1}$) are assigned to transitions of predominant MLCT+XLCT character; the middle-range bands ($480 \leq \lambda_{abs} \leq 480$) are assigned to the transitions with higher LC character admixtures; the intense bands at $\lambda_{abs} < 350$ are assigned to the transitions of predominant LC character.

It is noteworthy, that the charge transfer character absorption bands, appearing at the longer wavelength end of the spectrum, are several times more intense in the case of **Ir$_2$Cl$_2$** compared to **IrCl**. This difference can be explained by the (*quasi*)-symmetric structure of the dinuclear complex and is more closely considered in Chapter 4.

Both complexes show intense $T_1 \rightarrow S_0$ phosphorescence with the spectral maxima at λ_{max} = 558 nm with a vibrational shoulder at λ = 605 nm for **IrCl** and at λ_{max} = 575 nm with a vibrational shoulder λ = 618 nm for **Ir$_2$Cl$_2$**, as measured in degassed toluene ($c \approx 10^{-5}$ M) at room temperature (Figure 1.2). Spectral overlap of absorption and emission in both cases shows the close energy proximity of the emitting state T_1 and to the state S_1 and also to the whole manifold of excited singlet states. A small energy separation $\Delta E(S_1{-}T_1)$ indicates a weak exchange interaction in the electronic configuration of states S_1 and T_1 (both of HOMO→LUMO origin, Table 8.5), which agrees well with the predominant charge transfer character of the lowest excited states.

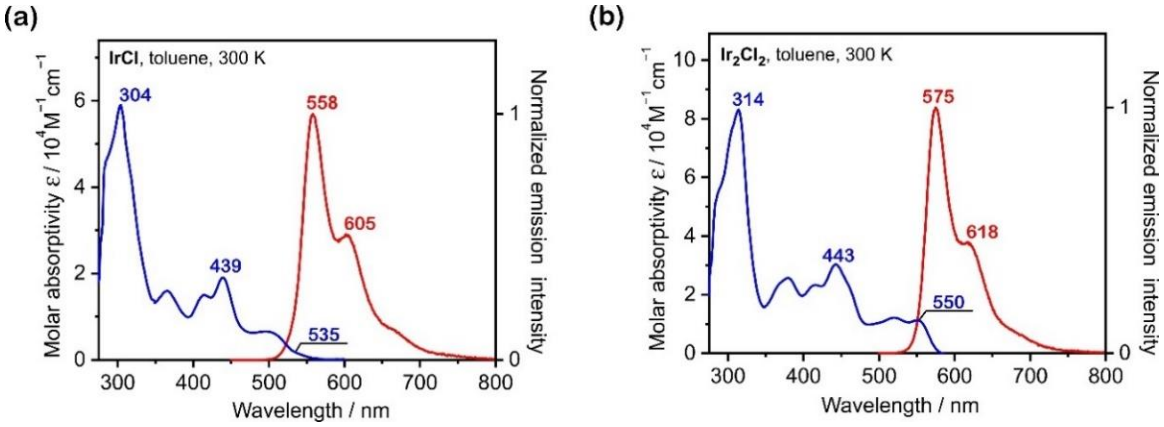

Figure 1.2. Absorption (blue) and emission (red) spectra of **IrCl** (a) and **Ir$_2$Cl$_2$** (b) at room temperature in toluene. (cf. ref.[19])

The room temperature emission quantum yields obtained for the degassed toluene solutions ($c \approx 10^{-5}$ M) amount to Φ_{PL} = 0.90 (90 %) for **IrCl** and Φ_{PL} = 0.95 (95 %) for **Ir$_2$Cl$_2$** with the corresponding emission decay times τ = 1.16 μs for **IrCl** and a notably shorter value of τ = 0.44

μs for dinuclear **Ir_2Cl_2** (Figure 1.3). The resulting radiative rate $k_r = 0.78\times10^6$ s^{-1} of **IrCl**, calculated as $k_r = \Phi_{PL}/\tau$, is a high value for phosphorescence although still comparable to other mono-nuclear Ir(III) complexes. The almost three times larger value $k_r = 2.27\times10^6$ s^{-1} of the dinuclear **Ir_2Cl_2**, on the other hand, is remarkable. Along with the k_r value, the non-radiative $T_1 \rightarrow S_0$ relaxation rate, calculated as $k_{nr} = (1-\Phi_{PL})/\tau$, assuming a unit population of the T_1 state, also increases from $k_{nr} = 0.86\times10^5$ s^{-1} for **IrCl** to $k_{nr} = 1.10\times10^5$ s^{-1} for **Ir_2Cl_2**. It is noted, however, that k_r/k_{nr} ratio is still smaller in the dinuclear **Ir_2Cl_2** that afford the relatively larger quantum yield. The numerical data for the photophysical properties of **IrCl** and **Ir_2Cl_2** are summarized in Table 1.1.

Table 1.1. Summary of key photophysical properties of **IrCl** and **Ir_2Cl_2** in diluted toluene solution ($c \approx 10^{-5}$ M). The absorption spectrum was measured under ambient conditions. The ambient temperature (T = 300 K) emission decay time and quantum yield values were measured for a degassed sample. (cf. ref.[19])

	IrCl	**Ir_2Cl_2**
Absorption λ_{max}/nm (ε/$M^{-1}cm^{-1}$)	496 (6590), 439 (19050), 415 (14980), 365 (15960), 304 (58970).	550 (11300), 520 (12100), 443 (30300), 415 (23260), 380 (25640), 300 (82540).
Photoluminescence at T = 300 K		
λ_{max}/nm	558, 605	575, 618
τ (τ_r)/μs*	1.16 (1.29)	0.44 (0.46)
Φ_{PL}/%	90	95
$k_r/10^6$ s^{-1}	0.78	2.27
$k_{nr}/10^5$ s^{-1}	0.86	1.10
Photoluminescence at T = 77 K		
λ_{max}/nm	543, 590, 645	565, 612
τ (τ_r)/μs*	2.40 (3.20)	2.50 (2.50)
Φ_{PL}/%	75	100

*τ_r – radiative decay time calculated as $\tau_r = \tau/\Phi_{PL} = 1/k_r$

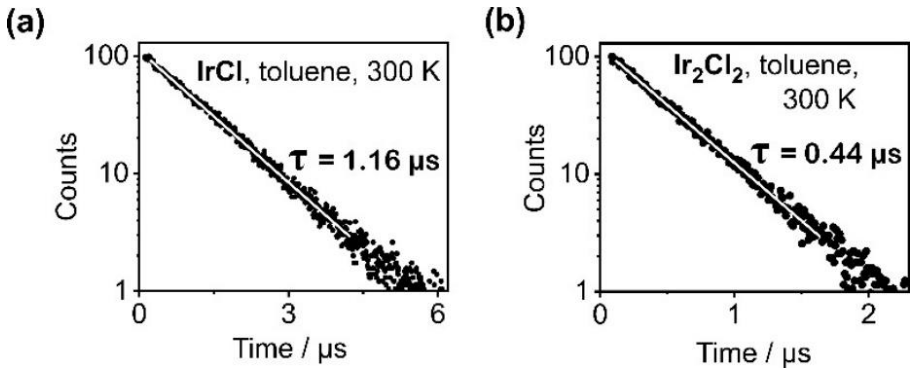

Figure 1.3. (a) emission decay curve of complex **IrCl** (a) and of complex **Ir$_2$Cl$_2$** (b) in degassed toluene ($c \approx 10^{-5}$ M) at T = 300 K. The white lines on the black experimental data points represent the best fit of mono-exponential decay function. (cf. ref.[19])

The larger k_r and k_{nr} values of **Ir$_2$Cl$_2$**, compared to those of **IrCl**, are experimental evidence of a more relaxed spin selection rule $\Delta S = 0$ (S – total spin of a state involved in the transition) for $T_1 \rightarrow S_0$ transition. The $\Delta S = 0$ selection rule, forbidding the $T_1 \rightarrow S_0$ phosphorescence, is relaxed by the SOC of the T_1 state with the singlet states (See section 8.1 for more detail). The more efficient the SOC, the faster the phosphorescence. Therefore, according to the obtained phosphorescence rates, the T_1 state of complex **Ir$_2$Cl$_2$** probably undergoes a significantly stronger SOC with the singlet states than that of complex **IrCl**. The extend of SOC of the T_1 state with other states (singlet and triplet) can be assessed via the Zero-Field Splitting of its substates I, II and III, and the individual emission rates of the substates indicate the relative amount of singlet admixture to each. Due to the SOC induced ZFS of state T_1, the population of its substates I, II, and III is different and depends on temperature. At relatively large values of T_1 state ZFS (ZFS ≥ 10 cm^{-1}), this effect can be traced by measuring the emission decay times as a function of temperature at cryogenic temperatures. Analyzing the thus obtained data one can estimate the individual characteristics of T_1 substates – a methodology developed by H. Yersin et al.[21-26]

The emission decay times of **IrCl** in toluene ($c \approx 10^{-5}$ M) were measured in the temperature range $1.7 \leq T \leq 120$ K where the solvent remains a frozen glass. At temperature T = 1.7 K, **IrCl** shows emission with a long decay time of $\tau(1.7K) = 97.6$ µs, assigned to the lowest substate I, $I \rightarrow S_0$. It is noted that the observed slight deviation of the decay curve from the mono-exponential profile at a short time range is related to Spin-Lattice Relaxation (SLR) processes[27,28], indicating a slow thermal relaxation of higher T_1 substates at T = 1.7 K (Figure 1.1a). This effect weakens quickly with an increase of temperature and is not observed already at T = 5 K. The emission decay time of **IrCl** decreases very steeply with an increase of temperature above T = 1.7 K. This is due to the thermal population of substate II and opening of the $II \rightarrow S_0$ relaxation channel. The decrease becomes less steep in the temperature range of $8 \text{ K} \leq T \leq 12$ K, where the decay time of substates

I and II reaches an average value of τ(10 K) = 39 μs. A further increase in temperature is followed by further shortening of the emission decay time due to the thermal population of substate III and activation of the III→S_0 channel. At T = 120 K the emission decay times reaches the value τ(120 K) = 1.6 μs. The obtained temperature dependence of the emission decay time can be analyzed with Eq. 1.1, describing the thermal population of higher substates via Boltzmann type relation: [21,23,25,29,30]

$$\tau(T) = \frac{1+ \exp\frac{-\Delta E(II-I)}{k_B T}+\exp\frac{-\Delta E(III-I)}{k_B T}}{\frac{1}{\tau(I)}+\frac{1}{\tau(II)}\exp\frac{-\Delta E(II-I)}{k_B T}+\frac{1}{\tau(III)}\exp\frac{-\Delta E(III-I)}{k_B T}} \qquad (1.1)$$

Here τ(I), τ(II), τ(III) are the lifetimes of triplet substates I, II and III, respectively; ΔE(II−I) and ΔE(III−I) are the energy gaps between substates II and I, and substates III and I, respectively; T is the temperature; k_B is the Boltzmann constant. Eq. 1.1 was fitted to the measured decay time values of **IrCl** in the temperature range 1.7K ≤ T ≤ 120 K, with parameter τ(I) fixed to the experimental value obtained at T = 1.7 K of τ(1.7 K) = 97.6 μs.

The best fit suggests the individual substate II and III decay times of τ(II) = 17 μs and τ(II) = 0.35 μs and energy gaps ΔE(II−I) = 5 cm^{-1} and ΔE(III−I) = 65 cm^{-1}. Extrapolated to the room temperature conditions (T = 300 K) with Eq. 1.1, the obtained T_1 state parameters give an average decay time of τ_{av} = 1.25 μs, which is close to the experimentally measured value of τ(300 K) = 1.16 μs obtained for **IrCl** in degassed toluene.

The dinuclear complex **Ir_2Cl_2** was also investigated at cryogenic temperatures. The emission decay time of **Ir_2Cl_2** at T = 1.7 K is τ(1.7 K) = 8.2 μs. This value is constant up to a temperature T = 3 K and is assigned to the individual decay time of T_1 substate I, τ(I) = 8.2 μs. The further increase in temperature is accompanied by a decrease in the emission decay time due to thermal activation of the II→S_0 channel. In the temperature range 12 K ≤ T ≤ 30 K, the decay times do not change strongly and form a quasi-plateau with an average I/II→S_0 decay time of τ(23 K) = 7.8 μs. The relaxation channel associated with the third substate of state T_1, III→S_0, is activated at temperatures above T = 30 K, and with an increase of temperature up to T = 120 K, the emission decay time decreases down to τ(120 K) = 1.0 μs. The increasing population of the higher energy triplet substates at higher temperatures and their contribution to T_1→S_0 emission is also traced in a slight blue shift of emission spectra from T = 1.7 K to T = 77 K (Figure 1.5).

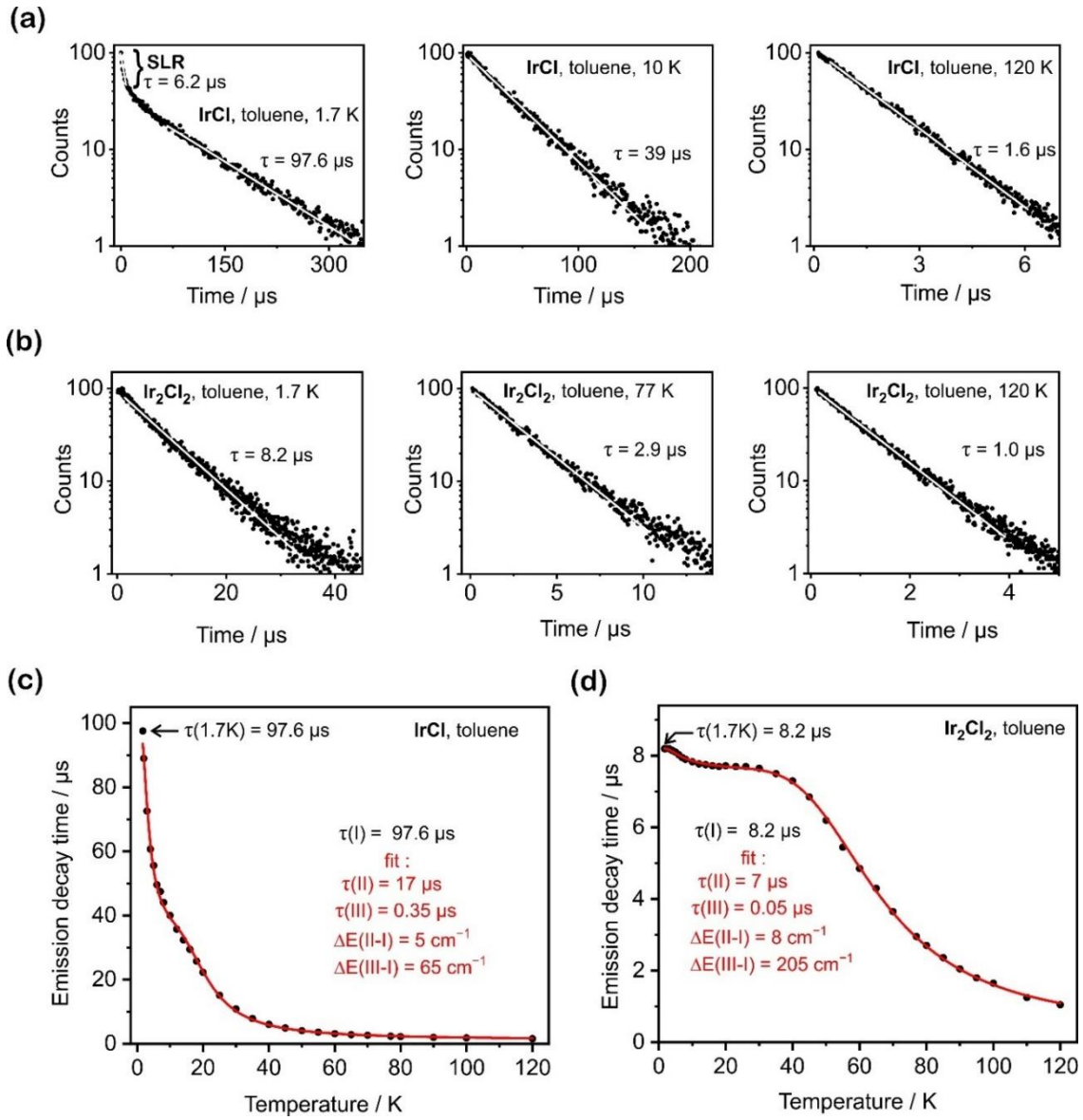

Figure 1.4. (a) Fitted emission decay curves of **IrCl** in toluene at the temperatures specified in the insets. (b) Fitted emission decay curves of **Ir_2Cl_2** in toluene at temperatures specified in the insets. (c) Emission decay times of **IrCl** as a function of temperature (black dots), and the best fit of Eq. 1.1 to the experimental values (red line). (d) Emission decay times of **Ir_2Cl_2** as a function of temperature (black dots), and the best fit of Eq. 1.1 to the experimental values (red line). SLR – Spin-Lattice Relaxation. (cf. ref.[19])

The best fit of Eq. 1.1 to the emission decay time values of complex **Ir_2Cl_2** in the temperature range 1.7 K ≤ T ≤ 120 K, with fixed τ(I) = τ(1.7 K) = 8.2 μs, revealed the individual decay times τ(II) = 7.0 μs and τ(III) = 0.05 μs, and energy gaps ΔE(II−I) = 8 cm^{-1} and ΔE(III−I) = 205 cm^{-1}. Extrapolating the T_1 state properties to temperature T = 300 K with Eq.1.1, these values give an average decay time of τ_{av} = 0.30 μs. This value is close to but notably shorter than the experimental value measured at T = 300 K, of τ(300K) = 0.44 μs. This deviation can be rationalized by the fact that τ_{av} is calculated from data measured in the frozen media, whereas τ(300K) is measured in a

liquid media condition. Better solvation and hence stabilization of the emitting state (T_1) in the liquid media may modify the $T_1 \rightarrow S_0$ transition rate. Stabilization of the T_1 state in liquid media is also seen in the red-shift of room temperature emission spectra relative to the spectra in frozen toluene matrix (compare emission spectra shown in Figure 1.2 and Figure 1.5).

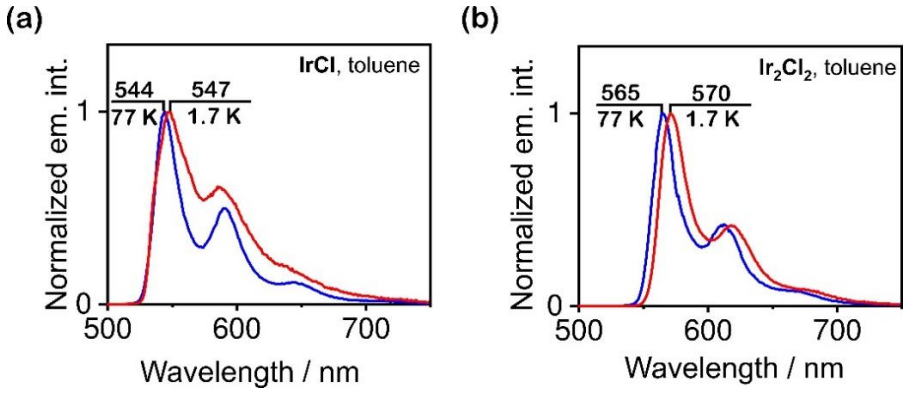

Figure 1.5. The emission spectra of complex **IrCl** (a) and complex **Ir_2Cl_2** (b) in toluene at T = 1.7 K (red trace) and T = 77 K (blue trace). (cf. ref.[19])

The T_1 state ZFS of 205 cm^{-1} obtained for **Ir_2Cl_2** is remarkable, compared to the 65 cm^{-1} obtained for the T_1 state of complex **IrCl**. This gives experimental evidence of a particularly strong SOC perturbation of the T_1 state. The observed increase in the ZFS value for the T_1 state of **Ir_2Cl_2** has to be strongly contributed to by SOC to singlet states, as the observed individual decay times of **Ir_2Cl_2** T_1 substates are much shorter compared to those of **IrCl**. For example, the decay time τ(I) = 8.2 µs of **Ir_2Cl_2** is an order of magnitude shorter (faster emission) than τ(I) = 97.6 µs of **IrCl**. Moreover, the individual III$\rightarrow S_0$ decay time of **Ir_2Cl_2** as short as τ(III) = 0.05 µs shows that in this respect substate III behaves almost like an excited singlet state. Indeed, the computational data discussed below show that the dinuclear structure of the complex **Ir_2Cl_2** can offer more singlet states available for direct SOC with the T_1 state, than the mononuclear structure of complex **IrCl**.

1.3 DFT and TD-DFT computations. To investigate the T_1 state SOC routes and to gain more insight into the electronic advantage of the dinuclear molecular design for enhancing the phosphorescence rate, density functional theory (DFT) calculations were carried out on both complexes, **IrCl** and **Ir_2Cl_2**. The details of all the computations presented in this work are given in the Experimental (Section 7.4). The molecular geometries of **IrCl** and **Ir_2Cl_2** were optimized for both ground state (S_0) and lowest triplet state (T_1) electronic configurations. The optimized ground state (S_0) geometries of both **IrCl** and **Ir_2Cl_2** agree well with the XRD determined geometries, with the coordination bond lengths differing by less than 0.05 Å and the coordination center angles deviating by less than 3° for three-point angles and 6° for torsion angles (Tables 8.1

and 8.2 in the Supplementary information). The optimized geometries of complex **Ir$_2$Cl$_2$** in S_0 and T_1 states possess a C_2 principal rotation axis, bisecting the pyrimidine ring through the C4 carbon (see Figure 1.1 for atom numbering) and the carbon in para-position to C4 and can be assigned to the C_2 point group symmetry. The time-dependent DFT calculations (TD-DFT) carried out for **IrCl** and **Ir$_2$Cl$_2$** predict the absorption spectra, reproducing the shape of the experimental spectra well. It is worth noting, however, that the lower energy bands of the theoretical spectra are slightly red-shifted, whereas the mid-range energy bands are blue-shifted relative to the experiment (See Figure 7.3 in the Experimental). Having a good agreement with the experimental data, it was assumed that the chosen theoretical method gives an acceptable accuracy in simulating the ground state electronic structures and excited states of both **IrCl** and **Ir$_2$Cl$_2$**.

The phenomenon of $T_1 \rightarrow S_0$ phosphorescence is best described from the perspective of the lowest triplet state as of the source state. Accordingly, computational results discussed in this work hereafter shall imply optimized T_1 state geometries, unless stated otherwise.

TD-DFT calculations show that the T_1 state of **IrCl** originates from a HOMO→LUMO electronic transition, where the HOMO is an Ir–Cl anti-bonding orbital with a major Ir d-orbital contribution of 45 %, and the LUMO is a π* orbital on the Phbib ligand (Figure 1.6 and Table 8.3).

The T_1 state of **Ir$_2$Cl$_2$** is also formed of a HOMO→LUMO transition but somewhat different from that in **IrCl.** The HOMO is an Ir1–Cl1 and Ir2–Cl2 anti-bonding orbital with total contribution from the two metals of 42 % (Figure 1.6, Table 8.4). The LUMO represents a π* orbital localized, in contrast to **IrCl**, on the dpp ligand. Thus, the T_1 state of **Ir$_2$Cl$_2$** is assigned as a dπ* charge transfer character, similarly to **IrCl**, but with the π* this time localized on dpp ligand. Such a difference between the complexes can be rationalized by the notably different extent of the π-backdonation from the metal centers to the dpp ligand. The effect can be traced by comparison of the bond lengths within the dpp ligands of the two complexes. As calculated, the lowest π* orbital on the dpp ligand is antibonding to the N1–C3 and N2–C5 bonds of the pyrimidine ring (Figures 7.4 and 7.5. For atom numbering see Figure 1.1). Indeed, according to the XRD analysis, the bond lengths 1.366(4) Å for N1–C3 and 1.356(4) Å for N2–C5 in complex **IrCl** (Molecule 1 in Table 8.1) increase to 1.375(4) Å for N1–C3 and to 1.374(4) Å for N2–C5 in complex **Ir$_2$Cl$_2$**, (Table 8.2 in Section 8.2) where two metals coordinated to the dpp ligand. Two metals in the case of complex **Ir$_2$Cl$_2$** have overall stronger π-backdonation to the dpp ligand, compared to one metal in **IrCl**. However, per metal center π-backdonation to dpp ligand in complex **Ir$_2$Cl$_2$** is probably lower than in **IrCl**. This increases the π-backdonation of the metal centers of **Ir$_2$Cl$_2$** to the π* orbitals of Phdib1 and Phbib2 ligands thus destabilizing those orbitals further to higher energies.

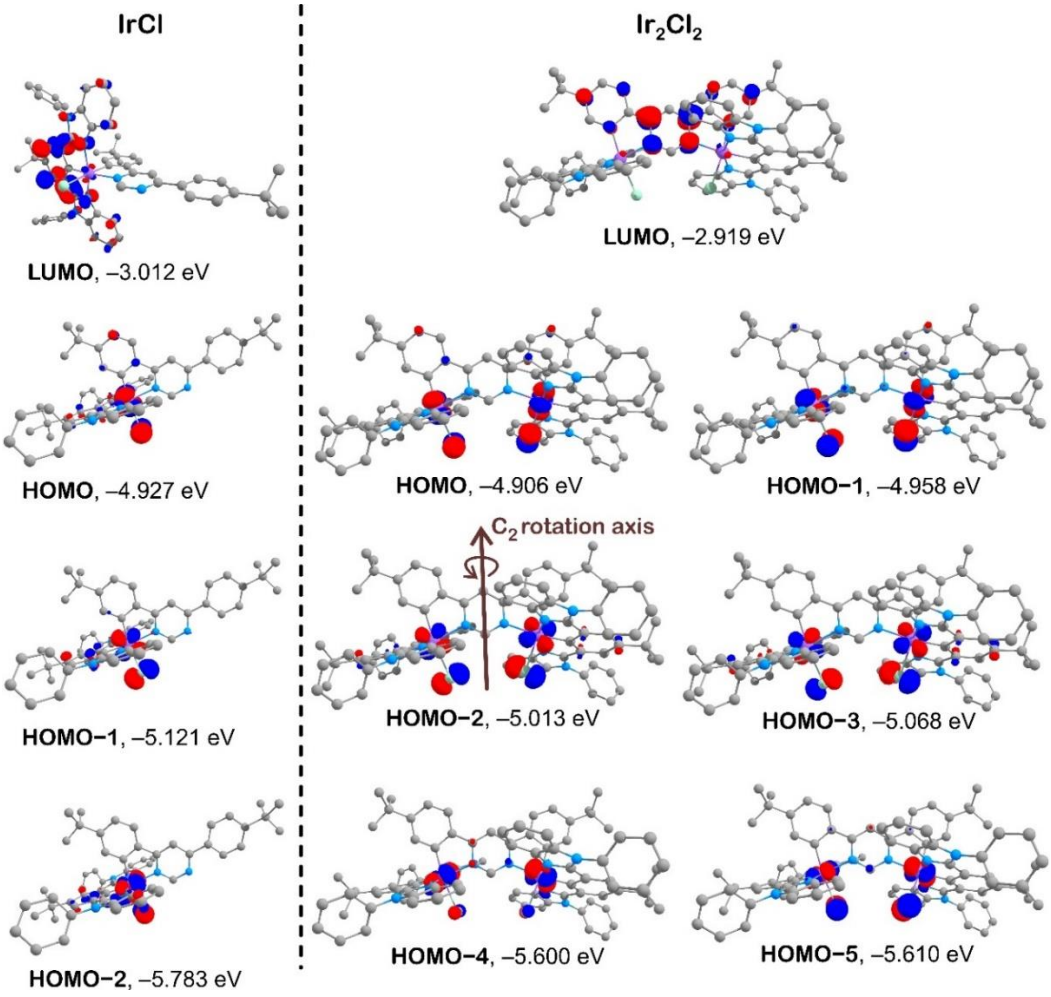

Figure 1.6. The iso-surface contour plots (iso-value = 0.05) of selected MOs of **IrCl** and **Ir_2Cl_2** at the T_1 state optimized geometry. (cf. ref.[19])

Indeed, as calculated at the ground state (S_0) geometry, the lowest π* orbital on each of the Phbib ligands of **Ir_2Cl_2**, representing LUMO+1 (–2.686 eV) and LUMO+2 (–2.684 eV), is destabilized compared to the lowest π* orbital on the Phbib ligand of complex **IrCl**, representing LUMO+1 (–2.739 eV).[19]

Interestingly, a careful inspection of the higher occupied molecular orbitals (MOs) brings attention to an important difference in the electronic composition of complexes **IrCl** and **Ir_2Cl_2**. In the mononuclear complex **IrCl**, the three t_{2g} symmetry 5d-orbitals of Ir ($5d_{xy}$, $5d_{xz}$ and $5d_{yz}$) and three 3p-orbitals of the coordinated chloride anion constitute three occupied Ir–Cl antibonding MOs representing HOMO, HOMO–1 and HOMO–2 (Figure 1.6). In the dinuclear complex **Ir_2Cl_2**, however, these Ir–Cl antibonding orbitals undergo pairwise electronic coupling between the two coordination sites which results in three pairs of MOs all involving both of the Ir ions about equally. A thus formed pair of MOs of **Ir_2Cl_2** represent two possible linear combinations of two analogous Ir–Cl antibonding orbitals at the two coordination sites. Therefore, two MOs

constituting such a pair involve the same Ir t_{2g} symmetry d-orbitals at the two metal centers and are different only in symmetry. This is easily followed in Figure 1.6 where a particular Ir 5d-orbital contributing to HOMO−1 of **IrCl**, in **Ir$_2$Cl$_2$**, contributes to HOMO−2 and HOMO−3. By the signs of orbital lobes, HOMO−2 is antisymmetric and HOMO−3 is symmetric to the C_2 rotation. The same type of symmetry is respectively valid for the pair HOMO and HOMO−1, and for the pair HOMO−4 and HOMO−5 of complex **Ir$_2$Cl$_2$** (Figure 1.6). It is noted that the net contribution of the Ir centers to each MO in the pairs described above for **Ir$_2$Cl$_2$**, is approximately equal to the contribution of Ir center to the corresponding MO of **IrCl** that involves the 5d-orbital of the same angular momentum orientation. For instance, the net Ir contribution to each HOMO−2 and HOMO−3 of **Ir$_2$Cl$_2$** is similar to the Ir contribution to HOMO−1 of **IrCl** (Tables 8.3 and 8.4 in Section 8.2). Thus, the dinuclear structure gives the doubled number of Ir contributed occupied MOs, compared to the mononuclear structure, with each MO having about the equal contribution of the two metal centers and the net metal contribution similar to that in the corresponding MO of the mononuclear structure.

According to the spin-selection rule, stating that the total spin of the state should not change upon an electronic transition ($\Delta S = 0$), the $T_1 \rightarrow S_0$ phosphorescence is a spin-forbidden process. This rule, however, can be relaxed by spin-orbit coupling (SOC) of the T_1 state with states of the singlet manifold.[31] The oscillator strength $f(T_1 \rightarrow S_0)$ resulting from the SOC of the T_1 state with singlet states is defined as:[31,32]

$$f(T_1 \rightarrow S_0) = \left[\sum_n \left|\frac{\langle T_1|\hat{H}_{SO}|S_n\rangle}{E(S_n)-E(T_1)}\right| \times \langle S_0|\mu|S_n\rangle\right]^2 \qquad (1.2)$$

Here T_1 and $E(T_1)$ are the lowest triplet state and its energy, respectively; S_n and $E(S_n)$ are an excited singlet state and its energy, respectively; S_0 is the ground state; $\hat{H}_{SO}$ is the spin-orbit coupling operator; μ is transition dipole moment ($\langle S_0|\mu|S_n\rangle^2 = f(S_n \rightarrow S_0)$). Considering complexes **IrCl** and **Ir$_2$Cl$_2$**, the excited singlet states in close energetic proximity to T_1 state are of mixed dπ* and ππ* character and have non-vanishing oscillator strength $f(S_n \rightarrow S_0)$. Then, the SOC matrix element $\langle T_1|\hat{H}_{SO}|S_n\rangle$ appears to be the main factor in Eq. 1.2 which largely defines the magnitude of the oscillator strength of $T_1 \rightarrow S_0$ transition. Since SOC is a short-range interaction, two states can effectively couple only if a particular heavy atom with a large SOC constant such as Ir (ζ=3909 cm^{-1})[33] contributes to the same natural transition orbital (NTO) of both states (either to the hole or to the electron). Then, for complexes **IrCl** and **Ir$_2$Cl$_2$**, both with a T_1 state largely of dπ* character, an effective SOC matrix element of Eq. 1.2 can be expressed as follows:

$$\langle T_1|H_{SO}|S_n\rangle = \sum_{i,j} a_{T_1} a_{S_n} c_i c_j \langle {}^3 d_i\pi^*|\hat{H}_{SO}|{}^1 d_j\pi^{*\prime}\rangle \qquad (1.3)$$

Here a_{T_1} and a_{S_n} are normalized configurational interaction coefficients of electronic transitions contributing to the state T_1 and an excited singlet state S_n, respectively; c_i and c_j are contributions of Ir d-orbitals d_i and d_j, respectively, to the molecular orbitals involved in the transitions; π^* and $\pi^{*\prime}$ are ligand localized π-orbitals. The matrix element $\langle {}^3 d_i \pi^* | \hat{\mathrm{H}}_{SO} | {}^1 d_j \pi^{*\prime} \rangle$ in Eq. 1.3 is significant only for the El-Sayed allowed cases[34] of direct SOC with $\pi^* = \pi^{*\prime}$ and $d_i \neq d_j$ e.g. different angular momentum of the d-orbitals as orbital rotation is required to conserve the total momentum of the electron (spin + orbital) when its spin flips (see Section 8.1 for more detail).[24] Thus, the T_1 state can have direct SOC with a singlet state that involves a transition from an Ir contributed molecular orbital different from HOMO (for $d_i \neq d_j$) to LUMO (for $\pi^* = \pi^{*\prime}$) in the case of complex **IrCl**, and from an Ir contributed molecular orbital different from HOMO and HOMO−1 to LUMO in the case of complex **Ir₂Cl₂**, as in the latter HOMO and HOMO−1 involve the same Ir d-orbitals at both metal centers. TD-DFT calculations for complex **IrCl** show one such singlet state available for direct SOC with the T_1 state: S_3 (HOMO−1→LUMO) which is within 0.5 eV energetic proximity to the T_1 state, whereas for complex **Ir₂Cl₂** there are two such singlet states: S_3 (HOMO−2→LUMO) and S_4 (HOMO−3→LUMO), which are within only 0.2 eV energetic proximity to the T_1 state (Tables 8.5 and 8.6). A notably smaller gap between state T_1 and spin-orbit coupled singlet states in the case of dinuclear **Ir₂Cl₂** is possibly due to the larger electronic conjugation within the molecule and consequently wider distribution of the involved orbitals. This may contribute to the higher density of the highest occupied MOs, suggested by calculations (Figure 1.6), and also reduce the exchange interaction decreasing the energy gap $\Delta(S_1{-}T_1)$. Both of these factors get the T_1 state closer to the excited singlet states electronically suited (El-Sayed allowed) for SOC with T_1.

The presence of two singlet states (S_3 and S_4) available for effective direct SOC with the T_1 state in complex **Ir₂Cl₂** is an advantage of the dinuclear molecular design. The HOMO−2 representing the hole NTO of the S_3 state and HOMO−3 representing the hole NTO of the S_4 state are a pair of orbitals formed by the electronic coupling of the two Ir−Cl sites and by the involved Ir t_{2g} orbitals, both are analogous to the HOMO−1 of complex **IrCl** (Figure 1.6). In complex **IrCl** the HOMO−1 represents the hole NTO of the S_3 state. Thus, the formation of pairs of orbitals involving the same Ir t_{2g} orbitals in the course of electronic coupling of two Ir−Cl sites in dinuclear complex **Ir₂Cl₂** also multiplies the number of singlet states (states S_3 and S_4 in **Ir₂Cl₂** instead of the only S_3 in **IrCl**) available for direct SOC with the emitting T_1 state. Importantly, HOMO, HOMO−2 and HOMO−3 of **Ir₂Cl₂** have similar contribution ratios between the two metal centers as the metals contribute about equally to each of the MOs. Therefore, the electronic suitability of each of states S_3 and S_4 for SOC with state T_1 in **Ir₂Cl₂** is not affected (not diminished) by splitting

the net metal contribution to HOMO, HOMO−2 and HOMO−3 between two centers. Hence, with the net metal contribution to each of HOMO−2 and HOMO−3 in **Ir_2Cl_2** being comparable to metal contribution to HOMO−1 in **IrCl**, the electronic suitability of each of states S_3 and S_4 for direct SOC with the T_1 state in **Ir_2Cl_2** is equal to that of state S_3 in **IrCl**.

With twice the number of singlet states electronically suited for SOC with state T_1 without a compromise in strength, compared to mononuclear **IrCl**, the phosphorescence rate of **Ir_2Cl_2** is predicted and experimentally found to be notably higher than that of **IrCl**. Moreover, the smaller energy separations between the state T_1 and states S_3 and S_4 in **Ir_2Cl_2**, compared to energy separation of states T_1 and S_3 in **IrCl**, through Eq. 1.2 should also contribute to the phosphorescence of **Ir_2Cl_2** being relatively fast.

Interestingly, in both **IrCl** and **Ir_2Cl_2** the higher occupied Ir–Cl antibonding orbitals with the different 5d-orbitals of iridium are also different by the contributing chlorine 6p-orbitals (Figure 1.6). Hence, the T_1 state with $p_i \rightarrow \pi^*$ contribution (partial $^3p_i\pi^*$ character within HOMO→LUMO transition) can also undergo direct SOC at the chlorine atom(s) with the singlet states bearing $^1p_j\pi'^*$ character where $p_i \neq p_j$ (different p-orbitals at the same chlorine atom) and $\pi^* = \pi'^*$. In other words, the singly occupied Ir–Cl antibonding orbitals can be involved in SOC of state T_1 with singlet states not only at the metal centers but almost entirely (at both Ir and Cl), thus increasing the probability of spin-flip. This may rationalize the relatively higher phosphorescence rate of the mononuclear **IrCl** compared to many other mononuclear Ir(III) complexes showing fast phosphorescence, for example, *fac*-Ir(ppy)$_3$ (ppyH – 2-phenylpyridine).[14] The diagrams in Figure 1.7 summarize the T_1 state properties of **IrCl** and **Ir_2Cl_2**.

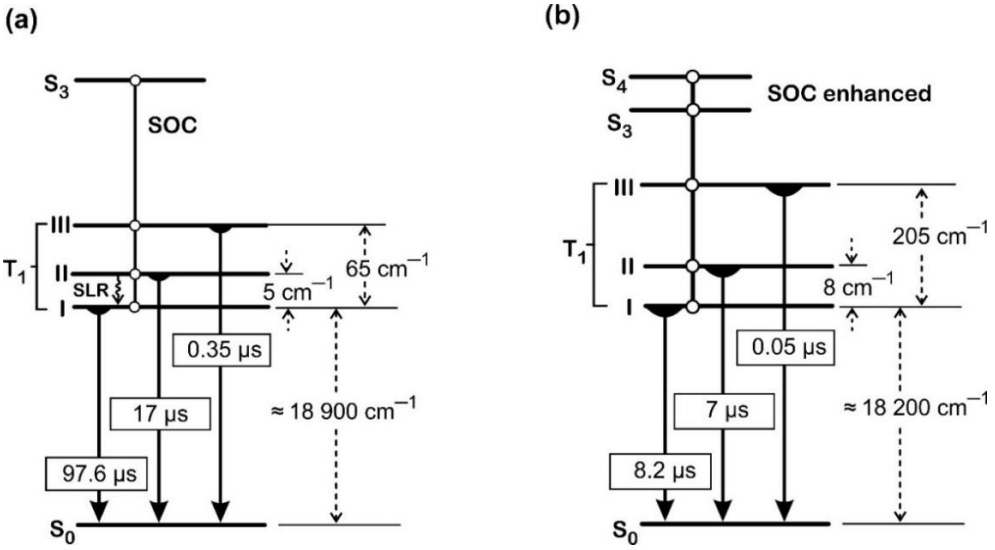

Figure 1.7. Simplified energy level diagrams summarizing the emissive properties of complexes **Ir_2Cl_2** (a) and **Ir_2Cl_2** (b) in the frozen toluene media. The diagrams are not to scale. (cf. ref.[19])

1.4 Concluding remarks. The Ir(III) based dinuclear molecular design can afford much faster phosphorescence, compared to the mononuclear analogue, because of the electronic level advantage enhancing the oscillator strength of $T_1 \rightarrow S_0$ transition. Under ambient conditions the phosphorescence of dinuclear complex **Ir_2Cl_2** is almost three times higher than that of the mononuclear analogue **IrCl**. As suggested for the first time in literature, the fundamental reason for such an enhancement of the phosphorescence rate in the (*quasi*)-symmetric dinuclear structure is the electronic coupling of Ir–Cl orbitals at the two coordination sites that results in three pairs of occupied MOs contributed by both metal centers with the same t_{2g} orbitals in a pair. This effect, consequently, also doubles the number of excited singlet states available for direct SOC with the emitting T_1 state thus more efficiently relaxing the $\Delta S = 0$ spin-selection rule for $T_1 \rightarrow S_0$ transition. These computational results are in line with the experimental findings that show remarkable shortening of the individual decay times of the T_1 substates accompanied by a T_1 state ZFS increase from mononuclear **IrCl** to dinuclear **Ir_2Cl_2**. As a result, complex **Ir_2Cl_2** is an emitter with an emission rate significantly higher compared to conventional monometallic Ir(III) phosphors.[14,35-47] Moreover, by the value of emission rate, **Ir_2Cl_2** also outcompetes the thermally activated delayed fluorescence (TADF)[48-54] materials which are often posed as OLED emitters alternative to phosphorescent materials.[48,55-58]

2. Spin-Orbit coupling on the metal coordinated halides and the phosphorescence rate of Ir(III) Complexes

As it was mentioned above in Chapter 1 (Section 1.3), conjugation of the chlorides' 3p-orbitals with the 5d-orbitals of Iridium center in **Ir_2Cl_2** and **IrCl** makes the chlorides SOC centers additional to the metals. This effect may enhance the SOC of the state T_1 with singlet states thus making the molecular design advantageous in terms of achieving a comparatively high phosphorescence rate. To investigate if the SOC of state T_1 with singlets could be maintained on the halide atom(s) as efficiently as on the Ir(III) center, it is interesting to consider complex **Ir_2I_2** structurally similar to **Ir_2Cl_2** but with iodides instead of chlorides (Scheme 2.1). The notably higher energy of 5p AOs of iodide, compared to 3p AOs of chloride, is expected to shift the localization of the higher occupied MOs from the metal centers more to the halides. This would increase the Halide to Ligand Charge Transfer (XLCT) character of the lower excited singlet and triplet states with a compromise in MLCT character, thus increasing the importance of the halides as SOC centers. It is noted that the SOC of the iodine atom calculated from the atomic spectra is $\zeta_\ell(\mathrm{I}) = 5069\ \mathrm{cm}^{-1}$, which is large and comparable to that of Iridium.[33]

Complex **Ir_2I_2** was synthesized from complex **Ir_2Cl_2** in a halide metathesis reaction with an excess of sodium iodide (NaI) in acetone (Scheme 2.1).

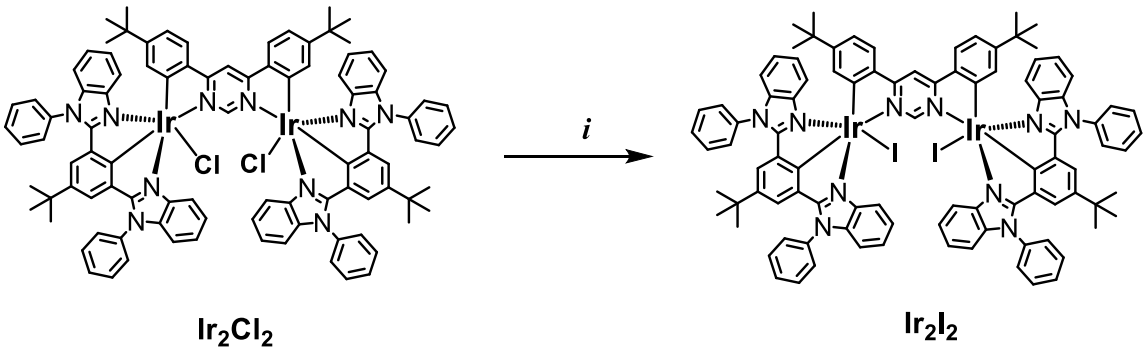

Scheme 2.1. Synthesis of complex **Ir_2I_2** from complex **Ir_2Cl_2**[19]. Reaction conditions: (*i*) NaI (20 molar equivalents), acetone, reflux, 2h. (cf. ref.[59])

For future reference in the text, it is noted that **Ir_2I_2** comprises the same organic ligands as **Ir_2Cl_2** does, C^N−N^C coordinating ditopic dpp ligand that bridges two metal centers and an N^C^N coordinating Phbib ligand at each metal center.

2.1 Optical spectroscopy. The optical spectroscopy measurements on **Ir_2I_2** were carried out in diluted toluene solution ($c \approx 10^{-5}$ M) and the key photophysical data are collected in Table 2.1. The UV/Vis absorption spectrum measured under ambient conditions features bands spanning an optical range of 280 nm ≤ λ ≤ 600 nm (Figure 2.1). The bands appearing in the lower energy

range, 500 nm ≤ λ_{abs} ≤ 600 nm, are of relatively low intensity (ε ≈ 1×10^4 M^{-1}cm^{-1}). These correspond to the electronic transitions with metal (d-orbital, M) and halide (p-orbital, X) to bridging ligand (π* - orbital, L) charge transfer character and are assigned to the lowest excited singlet states (^{1}dπ*+^{1}pπ* or ^{1}dpπ*; ^{1}MLCT+^{1}XLCT or ^{1}MXLCT). The relatively low intensity of these transitions is due to the poor spatial overlap of the orbitals localized on the metal and halide atoms with the π*-orbitals of the ditopic ligand. The bands of mid-range intensity (ε ≈ 3×10^4 M^{-1}cm^{-1}) in the optical range 350 nm ≤ λ_{abs} ≤ 500 nm are assigned to excited singlet states with mixed ^{1}MXLCT and Ligand Centered (^{1}LC, ^{1}ππ*) character involving either the bridging ligand (dpp) or the Phbib ligands. The set of intense bands (ε ≈ 7×10^4 M^{-1}cm^{-1}) centered at about 300 nm are assigned to excited singlet states of ^{1}LC (^{1}ππ*) character localized on the cyclometalating ligands dpp and Phbib. These assignments are supported by the TD-DFT calculations.

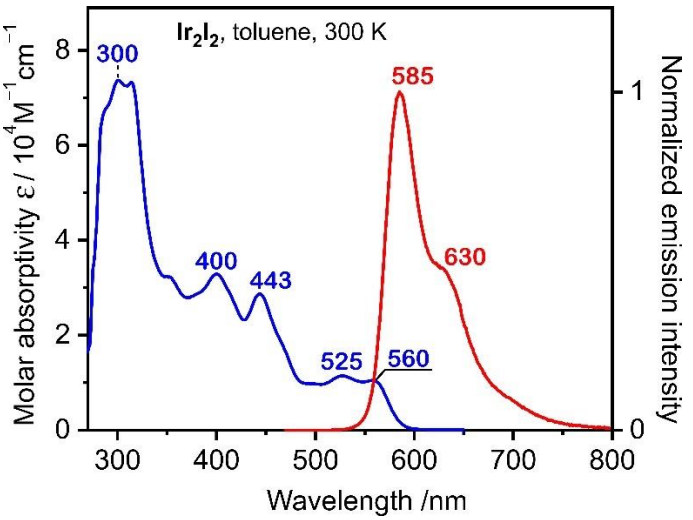

Figure 2.1. Absorption (blue) and emission (red) spectra of **Ir$_2$I$_2$** solution in toluene (c ≈ 10^{-5} M) measured at room temperature. (cf. ref.[59])

Although the absorption spectrum of **Ir$_2$I$_2$** is similar to that of **Ir$_2$Cl$_2$**, measured under the same conditions, it is noted that the lowest energy absorption bands of **Ir$_2$I$_2$**, assigned to ^{1}dπ*+^{1}pπ* transitions, are relatively red-shifted in comparison. For instance, the lowest energy absorption band maximum is at λ_{abs} = 550 nm in the spectrum of **Ir$_2$Cl$_2$** and at λ_{abs} = 560 nm in the spectrum of **Ir$_2$I$_2$**. This shift is associated with a stronger electron-donating character of iodide (5p-electrons), compared to chloride (3p-electrons), which destabilizes the higher occupied MOs and thus decreases the energy gap to the lowest orbitals unoccupied in the ground state.

Complex **Ir$_2$I$_2$** in toluene shows intense photoluminescence with the spectral maximum at λ_{max} = 585 nm and a shoulder at about λ = 630 nm (Figure 1). The emission is assigned to $T_1 \rightarrow S_0$ radiative transition (phosphorescence), which is typical for Ir(III) complexes. This assignment is also supported by the measurements conducted at cryogenic temperatures discussed further below.

Compared to that of **Ir_2Cl_2**, the emission spectrum of **Ir_2I_2** is similar in shape and slightly red-shifted, similar to the red shift of the lower energy absorption bands discussed above. Spectral overlap of absorption and emission of **Ir_2I_2** indicates a relatively small energy gap $\Delta E(S_1-T_1)$ and, similarly to the cases of **IrCl** and **Ir_2Cl_2**, can be rationalized by a strong charge transfer character of states S_1 and T_1. This shows that the state T_1 of **Ir_2I_2** is energetically close to the whole manifold of excited singlet states that should facilitate the efficient SOC of T_1 with singlets.

Table 2.1. A summary of key photophysical properties of **Ir_2I_2** and **Ir_2Cl_2** (for comparison) in a diluted toluene solution ($c \approx 10^{-5}$ M). The absorption spectrum was measured under ambient conditions. The ambient temperature (300 K) emission decay time and quantum yield values were measured for a degassed sample.

	Ir_2I_2	**Ir_2Cl_2**
Absorption λ_{max}/nm (ε /$M^{-1}cm^{-1}$)	560 (10500), 525 (11400), 443 (28700), 400 (32900), 315 (73250), 300 (73600).	550 (11300), 520 (12100), 443 (30300), 415 (23260), 380 (25640), 300 (82540).
Photoluminescence at T = 300 K		
λ_{max}/nm	585, 630	575, 618
Φ_{PL}/%	90	95
τ (τ_r)/μs*	0.34 (0.38)	0.44 (0.46)
$k_r/10^6$ s^{-1}	2.65	2.27
$k_{nr}/10^6$ s^{-1}	0.29	0.11
Photoluminescence at T = 77 K		
λ_{max}/nm	572, 620	565, 612
Φ_{PL}/%	100	100
τ (τ_r)/μs*	1.65 (1.65)	2.50 (2.50)
$k_r/10^6$ s^{-1}	0.60	0.40

*τ_r – radiative decay time calculated as $\tau_r = \tau/\Phi_{PL} = 1/k_r$

Measured for a degassed sample at room temperature, emission of **Ir_2I_2** has a very high quantum yield of Φ_{PL} = 0.9 (90 %) with a short decay time of only τ(300 K) = 0.34 μs (Figure 2.2). The corresponding radiative rate amounts to $k_r(300\ K) = \Phi_{PL}/\tau = 2.65\times10^6\ s^{-1}$. This rate is comparable to, and even slightly higher than, that of **Ir_2Cl_2 (**$k_r(300\ K) = 2.27\times10^6\ s^{-1}$**)** and represents one of the highest values reported for dinuclear Ir(III) complexes so far.[16,17,19,60]

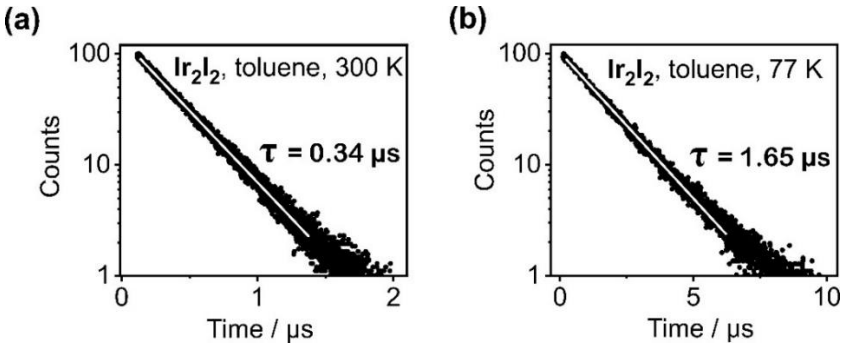

Figure 2.2. Emission decay curves of **Ir_2I_2** in toluene ($c \approx 10^{-5}$ M) measured at T = 300 K for a degassed sample (a) and at T = 77 K (b). The white lines on the black experimental data points represent the best fit of the mono-exponential decay function. (cf. ref.[59])

In frozen toluene at T = 77 K, the emission quantum yield of **Ir_2I_2** is $\Phi_{PL}(77\ K) = 1$ (100 %). The emission decay time under these conditions amounts to $\tau(77\ K) = 1.65$ μs, which corresponds to the radiative rate of $k_r(77\ K) = 0.6\times10^6\ s^{-1}$. The lower radiative rate at 77 K, compared to that at 300 K, is due to the lower population efficiency of the fastest emitting substate of T_1, which is investigated in detail below. It is noted that the rigid (frozen) medium at 77 K should strongly suppress the non-radiative $T_1 \rightarrow S_0$ relaxation processes in **Ir_2I_2** which is indicated by the increased emission quantum yield despite the decreased radiative rate as compared to room temperature (T = 300 K) conditions (Table 2.1).

Further details of the photoluminescent properties of **Ir_2I_2** can be gained by measuring its emission decay times at cryogenic temperatures as it was done for complexes **Ir_2Cl_2** and **IrCl** (Chapter 1). At T = 1.7 K, the emission decay time of **Ir_2I_2** amounts to $\tau(1.7\ K) = 6.4$ μs (Figure 2.3a). This value does not vary notably with temperature up to T = 3 K and is assigned to T_1 state's lowest energy substate I, $I \rightarrow S_0$. With the increase of temperature above T = 3 K, the emission decay time shows a slight increase and reaches a plateau in the range $15\ K \leq T \leq 25\ K$ (Figure 2.3b). This increase of emission decay time is due to the thermal population of the higher-lying substate II and hence the increasing contribution of the $II \rightarrow S_0$ transition. Evidently, the rate of $II \rightarrow S_0$ transition is slightly lower than that of transition $I \rightarrow S_0$, so the increasing thermal population of substate II slightly decreases the average emission rate. The average decay time of $I/II \rightarrow S_0$ transition reached at T = 20 K, a value corresponding to the plateau, is $\tau(20\ K) = 6.75$ μs (Figures 2.3a and 2.3b). With a further increase of temperature above T = 25 K, the emission decay time decreases steeply due to the thermal population of the highest lying substate III and the opening of the fast $III \rightarrow S_0$ transition path (Figure 2.3b). At T = 120 K, the measured emission decay time reaches a sub-microsecond value of $\tau(120\ K) = 0.66$ μs. The contribution of the energetically higher lying substates II and III of T_1 to the $T_1 \rightarrow S_0$ transition increasing with temperature is also

evidenced by the slight blue shift of emission spectrum from T = 1.7 K to T = 77 K shown in Figure 2.3c. It is noted that emission spectra measured at cryogenic temperatures are blue-shifted compared to the spectrum at T = 300 K, which might be due to better solvation (stabilization) of the emitting excited states in the liquid media.

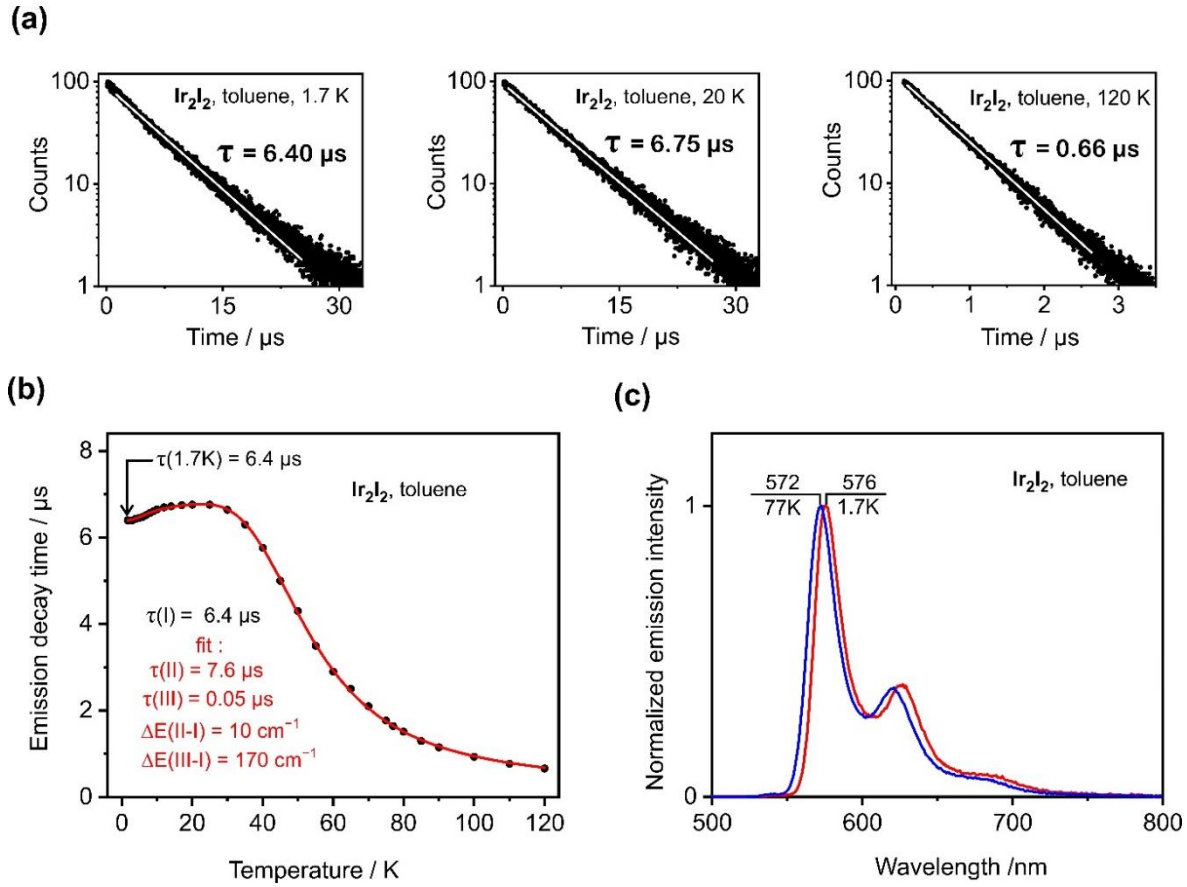

Figure 2.3. (a) Emission decay curves of **Ir2I2** in toluene ($c \approx 10^{-5}$ M) at temperatures specified in the insets. The white lines on the black experimental data points represent the best fit of the mono-exponential decay function. (b) Emission decay times of **Ir2I2** plotted as a function of temperature (black dots), and the best fit of Eq. 2.1 to the experimental values (red line). (c) The emission spectra of **Ir2I2** in toluene at T = 1.7 K (red trace) and T = 77 K (blue trace). (cf. ref.[59])

To obtain the individual time constants and relative energies of the substates I, II and III of state T_1 of **Ir2I2**, the decay time values measured in the temperature range $1.7 \leq T \leq 120$ K were analyzed with the three-level model described by Eq. 1.1. The best fit of Eq. 1.1 with the parameter τ(I) fixed to τ(I) = τ(1.7 K) = 6.40 μs, suggests the following values for the rest of the parameters in Eq. 1.1: τ(II) = 7.60 μs, τ(III) = 0.05 μs (50 ns), ΔE(II–I) = 10 cm^{-1} and ΔE(III–I) = 170 cm^{-1} (Figure 2.3b). The zero-field splitting (ZFS) of the T_1 substates with the value of ZFS = 170 cm^{-1} is among the largest reported for transition metal complexes (compare to refs.[14,19,23,24,61,62]). This indicates strong SOC mixing of T_1 substates with the higher-lying singlet and triplet states, which

affects their energies. According to the fit, the decay time value of T_1 substate III $\tau(III) \approx 50$ ns is similar to that of complex **Ir_2Cl_2** (Table 2.2).

Table 2.2. Emission decay times and the T_1 states Zero-Field Splitting (ZFS) determined for complexes **Ir_2I_2** and **Ir_2Cl_2** in toluene.

	Ir_2I_2	**Ir_2Cl_2**
τ(I)/μs	6.40	8.20
τ(II)/μs	7.60	7.00
τ(III)/μs	0.05	0.05
ΔE(II–I)/cm^{-1}	10	8
ΔE(III–I)/cm^{-1}	170	205

The lower-lying T_1 substates I and II of **Ir_2I_2**, in average are emitting even slightly faster (τ(I/II→S_0) = 6.75 μs at 20 K) than that in complex **Ir_2Cl_2** (τ(I/II→S_0) = 7.80 μs at 23 K). This may indicate that the T_1 substates I and II in **Ir_2I_2** are more perturbed by the SOC to the singlet states, which possibly is also associated with them being closer to the T_1 substate III, and hence with a smaller T_1 ZFS = 170 cm^{-1} of **Ir_2I_2** compared to **Ir_2Cl_2** with T_1 ZFS = 205 cm^{-1}.

The combined effect of the faster emitting T_1 substates I and II, and a smaller T_1 ZFS, favoring a more efficient population of the fastest T_1 substate III, results in a higher T_1→S_0 phosphorescence rate of complex **Ir_2I_2**, compared to **Ir_2Cl_2**, which is observed at both T = 300 K and T = 77 K (Table 2.1). Figure 2.4 summarizes the photophysical characteristics of the T_1 state of complex **Ir_2I_2**.

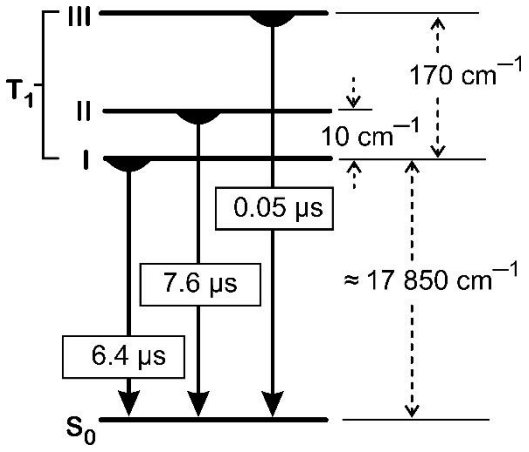

Figure 2.4. Simplified energy level diagram (not to scale) summarizing the emissive properties of **Ir_2I_2** in the medium of frozen toluene ($c \approx 10^{-5}$ M). (cf. ref.[59])

Considering the energetic proximity of the states T_1 and S_1, the emission decay times of **Ir_2I_2** were also analyzed with the four-level model described by Boltzmann type Eq. 2.1 which, in contrast to the three-level model of Eq. 1.1, in addition, considers the fourth state (IV) with the decay time parameter τ(IV) and energy gap parameter ΔE(IV−I). This allows assessing the possible thermal population of a state (state IV) laying above T_1 and its contribution to the emission of the analyzed complex.

$$\tau(T) = \frac{1+ \exp\frac{-\Delta E(II-I)}{k_B T}+\exp\frac{-\Delta E(III-I)}{k_B T}+\exp\frac{-\Delta E(IV-I)}{k_B T}}{\frac{1}{\tau(I)}+\frac{1}{\tau(II)}\exp\frac{-\Delta E(II-I)}{k_B T}+\frac{1}{\tau(III)}\exp\frac{-\Delta E(III-I)}{k_B T}+\frac{1}{\tau(IV)}\exp\frac{-\Delta E(IV-I)}{k_B T}} \qquad (2.1)$$

The fit with the fixed parameter τ(I) = τ(1.7 K) = 6.40 μs revealed the following values for other parameters: τ(II) = 7.70 μs, τ(III) = 0.067 μs (67 ns), τ(IV) = 0.063 μs (63 ns), ΔE(II–I) = 10 cm^{-1}, ΔE(III–I) = 160 cm^{-1}, ΔE(IV–I) = 260 cm^{-1}. The parameters for the T_1 substates I, II, and III are very close to those obtained above from the best fit of Eq. 1.1. Moreover, extrapolation of the three-level model of Eq. 1.1, consisting only of T_1 substates, to the room temperature conditions predicts a decay time of τ = 260 ns, which is closer to the experimental value τ(300 K) = 340 ns, compared to the value of τ = 230 ns predicted by the four-level model of Eq. 2.1 for the same conditions. This renders the three-level model more realistic thus allowing one to conclude that contribution of the fourth state (state IV) to the total emission intensity can't be significant at temperatures up to the ambient. Indeed, comparative analysis with the materials exhibiting efficient Thermally Activated Delayed Fluorescence (TADF) shows that to dominate the room temperature emission, the higher laying S_1 state should have at least three orders of magnitude higher radiative decay rate than the average rate of the lower laying triplet state (T_1).[48,58,63,64] This is not the case in either **Ir_2I_2** and **Ir_2Cl_2** where the T_1 substate III is characterized with a decay rate comparable to that of singlet states.

2.2 DFT and TD-DFT computations. To investigate the SOC paths of the emitting state T_1 with singlet states, the electronic structure of **Ir_2I_2** was analyzed using the DFT approach at the same theory level utilized for complexes **IrCl** and **Ir_2Cl_2**.

The calculations show that the LUMO is an π* orbital localized on the bridging (dpp) ligand, whereas the several higher occupied MOs including HOMO are mainly localized on the iodides, which contribute with the 5p AOs, and the metal centers, which contribute with the 5d AOs (Figure 2.5, Table 2.3 and Table 8.7).

Similarly to that in the case of complex **Ir_2Cl_2** (Section 1.2), electronic coupling of the two Metal – Halide sites in **Ir_2I_2** results in the formation of pairs of MOs contributed by the same d-orbitals of Ir centers and the same p-orbitals of iodides. One MO of the pair is symmetric, and the other MO is antisymmetric for the C_2 rotation of the molecule. For example, HOMO with

HOMO–3, and HOMO–1 with HOMO–2 constitute such pairs (Figure 2.5). As it was shown above comparing the mononuclear **IrCl** and dinuclear **Ir_2Cl_2**, the doubled number of MOs contributed by the same AOs in the dinuclear complex results in a larger number of singlet states electronically suited for efficient SOC with T_1 state, and thus facilitates the higher phosphorescence rate.

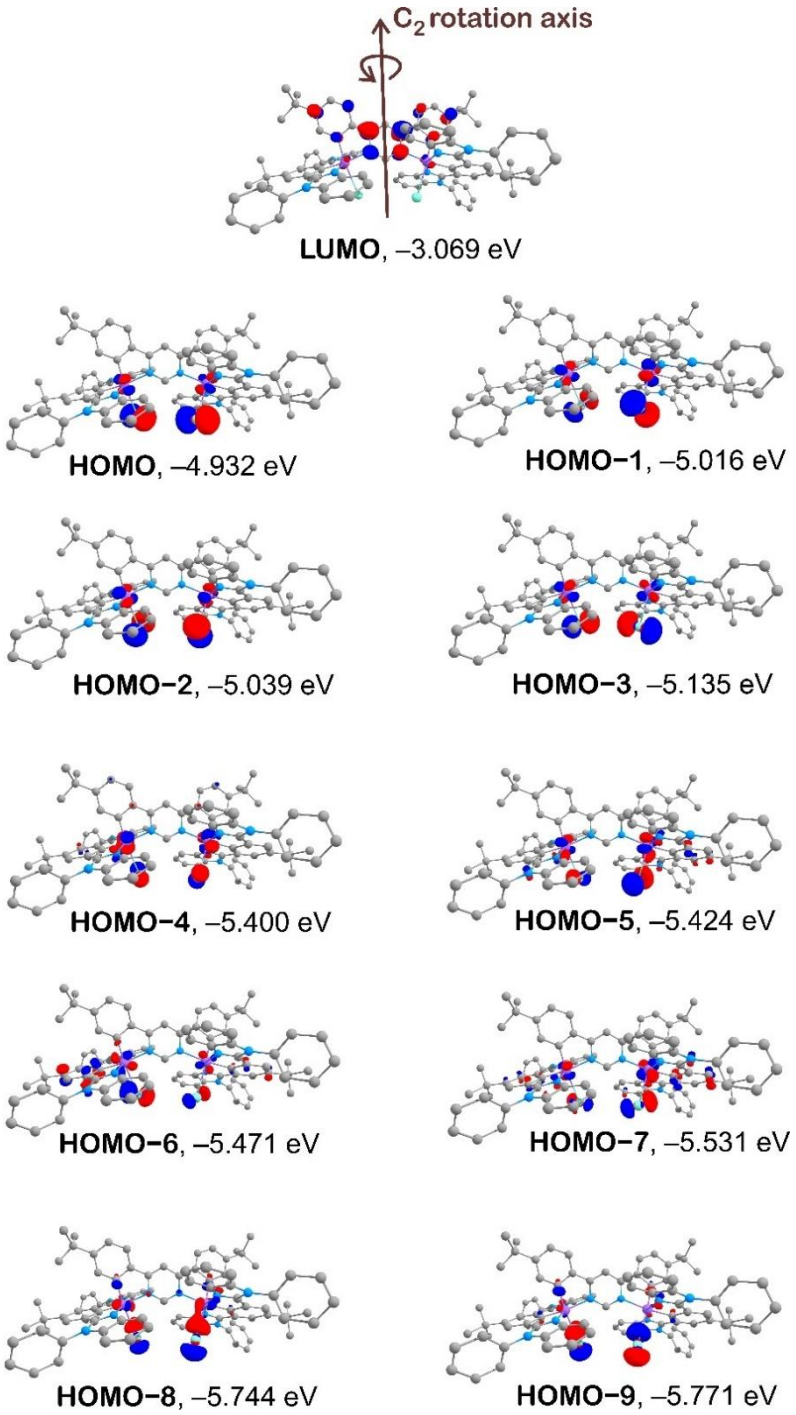

Figure 2.5. The iso-surface contour plots (iso-value = 0.05) of several selected MOs of **Ir_2I_2** at the T_1 state optimized geometry. (cf. ref.[59])

According to the TD-DFT calculations, state T_1 (1.851 eV) of **Ir_2I_2** originates from the HOMO→LUMO electronic transition (98 %). From localizations of HOMO and LUMO in the molecule, the state T_1 is of mixed Halide (X) to Ligand Charge transfer (XLCT, $^3p_i\pi^*$) and Metal to Ligand Charge Transfer (MLCT, $^3d_i\pi^*$) character. Analyzing the SOC pathways of state T_1 with singlet states, the states S_2 (1.964 eV, HOMO−1→LUMO) and S_3 (1.991 eV, HOMO−2→LUMO) come to attention. These singlets are in energetic proximity to state T_1, similarly to state T_1, have mixed character $^1p_j\pi^*$ (^{1}XLCT) and $^1d_j\pi^*$ (^{1}MLCT) and yet fulfill the requirement of total momentum conservation (El-Sayed's rule[34]) for effective SOC with state T_1 both at the metal centers ($d_i \neq d_j$) and at the iodides ($p_i \neq p_j$).

Interestingly, the net contribution of the iodides to the HOMO, HOMO−1 and HOMO−2 of **Ir_2I_2** is much larger than that of the Iridium centers (Figure 2.5, Table 2.3). For instance, the iodides' contribution to the HOMO amounts to 74 %, whereas the net contribution of the iridium centers is only 16%. Thus, in **Ir_2I_2** the pπ* (XLCT) character of states T_1, S_2 and S_3 strongly dominates over the dπ* (MLCT) character.

Table 2.3. Percentage contributions of the Ir centers, halides, dpp bridging ligand and Phbib ligands to the selected MOs of **Ir_2I_2** and **Ir_2Cl_2** according to Mulliken's population analysis. For the Ir atoms, halides and Phbib ligands, given are the net values. For individual contributions see Tables 8.4 and 8.7 in Section 8.2. The data for **Ir_2Cl_2** are adopted from ref.[19]

	Ir_2I_2				**Ir_2Cl_2**			
	Ir	**I**	**dpp**	**Phbib**	**Ir**	**Cl**	**dpp**	**Phbib**
LUMO	4	0	90	6	4	0	87	9
HOMO	16	74	6	4	44	25	19	15
HOMO–1	22	61	6	11	43	27	16	14
HOMO–2	21	66	6	7	39	33	4	24
HOMO–3	19	66	4	11	38	31	4	26

In contrast to **Ir_2I_2**, the higher occupied orbitals of **Ir_2Cl_2** have a predominant contribution from the Iridium centers (HOMO: Ir 44%, Cl 25%) (Table 2.3). Hence in **Ir_2Cl_2** the state T_1 (HOMO→LUMO) and excited singlets, S_3 (HOMO−2→LUMO) and S_4 (HOMO−2→LUMO), electronically suited for SOC with T_1, are predominantly of dπ* (MLCT) character.[19] Such a difference in the characters of the lowest excited states between **Ir_2I_2** and **Ir_2Cl_2** is due to the higher energy of the 5p AOs of iodides, compared to 3p AOs of chlorides, which result in a strong shift of localization of the halide contributed MOs from the bridging dpp ligand and the metals to the halides (Table 2.3). The stronger pπ* (XLCT) character of state T_1 and the lower excited singlet

states of complex **Ir₂I₂**, compared to those states of complex **Ir₂Cl₂**, also means the higher importance of the halides for the SOC efficiency of state T_1 with the singlet states and, consequently, for the phosphorescence rate.

2.3 Theoretical considerations. As expressed by Eq. 1.2 (Chapter 1, Section 1.3), the oscillator strength of radiative $T_1 \rightarrow S_0$ transition ($f(T_1 \leftrightarrow S_0)$) is defined by the efficiency of SOC of state T_1 with the excited singlet states (S_n) and by the transition oscillator strengths between those singlets and the ground state, $f(S_0 \leftrightarrow S_n)$. The relaxation of spin-forbiddenness of $T_1 \rightarrow S_0$ transition is proportional to the size of the SOC matrix elements of state T_1 with singlet states which reflect the perturbation degree of the T_1 state's wavefunction by the singlet states. It has been discussed in the literature that in transition metal complexes this perturbation increases with ^{3}MLCT character of the emitting state T_1 and is accompanied by an increase of phosphorescence rate (decrease of radiative decay time).[14] In this light, the composition of SOC matrix elements of Eq. 1.2 becomes the element of interest for a comparative discussion of the phosphorescence origins in **Ir₂I₂** and **Ir₂Cl₂**. It is noted that the absorption intensities, as well as the spectral overlap of absorption and emission of complexes **Ir₂I₂** and **Ir₂Cl₂**, are comparable, indicating that parameter $E(S_n) - E(T_1)$ of Eq. 1.2 for these materials is similar which also is in line with the TD-DFT calculations. The possible effect of the $\langle S_0|\mu|S_n\rangle$ parameter of Eq. 1.2 is addressed further below.

Since in **Ir₂I₂** and **Ir₂Cl₂** the metals and the halides are the only centers that fulfill the electronic requirements[34] for efficient SOC of state T_1 with singlet states based on El-Sayed's rule[34], the SOC matrix element in Eq. 1.2 is a sum of matrix elements brought by pπ* and dπ* characters of the involved states. Taking this into account and extending the spin-orbit coupling operator as $\hat{H}_{SO} = \zeta_\ell SL$ (ζ_ℓ is SOC constant, S is spin momentum operator, L is orbital momentum operator), the SOC matrix element of Eq. 1.2 can be expressed as follows:[65-67]

$$\langle T_1|\hat{H}_{SO}|S_n\rangle = \sum_{i,j} a_{T_1} a_{S_n} c_i c_j \langle {}^3 d_i \pi^* | \zeta_\ell(\mathrm{Ir}) SL | {}^1 d_j \pi^{*\prime}\rangle + \sum_{i,j} a_{T_1} a_{S_n} c_i' c_j' \langle {}^3 p_i \pi^* | \zeta_\ell(\mathrm{X}) SL | {}^1 p_j \pi^{*\prime}\rangle \quad (2.2)$$

Here a_{T_1} and a_{S_n} are normalized configuration interaction coefficients of state T_1 and state S_n, respectively; c_i and c_j are partial contribution coefficients of the AOs d_i and d_j, respectively, of the metal center to the MOs involved in transitions forming states T_1 and S_n; c_i' and c_j' are partial contribution coefficients of the AOs p_i and p_j, respectively, of the halide to the MOs involved in transitions forming states T_1 and S_n; X = I (**Ir₂I₂**), Cl (**Ir₂Cl₂**). The SOC matrix elements $\langle {}^3 d_i \pi^* | \zeta_\ell(\mathrm{X}) SL | {}^1 d_j \pi^{*\prime}\rangle$ and $\langle {}^3 p_i \pi^* | \zeta_\ell(\mathrm{X}) SL | {}^1 p_j \pi^{*\prime}\rangle$ in Eq. 2.2 are not vanishing only when $d_i \neq d_j$ *and* $p_i \neq p_j$, respectively, and $\pi^* = \pi^{*\prime}$. As mentioned above, in **Ir₂I₂** this condition is fulfilled for SOC matrix elements of state T_1 with states S_2 and S_3 at both the metal centers and the halides.

Similar derivations are valid also for SOC matrix elements of state T_1 with states S_3 and S_4 in complex **Ir₂Cl₂** (Section 1.3).[19]

According to Eq. 2.2, the partial contributions of the metal centers and the halides to the SOC of state T_1 with singlets are defined by coefficients c_i and c_j and SOC constant ζ_ℓ(Ir) = 3909 cm^{-1}, and by coefficients c_i' and c_j' and SOC constant of the halide ζ_ℓ(X), respectively. The states T_1 (HOMO→LUMO), S_2 (HOMO−1→LUMO) and S_3 (HOMO−2→LUMO) of complex **Ir₂I₂** are largely of pπ* character with a comparatively minor contribution of dπ* (Table 2.3). Thus, in Eq. 2.2 the coefficients c_i and c_j are much smaller than coefficients c_i' and c_j'. Consequently, with the SOC coefficient ζ_ℓ(Ir) = 3909 cm^{-1} being roughly comparable to ζ_ℓ(I) = 5069 cm^{-1}, the following relation is obtained for the SOC matrix elements at the metal centers and the halides:

$$\sum_{i,j} a_{T_1} a_{S_n} c_i c_j \langle {}^3 d_i \pi^* | \zeta_\ell(\mathrm{Ir}) SL | {}^1 d_j \pi^{*\prime} \rangle \ll \sum_{i,j} a_{T_1} a_{S_n} c_i' c_j' \langle {}^3 p_i \pi^* | \zeta_\ell(\mathrm{I}) SL | {}^1 p_j \pi^{*\prime} \rangle \qquad (2.3)$$

Relation 2.3 shows that in complex **Ir₂I₂** the iodides are of primary importance for SOC of state T_1 with singlets.

In complex **Ir₂Cl₂**, states T_1 (HOMO→LUMO), S_3 (HOMO−2→LUMO) and S_4 (HOMO−3→LUMO) are predominantly of dπ* character with a notably lower contribution of pπ* character (Table 2.3). Therefore, here the coefficients c_i and c_j are notably larger than c_i' and c_j'. Also, the SOC constant value ζ_ℓ(Ir) = 3909 cm^{-1} is almost an order of magnitude larger than ζ_ℓ(Cl) = 587 cm^{-1}. Hence, the SOC matrix elements of state T_1 with singlets at the metal centers are much larger than at the halides, and the following relation is valid:

$$\sum_{i,j} a_{T_1} a_{S_n} c_i c_j \langle {}^3 d_i \pi^* | \zeta_\ell(\mathrm{Ir}) SL | {}^1 d_j \pi^{*\prime} \rangle \gg \sum_{i,j} a_{T_1} a_{S_n} c_i' c_j' \langle {}^3 p_i \pi^* | \zeta_\ell(\mathrm{Cl}) SL | {}^1 p_j \pi^{*\prime} \rangle \qquad (2.4)$$

Relation 2.4 shows that the Iridium centers in complex **Ir₂Cl₂**, in contrast to **Ir₂I₂**, are of much higher importance for SOC of T_1 with singlets than the halides, although the contribution of the halides is also not vanishing.

2.4 Discussions. The above results show that in complexes **Ir₂Cl₂** and **Ir₂I₂** both the halides and the metals are contributing to the SOC of the emitting state T_1 with the singlets and, consequently, to the final rate of $T_1 \rightarrow S_0$ phosphorescence, as Eq. 1.2 and Eq. 2.2 describe. The contribution of the metals and the halides to this SOC is defined by the balance of dπ* and pπ* character of the state T_1 and of the singlet states spin-orbit coupled with T_1, which in turn is given by the partial contributions of the metals and the halides to a set of highest occupied MOs of the complex. These partial contributions depend on the halide; the stronger the electron-donating properties of the halides the more the shift of the orbital localization to halides. This increases the halides' role and decreases the metals' role in SOC of state T_1 with singlets and, consequently, in contribution to the phosphorescence rate. Importantly, the character of the halides also affects the contribution of the bridging ligand to the discussed higher occupied MOs, and hence the ππ*

character of the lowest singlet and triplet states. For instance, the strong shift of the electron density of several highest occupied MOs (HOMO, HOMO−1, HOMO−2, etc.) to the halides in **Ir₂I₂**, compared to **Ir₂Cl₂**, diminishes the ππ* character of the lowest excited states. This, from the viewpoints of Eq. 2.2, increases the sum of coefficients c_i and c_j with coefficients c_i' and c_j', that gives a larger net dπ*+ pπ* character of the states thus affecting the total value of the SOC matrix element in Eq. 1.2. Hence, it can be deduced that SOC of state T_1 with singlets in **Ir₂I₂** can be stronger than in **Ir₂Cl₂** as a combined effect of an overall increase of the net dπ*+ pπ* character of state T_1 and singlet states, electronically suited for SOC with T_1, and of a large SOC constant of iodine that allows it to maintain the high SOC efficiency of the discussed states despite the decreasing contribution of the metal centers (dπ* character) in favor of halides (pπ* character). Worth of noting effect, brought by the increased role of the halides as the T_1 state SOC centers, is the decreased value of ZFS of the T_1 state in complex **Ir₂I₂**, relative to **Ir₂Cl₂**. This is possibly a result of a lower field anisotropy at the mono-coordinated halides in comparison with metal ions that are hexa-coordinated by different ligands. Hence the SOC induced energy corrections to the T_1 substates in **Ir₂I₂** are closer in values that results in a smaller ZFS.[68] The smaller ZFS of T_1 state in complex **Ir₂I₂** works for a more efficient thermal population of the fastest emitting T_1 substate III, which increased the role of the latter in the emission process at room temperature and, consequently contributed to the enhancement of phosphorescence rate of the material.

It is noted that according to TD-DFT calculations, in **Ir₂I₂**, the singlet states suited for SOC with T_1, have oscillator strengths ($f(S_2 \rightarrow S_0) = 0.0374$ and $f(S_3 \rightarrow S_0) = 0.0099$) larger than such singlet states in complex **Ir₂Cl₂**[19] ($f(S_3 \rightarrow S_0) = 0.0063$ and $f(S_4 \rightarrow S_0) = 0.0010$). Through Eq. 1.2 ($\langle S_0|\mu|S_n\rangle^2 = f(S_n \rightarrow S_0)$) this factor might also contribute to the phosphorescence rate of **Ir₂I₂** being slightly higher than that of **Ir₂Cl₂**.

2.5 Concluding remarks. The molecular design of Ir(III) complexes with auxiliary halide ligands affords a unique electronic composition of the molecule that offers enhanced SOC of T_1 state with singlet states. The halide ligands turn out to be non-innocent and contribute significantly to photophysical processes in the complex. The doubly occupied p_x, p_y and p_z orbitals of halide, in conjunction with the d_{xy}, d_{xz} and d_{yz} orbitals of Ir(III) center and the π-system of the chromophoric ligand, constitute a set of highest occupied MOs to which both the metal centers and the halides contribute with AOs of different angular momentum orientations. With the bridging ligand utilized in **Ir₂I₂** and **Ir₂Cl₂** (dpp), contributions of the halides and metal centers to these MOs strongly prevail over the contribution of the bridging ligand and, consequently, a dense set of lowest excited states (triplet and singlet) have strong net dπ*+pπ* character, and only minor LC (ππ*) character. In such an electronic system, the total momentum conservation requirement for spin-orbit coupling of T_1 with singlet states (El-Sayed's rule) is fulfilled at both the Ir(III) and the halide centers (e.g.

the T_1 state is spin-orbit coupled with singlet states via both the dπ* and the pπ* characters). Depending on the halide, the predominant character of these excited states swings from dπ* in **Ir_2Cl_2** to pπ* in **Ir_2I_2** without the reduction of the SOC efficiency since Ir(III) centers and iodides have comparably large SOC constants. Our results suggest that the increasing role of the halides in SOC of T_1 state might decrease the ZFS and thus afford a more efficient thermal population of the highest lying and fastest emitting T_1 substate III, which further enhances the phosphorescence rate at ambient temperature.

In excited states of dπ*+pπ* character an unpaired electron is always at the metal center or at the halide, which represents a system of cooperatively working SOC centers effectively mixing the state T_1 with singlet states. Thus, compared to the homoleptic Ir(III) complexes such as *fac*-$Ir(ppy)_3$ **(**Hppy – 2-phenylpyrimidine) comprising only organic ligands, the pπ* character of several lowest excited singlet states and triplet state T_1, brought by the metal coordinated halide, results in a qualitative improvement in SOC efficiency of state T_1 with singlet states. This increases the $T_1 \rightarrow S_0$ phosphorescence rate (compare complexes **IrCl** and *fac*-$Ir(ppy)_3$; Hppy – 2-phenylpyrimidine)[59] and applied together with dinuclear design, as in **Ir_2I_2** and **Ir_2Cl_2**, affords materials with an unprecedentedly high rate of phosphorescence.

3. The bridging ligand as a tuning tool of photoluminescence of dinuclear Ir(III) complexes

As it was discussed in Chapters 1 and Chapter 2, the dinuclear design of Ir(III) complexes, where the chromophoric ligand bridges the metal centers, can strongly enhance the phosphorescence rate of the molecule, compared to the mononuclear design, due to a larger number of singlet states suited for SOC with the emitting T_1 states. In this light, it is also important to investigate the influence of the structure of the chromophoric bridging ligand on the photoluminescent properties of dinuclear complexes. For this purpose, a dinuclear Ir(III) complex **IrIr** (Chart 3.1) will be investigated. In contrast to the previously investigated complexes, **IrIr** comprises a bridging N^C−C^N ligand with a strongly π-excessive cyclometalating core of *thieno*[*3,2-b*]*thiophene* derivative functionalized with two terminal pyridine derivatives.

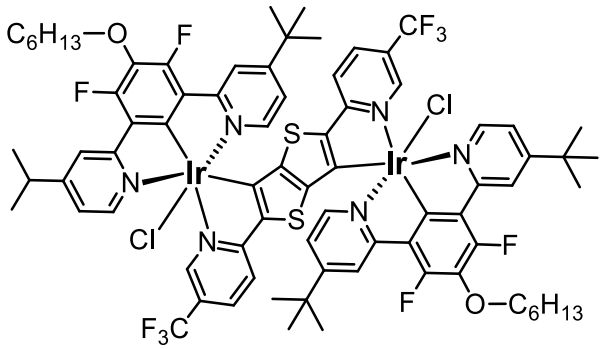

IrIr

Chart 3.1. Chemical structure of dinuclear Ir(III) complex **IrIr**. For synthetic details see ref.[69]

3.1 X-ray diffraction analysis. Crystals of **IrIr** suitable for x-ray diffraction (XRD) analysis were grown by a convectional diffusion of methanol into a dichloromethane solution of the complex. The obtained structure (Figure 3.1) displays the C_i point group symmetry with the inversion center in the middle of the bond annelating the thiophenes of the *thieno*[*3,2-b*]*thiophene* core of the ditopic N^C−C^N ligand. The Ir(III) coordination center features *quasi*-octahedral geometry where the coordinating carbon atoms of the N^C^N and N^C−C^N ligand are positioned *cis* to each other owing to the strong *trans* effect that they exert (compare ref.[17,19]). This configures the coordination center so that the chloride ligands are positioned *trans* to the coordinating carbon atom of the N^C−C^N bridging ligand. The coordination bond lengths and angles (Table 8.9) are unremarkable from those of similar complexes.[17,19]

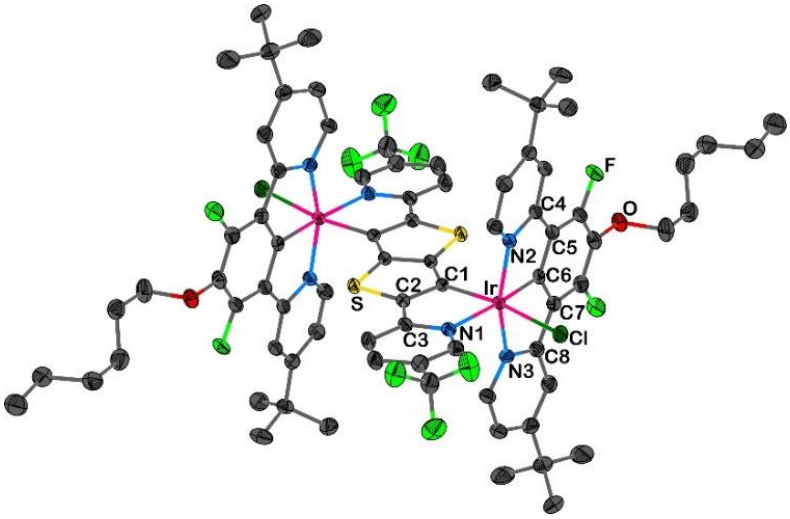

Figure 3.1. The XRD determined molecular structure of complex **IrIr** in the crystal. Thermal ellipsoids are shown at the 50% probability level, and hydrogen atoms are omitted for clarity. (cf. ref.[69])

3.2 Steady-state optical spectroscopy. The ambient temperature UV-vis absorption spectrum of **IrIr** in dichloromethane (DCM) reveals a structured band in the long-wavelength end with two resolved maxima at 518 nm and 485 nm that is followed by another intense band peaking at 400 nm (Figure 3.2a, Table 3.1). The structured longer-wavelength band is assigned to the lowest-energy electronic transition within the singlet manifold, $S_0 \rightarrow S_1$. The partially resolved vibronic structure and high molar absorption coefficients, $\varepsilon(518\ nm) = 2.8\times10^4\ M^{-1}cm^{-1}$ and $\varepsilon(485\ nm) = 1.95\times10^4\ M^{-1}cm^{-1}$, indicate the dominating $\pi\rightarrow\pi^*$ character of the electronic transition. This allows assigning the lowest singlet excited state (S_1) as a ligand centered $^1\pi\pi^*$ (^{1}LC) state localized on the ditopic N^C-C^N ligand representing the largest conjugated system in complex **IrIr**. This assignment contrasts dinuclear complexes described in preceding chapters that show significantly less intense $S_0 \rightarrow S_1$ absorption bands due to Metal to Ligand Charge Transfer (MLCT) transitions,[17,19,70] and is further corroborated by TD-DFT calculations presented below.

Measured in dichloromethane ($c \approx 10^{-5}$ M) at ambient temperature, complex **IrIr** shows photoluminescence spectrum comprising two emission bands which appear in green to yellow and in far-red to near infra-red (NIR) optical ranges, respectively (Figure 3.2). The longer wavelength band is about two orders of magnitude more intense in comparison and features a vibrationally structured shape with the maxima at $\lambda_{max} = 714$ nm and resolved shoulder at $\lambda = 790$ nm.

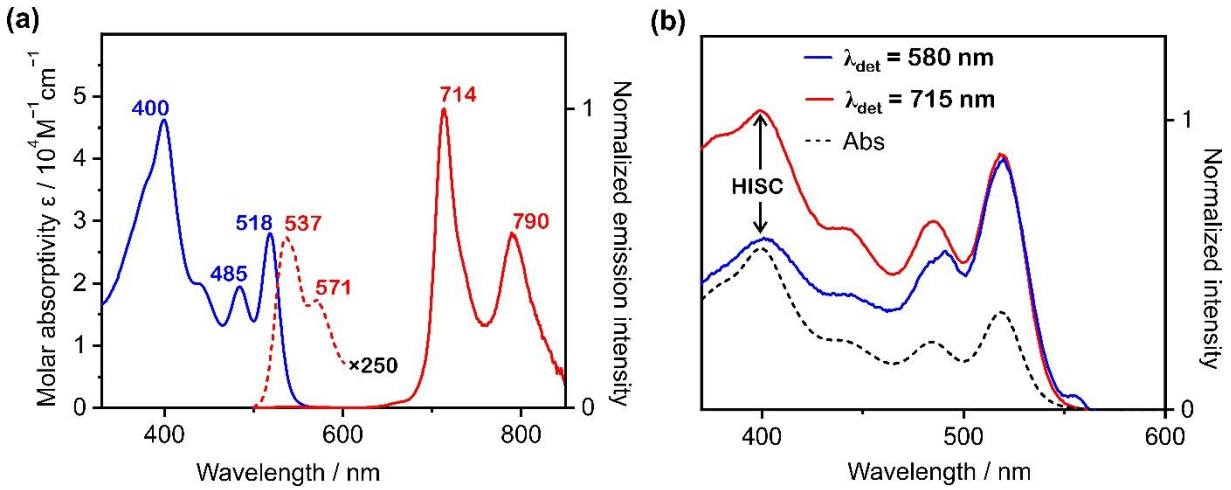

Figure 3.2. (a) Ambient temperature absorption (blue) and luminescence (red) spectra of **IrIr** in dichloromethane (c ≈ 10^{-5} M). The emission was measured for a degassed sample. (b) Excitation spectra of **IrIr** measured in degassed dichloromethane (c ≈ 10^{-5} M) at ambient temperature with detection wavelengths λ_{det} = 580 nm (blue trace) and λ_{det} = 710 nm (red trace), respectively, and normalized absorption spectrum of **IrIr** (dashed black trace). HISC stands for the Hyper Intersystem Crossing, i.e., ultrafast ISC between higher excited singlet states (S_n; n > 1) and triplet states (T_m), $S_n \rightarrow T_m$. (cf. ref.[69])

In the degassed sample this emission shows a decay time of τ(300K) =2.9 μs (Figure 3.3) and quantum yield of Φ_{PL} = 3.5%. The corresponding radiative rate amounts to $k_r = \Phi_{PL}/\tau = 1.2\times10^4$ s^{-1} with the radiative decay time $\tau_r = 1/k_r$ = 82 μs. Thus, owing to the radiative decay time in the microsecond time range, this emission is assigned as $T_1 \rightarrow S_0$ phosphorescence. The notably lower rate of phosphorescence, along with structured band shape of the triplet state emission, contrasting the **Ir_2Cl_2** and **Ir_2I_2** discussed above and some other reported dinuclear Ir(III) complexes[17,60,70], indicates the dominating ligand centered character (^{3}LC) of the T_1 state which in more detail will be discussed further below.

Thus, the use of π-excessive N^C−C^N ligand in **IrIr** results affords phosphorescence appearing NIR optical range. The quantum yield (Φ_{PL} = 3.5%), although moderate, accounts to the highest values found for NIR emitting Ir(III) complexes so far.[70-76] In air-saturated dichloromethane, the phosphorescence of **IrIr** has the decay time of τ = 0.85 μs, by a factor of about three shorter than in oxygen-free solvent (Figure 3.3), but is still detectable and not quenched[77,78] completely. This is important when application at aerobic conditions, for instance in biologic environments, is considered

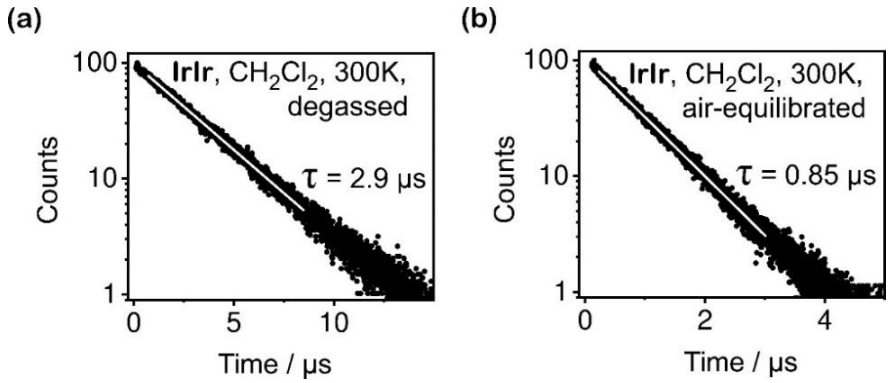

Figure 3.3. Emission decay profiles measured for a diluted solution of complex **IrIr** in dichloromethane ($c \approx 10^{-5}$ M), degassed (a) and air-equilibrated (b), at room temperature with signal detection at λ_{det} = 715 nm. (cf. ref.[69])

Table 3.1. Summary of key photophysical properties of **IrIr** in a diluted dichloromethane solution ($c \approx 10^{-5}$ M) under ambient temperature. The photoluminescence decay time (λ_{det} = 715 nm) and quantum yield were measured for a degassed sample. The decay time value in brackets is measured for an air-equilibrated sample. (cf. ref.[69])

Absorption	λ_{max}/nm (ε/$M^{-1}cm^{-1}$)	518 (28000), 484 (19500), 400 (46200).
Photoluminescence	λ_{max}/nm	537, 571 (Fl); 714, 790 (Ph)
	Φ_{PL} /%	3.5
	τ /μs	2.9 [0.85] (Ph.)
	$k_r/10^4$ s^{-1}	1.2
	$\tau_r = (1/k_r)$/μs	82
	$k_{nr}/10^4$ s^{-1}	33.3

The shorter wavelength emission band of **IrIr** appears with the maximum at λ_{max} = 537 nm and resolved vibrational shoulder at λ = 571 nm (Figure 3.2a). A mirror-symmetry band shape relationship with the $S_1 \leftarrow S_0$ absorption band allows assigning this emission as $S_1 \rightarrow S_0$ fluorescence of **IrIr**. This assignment is further substantiated by the excitation spectra (Figure 3.2b). Both of

the excitation spectra of **IrIr**, recorded at detection wavelengths λ_{det} = 580 nm (fluorescence) and λ_{det} = 715 nm (phosphorescence), resemble the UV-vis absorption spectrum of **IrIr** indicating that both emissions indeed belong to the same absorbing species, i.e. the **IrIr** complex. At shorter excitation wavelengths, the spectrum recorded at λ_{det} = 715 nm (red line) is more intense than the spectrum recorded with λ_{det} = 580 nm (blue line). This spectral difference indicates that the emitting states T_1 and S_1 are populated with different relative efficiencies depending on the exciting photon energy. This finding conforms with the hyper intersystem crossing (HISC) effect between higher excited singlet and triplet states (Figure 3.2b).[79,80]

The fluorescence of **IrIr** is short-lived. Transient absorption experiments (see below) reveal a decay time of only τ_{S1} = 2.3 ps. The ultrafast decay of the fluorescent state S_1 results from ISC to the triplet manifold, competing with direct relaxation to the ground state.

Measured emission quantum yield is invariant with excitation wavelength, despite the occurrence of HISC. This invariance results from a very small contribution of the S_1 fluorescence to the total emission intensity and high efficiency of ISC (from S_1) populating the T_1 state with a quantum yield close to unity which is also confirmed by transient absorption experiments. Thus, almost all non-radiative relaxations to the ground state decreasing the Φ_{PL} are assigned to the non-radiative transitions from the triplet state, $T_1 \rightarrow S_0$.

The occurrence of $S_1 \rightarrow S_0$ fluorescence of **IrIr** detectable by steady state experiments corresponds to the strong ^{1}LC character of state S_1 and hence to a high oscillator strength $f(S_1 \rightarrow S_0)$. This can be concluded from the large value ε(518 nm) = 2.8×10^4 $M^{-1}cm^{-1}$ assigned to the $S_1 \leftarrow S_0$ absorption, and from TD-DFT calculations predicting the value of f ($S_1 \rightarrow S_0$) = 0.29 (Table 8.11). On the other hand, the observable $S_1 \rightarrow S_0$ fluorescence of **IrIr**, may also indicate slow ISC from state S_1 to triplet manifold, compared to purely phosphorescent Ir(III) complexes. The low rate of ISC may result from LC character ($\pi\pi^*$) of the S_1 and T_1, as was indicated by the spectroscopic data above, and their significant energy separation.[71] Indeed, the energy gap $\Delta E(S_1 - T_1)$ estimated from spectral separation of fluorescence (λ = 537 nm) and phosphorescence maxima (λ = 714 nm) amounts to $\Delta E(S_1 - T_1)$ = 4600 cm^{-1} (0.57 eV) and is considered as unusually large (compare to computed values in refs.[17,19]).

3.3 Time-resolved absorption spectroscopy. The excited state dynamics of **IrIr** were studied by femtosecond transient absorption spectroscopy. The apparatus setup, experimental procedure and data analysis are described in the experimental part (Section 7.3). A dichloromethane solution of **IrIr** ($c \approx 10^{-5}$ M) was excited with a pumping laser pulse at λ_{exc} = 520 nm corresponding to the $S_0 \rightarrow S_1$ transition of **IrIr**. Within the time of the excitation pulse, the S_1 state is populated with the characteristic positive absorption features intersected by their

negative ground state bleach and stimulated emission features (see Figure 3.3a). The initial spectrum changes into a new spectrum accompanied by a complete loss of the stimulated emission signal and partial loss of the ground state signal. The newly formed absorption features of **IrIr** shows broad positive absorption bands starting from $\lambda \geq 530$ nm. The dynamics of this change is completed within 10 ps and this new spectrum does not change within the observed time window of 2 ns any further and can, thus, be assigned to the corresponding triplet spectrum. A global fit quantifies the S_1 decay with the lifetimes of $\tau_{S1} = 2.3$ ps and the decay associated difference spectra (see inset in Figure 3.4a) show the corresponding spectral changes that occur with this lifetime[81,82]

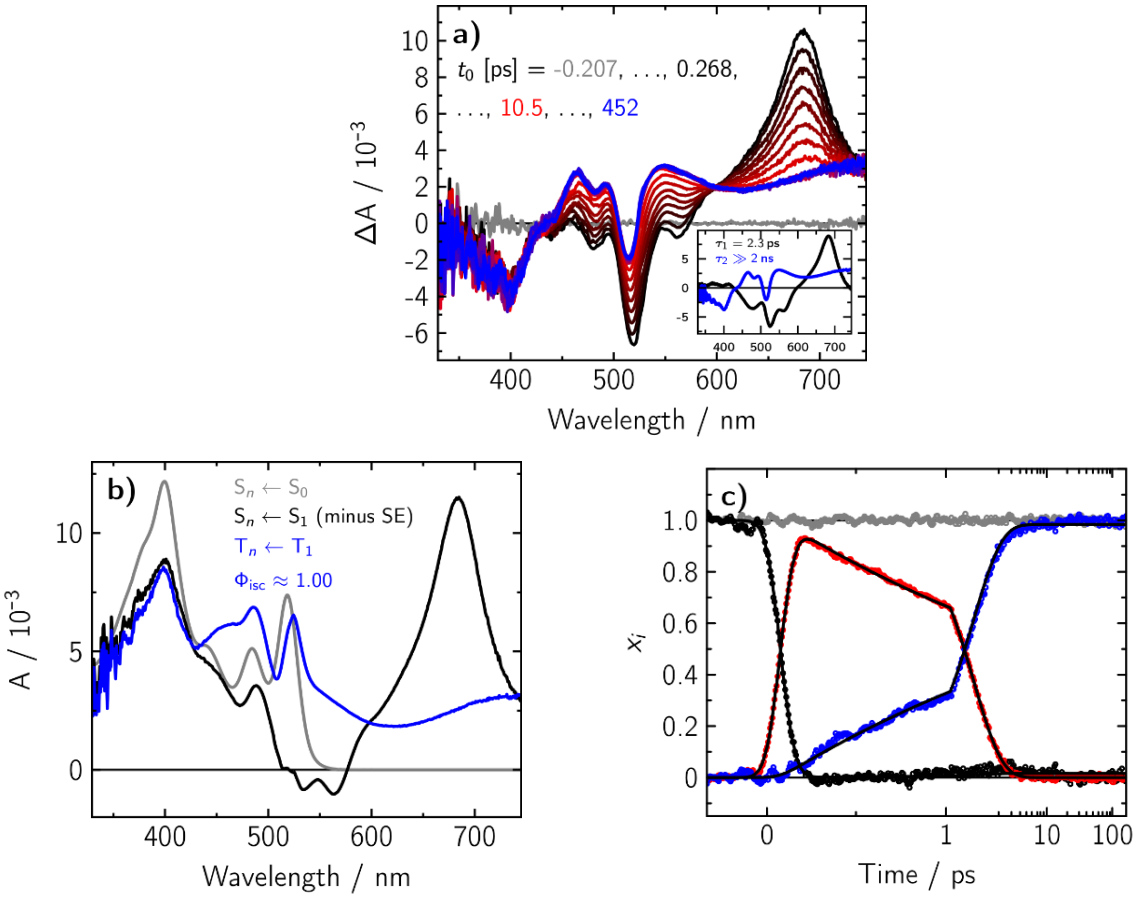

Figure 3.4. Transient absorption spectra of **IrIr** in dichloromethane after excitation into the corresponding $S_1 \rightarrow S_0$ absorption band at $\lambda = 520$ nm. (a) Raw data at selected delay times as indicated. The inset shows the decay associated difference spectra (DADS) from a global biexponential fit on the data. (b) Species associated spectra (SAS) of all contributing electronic species as indicated where SE stands for Stimulated Emission (for further details see Section 7.3). (c) Corresponding mole fraction (x_i) vs. time profiles resulting from the decomposition of the raw data with the SAS. The black lines show the global fit.

Applying a standard photophysical model consisting of the S_0, S_1, and T_1 states the transient absorption data can be decomposed into the species associated spectra (SAS, see Figure 3.4b) and their corresponding concentration-time profiles (see Figure 3.4c). This decomposition allows

consequently to determine the corresponding intersystem crossing yield to be of almost unity ($\Phi_{ISC} \approx 1$), yielding ISC rate constant of $k_{ISC} = \Phi_{ISC}/\tau_{S1} = 4.3\times10^{11}\ s^{-1}$. Typically, for the purely phosphorescent iridium complexes, such as $Ir(ppy)_3$ (Hppy – 2-phenylpyridine), intersystem crossing times of the order of 0.1 ps are found.[83-87] Therefore, the ISC time of τ(ISC) = 2.3 ps is regarded as long.

3.4 DFT and TD-DFT computations. To view the photophysical properties of **IrIr** from electronic structure perspectives, DFT and TD-DFT calculations were carried out with a model complex **IrIr'** where alkoxy and tret-butyl groups on the N^C^N ligands of **IrIr** are truncated to methoxy and methyl groups, respectively.

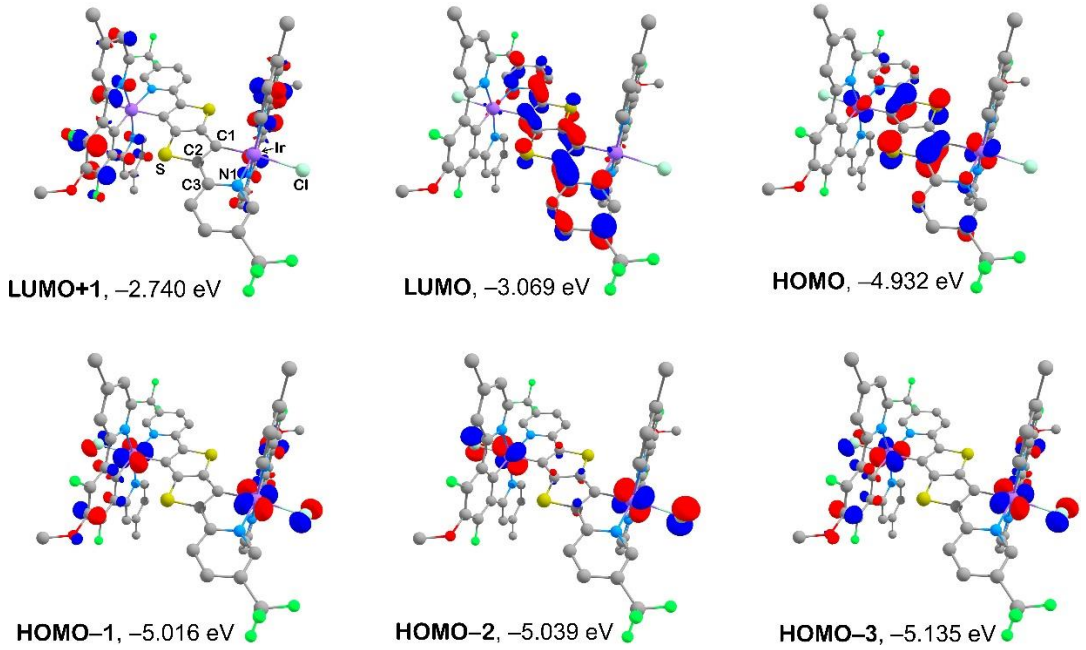

Figure 3.5. The iso-surface contour plots (iso-value = 0.05) of several selected MOs of the model complex **IrIr'** at the T_1 state optimized geometry. (cf. ref.[69])

The results of TD-DFT calculations further substantiate the assignments of spectroscopic data presented above. The energy separation between the lowest excited triplet and singlet states, calculated as a difference of vertical excitation energies $E(S_0\rightarrow S_1)$ and $E(S_0\rightarrow T_1)$ (Table 8.11), amounts to $\Delta E(S_1–T_1) \approx 0.54$ eV (4300 cm^{-1}). This is very close to the value 0.57 eV (4600 cm^{-1}) estimated from the spectral positions of the fluorescence and phosphorescence maxima (Figure 3.2a). Such a large gap $\Delta E(S_1–T_1)$ is a consequence of the LC character and identical orbital origin (HOMO $\rightarrow$ LUMO) of the two states. With both HOMO and LUMO confined within the bridging ligand (Figure 3.5), the exchange interaction of the unpaired electrons is strong and, consequently, the $\Delta E(S_1–T_1)$ value is large.[88] Importantly, the TD-DFT results show that all triplet states higher

than T_1 are also above the S_1 state [$\Delta E(T_2–S_1) = 0.08$ eV]. Thus, to conform with the law of energy conservation, intersystem crossing from S_1 can involve only higher vibrational levels of the T_1 state (direct ISC $S_1 \rightarrow T_1$) which agrees with the results of transient absorption data discussed above.

The ISC rate $k_{ISC}(S_1 \rightarrow T_1)$ is expressed in terms of the Fermi golden rule as a combination of electronic and nuclear factors as:[89]

$$k_{ISC}(S_1 \rightarrow T_1) = \frac{2\pi}{\hbar} \left|\langle S_1|\hat{H}_{SO}|T_1\rangle\right|^2 \times \text{FCWD} \qquad (3.1)$$

Where $\hbar$ is reduced Planck's constant, $\Delta E(S_1–T_1)$ is the energy gap between states S_1 and T_1, H_{SO} is the spin-orbit coupling operator and FCWD is the Frank-Condon weighted density of states, representing the vibrational overlap of states T_1 and S_1 (nuclear factor).

The spin-orbit coupling operator is extended as $H_{SO} = \zeta_\ell(X)SL$ where ζ_ℓ is SOC constant of atom X, S is spin momentum operator and L is orbital (angular) momentum operator. The SOC constant of Iridium (ζ_ℓ = 3909 cm^{-1}) is about three orders of magnitude larger than the SOC constant of the lighter main group elements (C, H, N, O).[33] Hence, the contributions of light atoms to SOC can be neglected. The minor involvement of the Iridium centers to the states S_1 and T_1, non-conformity with the El-Sayed's rule[34] for efficient SOC, due to the same orbital origin of states S_1 and T_1, both lead to a relatively small SOC matrix element of states S_1 and T_1 . The small SOC matrix element renders the electronic factor of Eq 3.1 small. The nuclear factor in Eq.3.1, represented by FCWD, depends on the energy gap $\Delta E(S_1–T_1)$ as:[89,90]

$$\text{FCWD} \propto \exp[-(\Delta E(S_1–T_1))^2] \qquad (3.2)$$

which is also known as the energy gap law.[15] Therefore, a relatively large $\Delta E(S_1–T_1)$ plays for a relatively small nuclear factor (FCWD) in Eq 3.1. Thus, with both electronic and nuclear factors in Eq. 3.1 being relatively small, a relatively low $k_{ISC}(S_1 \rightarrow T_1)$ can be expected.[79] This rationalizes the unusually low rate of $S_1 \rightarrow T_1$ ISC and the dual emissive behavior of **IrIr**.

The LC character of the T_1 and a large energy gaps $\Delta E(S_n–T_1)$ to the higher laying singlet states suited for SOC with T_1 through Eq.1.2 and Eq. 1.3 (Chapter 1, Section 1.3) also predict a relatively small oscillator strength $f(T_1 \rightarrow S_0)$.[24,31] This, along with a relatively small Einstein's coefficient of spontaneous emission due to the low energy of state T_1, might rationalize the rate of $T_1 \rightarrow S_0$ phosphorescence of **IrIr** being about two orders of magnitude lower than that of dinuclear **Ir_2Cl_2** and **Ir_2I_2** and even that of mononuclear **IrCl**. The state diagram shown in Figure 3.6 summarizes the photophysical and computational data for complex **IrIr** and model structure **IrIr'**.

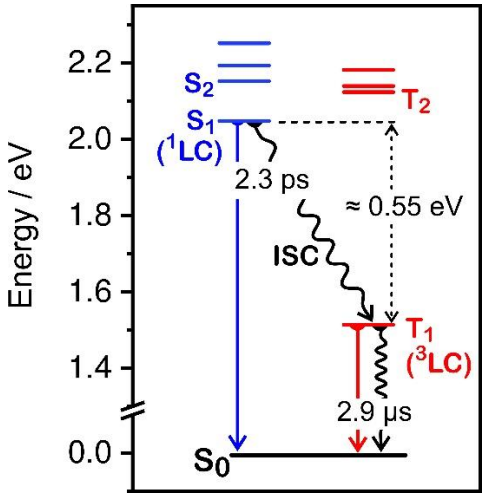

Figure 3.6. The simplified energy level diagram summarizing the photophysical properties of complex **IrIr** and computational data for the model structure **IrIr'**. (cf. ref.[69])

3.5 Application in bio-imaging. Complex **IrIr** was checked for suitability as a luminescent probe for live cell cultures. To study the cellular uptake and localization of the complex, human cancer HeLa cells were used. The emission from biological samples was detected by confocal luminescence microscopy. Despite some precipitation of the complex in the culture medium, **IrIr** stained the HeLa cells. Confocal microscopy images shown in Figure 3.7 confirm the uptake.

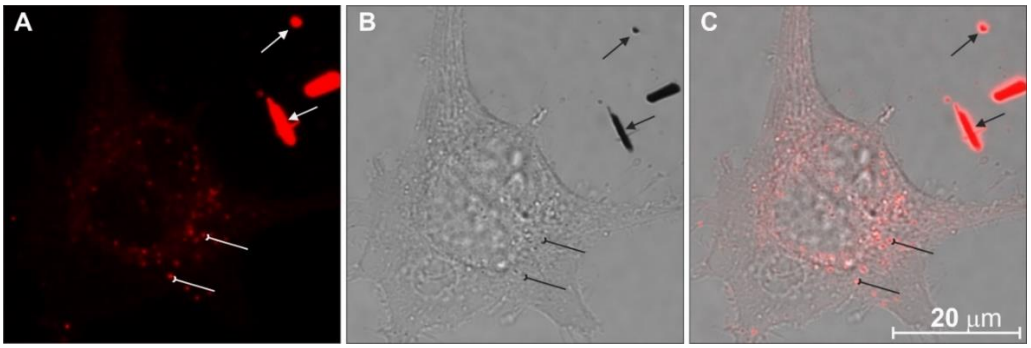

Figure 3.7. Cellular distribution of **IrIr** in fixed HeLa cells. (A) Luminescence of **IrIr**. (B) Transmitted light image. (C) Merged image of (A) and (B). Vesicles with **IrIr** cargo in the cytoplasm - inverted arrow. Precipitated **IrIr** outside the cell – arrow. (cf. ref.[69])

Co-staining experiments using 4′,6-diamidino-2-phenylindole (DAPI) and 3,3′-dihexyloxacarbocyanine iodide (DiOC6) as standard fluorescence probes for double-stranded DNA (in nucleus and mitochondria) and membrane structures (endoplasmic reticulum, vesicle membranes, mitochondria), respectively, reveal significant accumulation of **IrIr** in intracellular vesicles. In Figure 3.8, **IrIr**-loaded vesicles scattered throughout the volume of cytoplasm and vesicles near the nuclear envelope are marked with inverted arrows and empty arrowheads, respectively.

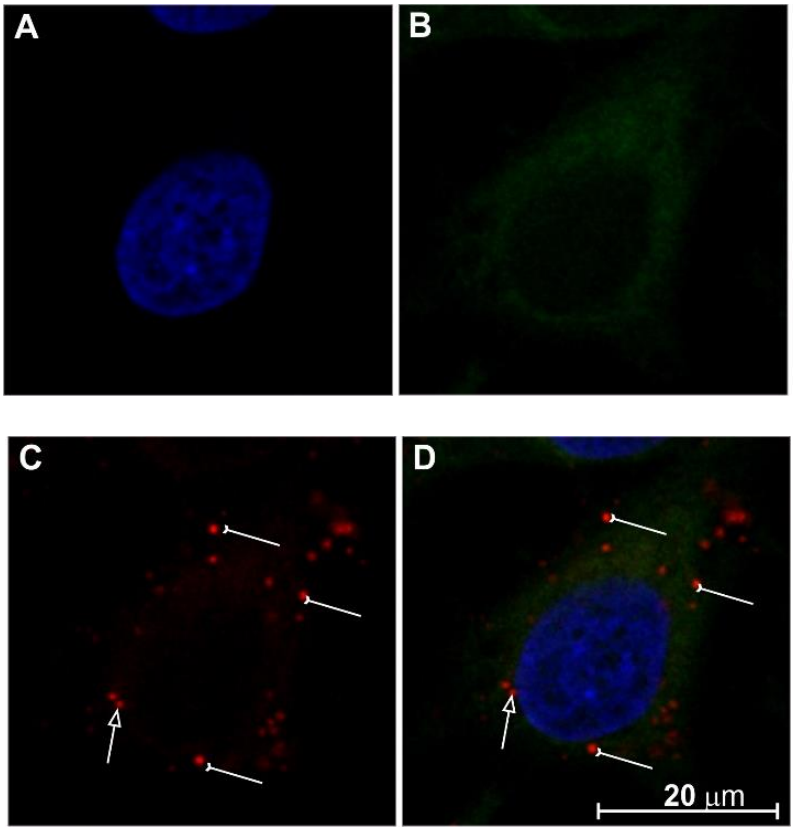

Figure 3.8. Co-staining experiment of **IrIr** with DAPI and DiOC6. Luminescence of DAPI (A). Luminescence of DiOC6 (B). Luminescence of **IrIr** (C). (D) Merged image of (A), (B) and (C). Vesicles with **IrIr** cargo in cytoplasm - inverted arrow, vesicles with **IrIr** cargo attached to nuclear envelope - empty arrowhead. (cf. ref.[69])

Thus, the experiments demonstrate that **IrIr** is uptaken by the HeLa cells. It is localized mostly in the cytoplasm as a vesicle cargo within the network of the endoplasmic reticulum. However, there is no evidence of **IrIr** transports to the nucleus. The complex shows a rather low solubility in aqueous media which requires further optimisations of the molecular structure to improve the solubility in polar media.

3.6 Concluding remarks. The dinuclear Ir(III) complex **IrIr** shows deep-red/NIR phosphorescence that is accompanied by weak green fluorescence stemming from S_1 state as measured in dichloromethane at ambient temperature. The unusual occurrence of fluorescence in steady-state spectra is due to a relatively slow ISC with the measured rate of about $k_{ISC}(S_1 \rightarrow T_1) = 4.3 \times 10^{11}$ s^{-1}. This is a consequence of the strong ligand centered (LC) character of the S_1 and T_1 excited states, relatively large energy gap $\Delta E(S_1–T_1)$, and high energy of the higher triplet states (T_2, T_3…) respective to state S_1. Such an unusual electronic structure and, consequently, photophysical behavior of **IrIr**, are due to the strongly π-excessive character of the chromophoric

bridging ligand. This results in the predominant LC character of the lowest excited states S_1 and T_1, both of HOMO→LUMO origin, giving a large energy gap $\Delta E(S_1–T_1)$. Therefore, the SOC and vibrational coupling of states S_1 and T_1 is relatively weak which results in a slow ISC $S_1 \rightarrow T_1$. These findings, in comparison to those in Chapters 1 and Chapter 2, demonstrate the high importance of the chromophoric ligand's design for the photophysical properties of the complex. In particular, the π-excessive ligands play for the reduction of the efficiency of SOC of the lowest excited states thus reducing the rates of the SOC-dependent processes.

The emission quantum yield of **IrIr** of Φ_{PL} = 3.5 % is relatively high among other NIR phosphorescent Ir(III) complexes.[70,72-76] For example, mononuclear Ir(III) complexes of oligothienylpyridine, also exhibiting red to NIR phosphorescence, were characterized with much lower photoluminescence quantum yields of Φ_{PL} < 1 %.[71] Internalized by live HeLa cells, the NIR phosphorescence of **IrIr** can be efficiently detected in biological samples using confocal microscopy which shows the design motif of the complex as promising for the construction of NIR luminescent molecular probes.

4. Dinuclear molecular design to afford fast and efficient red phosphorescence

As it is seen from the results of Chapters 1, 2 and 3, the dinuclear motif of the molecular structure can indeed be advantageous for the design of efficient Ir(III) phosphors. This is a tempting approach to the design-wise challenging class of materials showing efficient and fast phosphorescence in the red optical range. However, the chromophoric ligand should be judiciously chosen to not be strongly π-excessive as otherwise, it would increase the LC character of the T_1 state diminishing its SOC with the singlet states and, consequently, result in a relatively low rate of $T_1 \rightarrow S_0$ phosphorescence. Therefore, it seems rational to consider complexes with chromophoric ligands comprising π-deficient heterocycles. For this purpose, two new Ir(III) complexes **Ir-1** and **Ir-2** (Chart 4.1) were investigated. **Ir-1** and **Ir-2** feature mono- and dinuclear design, respectively, allowing to once again assess the advantages of dinuclear design in a comparative study. In mononuclear **Ir-1**, the N^C^N coordinating ligand with two terminal π-deficient pyridine derivatives, expected to accommodate the LUMO of the complex. Similarly, in dinuclear **Ir-2** the LUMO is expected to localize on and the ditopic (bridging) N^C^N−N^C^N coordinating ligand containing two terminal π-deficient pyridine derivatives and a central strongly π-deficient 1,3-pyrimidine derivative. The HOMO of both complexes is expected to be strongly contributed by the metal centers. Thus, the lowest excited states of **Ir-1** and **Ir-2** are expected to have strong Metal-to-Ligand Charge Transfer (MLCT) character which was shown as advantageous for $T_1 \rightarrow S_0$ phosphorescence rate in the preceding chapters as well as in literature.[14]

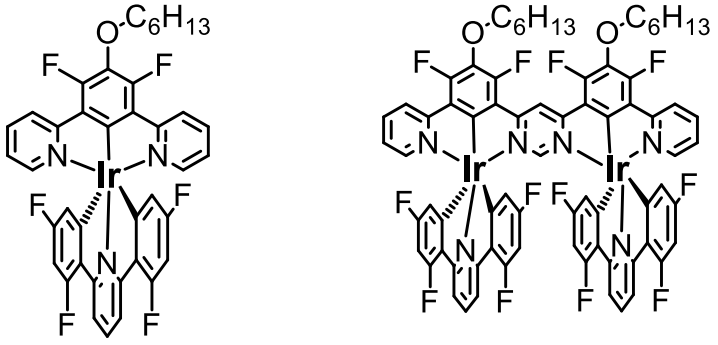

Ir-1 **Ir-2**

Chart 4.1. Chemical structures of complexes **Ir-1** and **Ir-2**. For synthetic details see ref.[91]

4.1 X-ray diffraction analysis. Crystals of **Ir-1** and **Ir-2** suitable for x-ray diffraction (XRD) analysis were grown by slow convectional diffusion of methanol into a solution of the corresponding complex in dichloromethane. The details of the XRD experiment are given in Section 7.6. The XRD determined molecular structure of **Ir-1** shows the *quasi*-octahedral geometry of the coordination center (Figure 4.1a and Figure 7.7). The C^N^C ligand is coordinated

to the Ir(III) ion with bond length values of 2.082 Å and 2.087 Å for the two C–Ir bonds and 2.099(4) for the N–Ir bond (Table 8.12), which are longer compared to the coordination bonds found for the N^C^N ligand: 1.929 Å for the C–Ir bond and 2.055 Å for both N–Ir bonds. The larger values found for the C^N^C ligand are attributed to the two coordinating carbons exerting a strong *trans*-effect on each other which elongates both C–Ir bonds[17] compared to the cases with carbon atoms positioned *cis* to each other.[19,61]

The unit cell of complex **Ir-2** contains two independent molecules which, however, are very similar (Table 8.13). The structure of **Ir-2** comprises two octahedral Ir(III) centers bridged by the ditopic ligand and each coordinated to a C^N^C ligand (Figure 4.1b and Figure 7.8). The coordination center geometry parameters of **Ir-2** are comparable to those of the complex **Ir-1.** The plane of bridging N^C^N−N^C^N ligand is slightly bent and twisted. The two C^N^C ligands are in a wedge-shaped configuration where the two are slightly shifted in respect to each other. This distorted geometry is the result of the steric confinement of the two C^N^C ligands. It is noteworthy that geometrically the oxygen atoms of the alkoxy chains of the N^C^N coordinating ligands in both complexes are out of the π-conjugation with the aromatic system, which electronically makes them rather more σ-acceptors than π-donors.

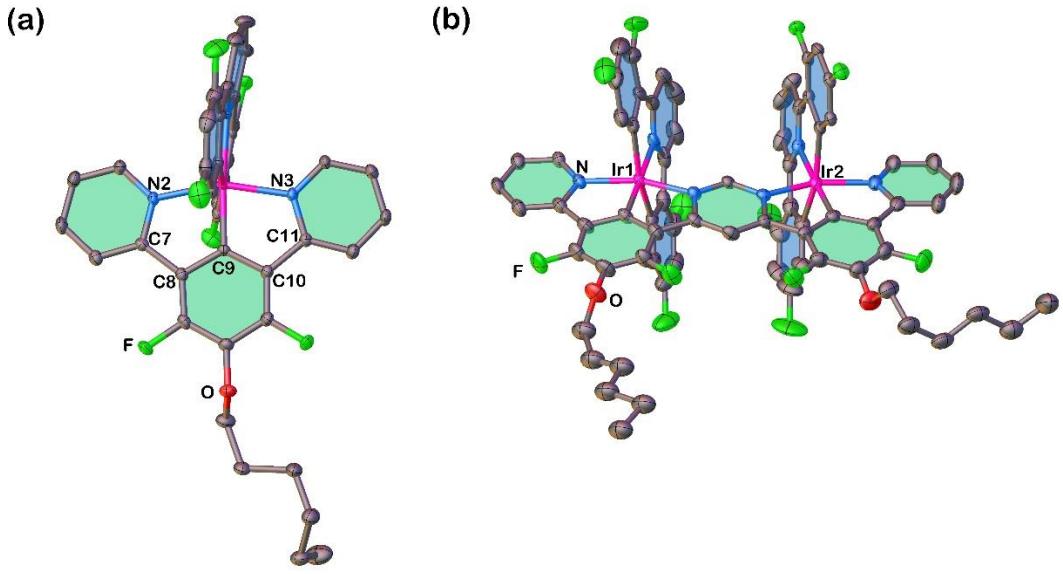

Figure 4.1. XRD determined molecular structure of complex **Ir-1** (a) and complex **Ir-2** (b) in the crystal. Thermal ellipsoids are shown at the 50% probability level. (cf. ref.[91])

4.2 Optical spectroscopy. Absorption spectra measured at ambient temperature for a toluene solution of complex **Ir-1** features a series of relatively low-intensity bands in the range 350 nm ≤ λ ≤ 480 nm (Figure 4.2a). With the help of TD-DFT calculation, these bands are assigned to excited states of mixed Metal-to-Ligand Charge Transfer character, involving d-orbitals of Ir(III) center

and π* orbital of the N^C^N ligand (denoted as ^{1}MLCT or ^{1}dπ*), and ligand centered character (LC or ππ*). The gradual intensification of the absorption at λ < 350 nm is assigned to the increasing dominancy of the ^{1}LC character of the associated excited states. The absorption of complex **Ir-2** measured under the same conditions extends to lower energies and covers the range of up to λ ≈ 600 nm, which is a result of a significantly larger π-electronic system of the N^C^N−N^C^N ligand of **Ir-2** as compared to the ligands of **Ir-1**. Similar to complex **Ir-1**, the series of lower energy absorption bands of **Ir-2** covering the spectral range 350 nm ≤ λ ≤ 600 nm are assigned to states of mixed ^{1}MLCT/^{1}LC character while the bands with λ < 350 nm are assigned to the excited states of predominant ^{1}LC character. These assignments are also in agreement with the TD-DFT calculations discussed below. It is important to mention that the lowest energy absorption band of complex **Ir-2** with λ_{max} = 602 nm, assigned to $S_0 \rightarrow S_1$ transition, is unusually intense ($\varepsilon \approx 3.4\times10^4$ $M^{-1}cm^{-1}$) for a transition of decent ^{1}MLCT character. The seeming anomaly, however, can be explained by the symmetric structure of complex **Ir-2**. This effect, brought by dinuclear design, was noted in Chapter 1 comparing mononuclear **IrCl** and dinuclear **Ir$_2$Cl$_2$**, and also has been reported for other dinuclear complexes.[19,92]

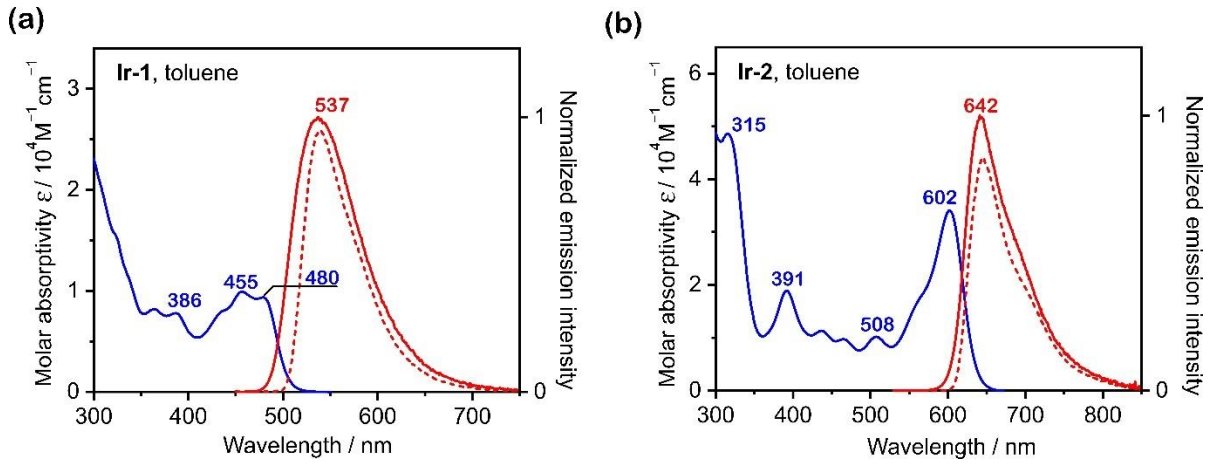

Figure 4.2. Absorption spectrum at T = 300 K (blue) and emission (red) spectra of **Ir-1** (a) and **Ir-2** (b) at T = 300 K (solid line) and at T = 77 K (dashed line) in toluene. (cf. ref.[91])

In complex **Ir-2**, due to the constructive coupling of the light-induced electronic oscillations at the two sides, the magnitude of transition dipole moment (μ($S_0 \rightarrow S_1$)), directed along the bridging ligand (y-axis in C_{2v} symmetry molecules) can be up to twice as large compared to mononuclear complex **Ir-1**. This can give up to a four-fold increase in the f($S_0 \rightarrow S_1$) oscillator strength.[3] This effect is discussed in more detail in the computational part below.

The emission measured for the toluene solution of complex **Ir-1** under ambient conditions appears in green spectral range with the maximum at λ_{max} = 537 nm (Figure 4.2a). The emission

quantum yield and decay time, measured for degassed sample ($c \approx 10^{-5}$ M) amount to $\Phi_{PL} = 0.15$ (15 %) and $\tau = 1$ µs (Figure 4.3), respectively. These values give radiative decay time of $\tau^r = \tau/\Phi_{PL} = 6.67$ µs, radiative rate of $k_r(300K) = \Phi_{PL}/\tau = 1.5\times10^5$ s^{-1} and non-radiative decay rate of $k_{nr}(300\ K) = (1-\Phi_{PL})/\tau = 8.5\times10^5$ s^{-1}. Measured for the doped polystyrene (PS) film at room temperature, the emission quantum yield of **Ir-1** increases significantly to $\Phi_{PL} = 55$ %, which is primarily due to the reduction of the non-radiative relaxation rate as seen from the values in Table 4.1. The relatively more rigid media of polystyrene may suppress the geometry reorganisations in the emitting state thus diminishing the vibrational overlap of the emitting and ground states that results in a slower non-radiative relaxation of the emitting state. The relatively blue-shifted emission maximum in the PS film (532 nm), compared to that in toluene (537 nm), might be the sign of such suppression of geometry reorganisations. Besides reducing the vibrational overlap of the emitting and ground states, the suppressed geometry reorganisations in the emitting state may also reduce the population efficiency of a higher laying quenching state of metal centered excitation character (MC or dd*), [93-96] which would also play for a decrease of non-radiative relaxation rate of the emitting state.

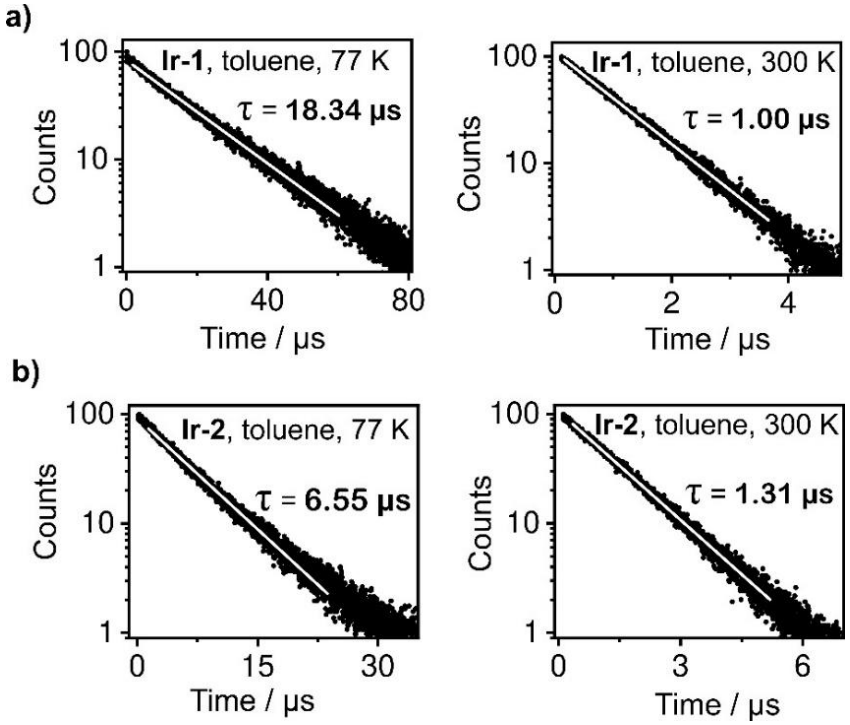

Figure 4.3. Emission decay profiles measured for **Ir-1** (a) and complex **Ir-2** (b) both in toluene ($c \approx 10^{-5}$ M) at T = 77 K and degassed solution at T = 300 K. The temperatures are indicated in the insets. (cf. ref.[91])

The emission of complex **Ir-2** in toluene measured at room temperature appears in the red spectral range with $\lambda_{max}(300\ K) = 642$ nm (Figure 4.2). The corresponding emission quantum yield

and decay time values, measured for a degassed sample ($c \approx 10^{-5}$ M), amount to $\Phi_{PL} = 0.80$ (80 %, Table 1) and $\tau = 1.31$ μs (Figure 4.3), respectively, which gives radiative decay time of $\tau^r(300\ K) = \tau/\Phi_{PL} = 1.64$ μs, radiative rate of $k_r(300\ K) = \Phi_{PL}/\tau = 6.1\times10^5\ s^{-1}$ and non-radiative rate of $k_{nr}(300\ K) = (1-\Phi_{PL})/\tau = 1.5\times10^5\ s^{-1}$ (Table 4.1). The calculated radiative rate value is remarkably high for a red-emitting Ir(III) complex.[14,42] Typically, the emission of Ir(III) complexes represents phosphorescence stemming from the T_1 state which owes to the metal-induced spin-orbit coupling (SOC) effect. The $T_1 \rightarrow S_0$ character of emission also fits the photophysical properties of **Ir-1** and **Ir-2** as the τ^r value in the microsecond time range is a fingerprint of phosphorescence. However, as will be discussed below, the emission of **Ir-1** and **Ir-2** at room temperature is probably also contributed by thermally activated excited state(s) energetically lying above the state T_1.

The photoluminescence properties of **Ir-2** in PS film at room temperature are comparable to those in toluene. The more rigid media of PS film causes only a slight increase of quantum yield that is a result of both, a slightly increased radiative rate and a slightly decreased non-radiative rate (Table 4.1). This contrasts the case of **Ir-1**, for which at room temperature the non-radiative relaxation rate in toluene is found to be much higher than in PS film. Also, at room temperature, the non-radiative rate of **Ir-1** in toluene is several times higher than that of **Ir-2** (Table 4.1). Recalling the energy gap law[15], the slower non-radiative relaxation in the case of **Ir-2** with a lower energy emitting state, compared to **Ir-1**, is counterintuitive. Such a stark decrease of non-radiative relaxation rate in **Ir-2** might be due to two effects: (i) high molecular rigidity brought by the dinuclear design of **Ir-2** with two spatially hindered N^C^N ligands; (ii) larger energy gap between the emitting state and the higher laying quenching state of metal centered character(dd*)[93-96] so that the population efficiency of the latter is diminished. Thus, the dinuclear design afforded a very unique combination of strongly red-shifted emission with several times higher radiative rate and strongly suppressed non-radiative relaxation of the emitting state, compared to the mononuclear analogue.

At T = 77 K the emission of **Ir-1** in toluene ($c \approx 10^{-5}$ M) peaks at $\lambda = 540$ nm (Figure 4.2) with the quantum yield reaching unity, and decay time of $\tau = \tau_r = 18.34$ μs. The corresponding radiative rate constant amounts to $k_r = 0.55\times10^5\ s^{-1}$ that is notably lower than at T = 300 K (Table 4.1). The fact that the quantum yield of **Ir-1** increases with lowering the temperature, despite the decrease in radiative rate shows that non-radiative deactivation of the state T_1 at in the frozen medium at T = 77 K becomes suppressed. This effect is similar to the reduction of the non-radiative rate from toluene to the rigid media of PS film at room temperature that was discussed above.

Complex **Ir-2** measured in toluene ($c \approx 10^{-5}$ M) at T = 77 K shows emission with the maximum at $\lambda = 645$ nm, quantum yield of $\Phi_{PL}(77\ K) = 0.9$ and decay time of $\tau(77\ K) = 6.55$ μs. This gives the radiative decay rate value $k_r(77\ K) = 1.37\times10^5\ s^{-1}$ and non-radiative decay rate value $k_{nr}(77\ K)$

= 0.15×10^5 s^{-1}. The decrease of the radiative rate with a decrease in temperature, found for both **Ir-1** and **Ir-2**, is associated with the decreasing thermal population efficiency of the higher laying and faster-emitting substates of T_1 and, probably, also of the state(s) lying above T_1 which will be discussed in detail below.

Table 4.1. Summary of photophysical data of **Ir-1** and **Ir-2** in toluene ($c \approx 10^{-5}$ M) and doped in polystyrene (PS) film. The films were processed from polystyrene and the complex (wt.% < 1) dissolved in toluene. The absorption was measured for toluene solution at T = 300 K. For the emission quantum yield and decay time measurements at T = 300 K the toluene solutions were degassed and polystyrene films kept under the nitrogen atmosphere. (cf. ref.[91])

		Ir-1	**Ir-2**
Absorption	λ_{max}/nm (ε/$M^{-1}cm^{-1}$)	480 (9300), 455 (9900), 386 (7800), 365 (8200), 280 (35000).	602 (34100), 507 (10200), 465 (9700), 437 (11300), 391 (18900), 315 (48600).
Photoluminescence	λ_{max}/nm	537	642
Toluene, T = 300 K	τ (τ_r)/μs*	1.00 (6.67)	1.31 (1.64)
	Φ_{PL} / %	15	80
	$k_r/10^5$ s^{-1}	1.50	6.11
	$k_{nr}/10^5$ s^{-1}	8.50	1.53
Photoluminescence	λ_{max}/nm	540	645
Toluene, T = 77 K	$\tau(\tau_r)$/μs*	18.34 (18.34)	6.55 (7.28)
	Φ_{PL}/%	100	90
	$k_r/10^5$ s^{-1}	0.55	1.37
	$k_{nr}/10^5$ s^{-1}	≤ 0.016	0.15
Photoluminescence	λ_{max}/nm	532	637
PS film, T = 300 K	τ (τ_r)/μs*	3.40 (6.20)	1.20 (1.33)
	Φ_{PL}/%	55	90
	$k_r/10^5$ s^{-1}	1.62	7.5
	$k_{nr}/10^5$ s^{-1}	1.32	0.83

*τ_r – radiative decay time calculated as $\tau_r = \tau/\Phi_{PL} = 1/k_r$ where Φ_{PL} is taken as a fraction of unity, e.g., 15 % = 0.15.

The obtained photophysical characteristics show a four-fold increase in the radiative rate of emission from the mononuclear complex **Ir-1** to the dinuclear complex **Ir-2**. This possibly is associated with a more efficient SOC of the state T_1 with singlet states in complex **Ir-2** and hence comparatively more relaxed $\Delta S = 0$ rule for $T_1 \rightarrow S_0$ transition. To obtain more detailed characteristics of the emitting state, the emission decay of each **Ir-1** and **Ir-2**, was investigated at cryogenic temperatures and the obtained decay times values were also analyzed with the Boltzman type Eq. 1.1, as it was done complexes **IrCl**, **Ir_2Cl_2** and **Ir_2I_2** discussed in above.

In each case, **Ir-1** and **Ir-2**, Eq. 1.1 was fitted to the decay time values measured in the temperature range of $1.7K \leq T \leq 120$ K, with parameter $\tau(I)$ fixed to the experimental value obtained at T = 1.7 K. The best fit obtained for complex **Ir-1** with $\tau(I) = 192$ µs suggests the individual substate II and III decay times of $\tau(II) = 65.6$ µs and $\tau(II) = 3.6$ µs and energy gaps of $\Delta E(II-I) = 5$ cm^{-1} and $\Delta E(III-I) = 50$ cm^{-1}. The best fir obtained for the dinuclear complex **Ir-2** with $\tau(I) = 120$ µs suggests decay time values of $\tau(II) = 7.0$ µs and $\tau(II) = 1.0$ µs and energy gaps of $\Delta E(II-I) = 30$ cm^{-1} and $\Delta E(III-I) = 90$ cm^{-1} (Figure 4.4).

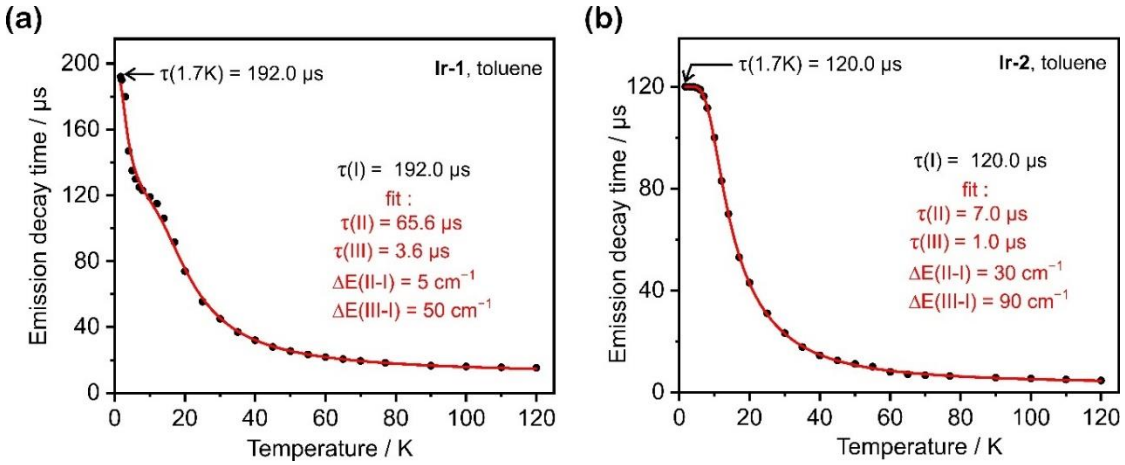

Figure 4.4. Emission decay times plotted as a function of temperature (black dots), and the best fit of Eq. 4.1 to the experimental values (red line) of complex **Ir-1** (a) and complex **Ir-2** (b). (cf. ref.[91])

The notably larger zero-field splitting (ZFS) ($\Delta E(III-I)$) found for the dinuclear complex **Ir-2** is rationalized by a stronger SOC of state T_1 with other states, which, according to the comparatively shorter decay times of the T_1 substates I, II and III, must be contributed by singlet states. Such an influence of the dinuclear structure on the SOC efficiency of state T_1 and, consequently, on its photophysical properties is in line with the results of Chapter 1.

Interestingly, extrapolation of the decay time values obtained for T_1 substates of complex **Ir-1** to the temperature T = 300 K via Eq. 1.1 results in the average decay time of 11.58 µs that is

about twice as large compared to the experimentally obtained value of τ_r(300K) = 6.67 μs in toluene and τ_r(300K) = 6.20 μs in PS film (Table 4.1). This contrasts complexes **IrCl**, **Ir_2Cl_2**, **Ir_2I_2** discussed earlier and complex **IrPt** discussed in Chapter 5 below, for which the properties of T_1 substates predict emission decay time at T = 300 K similar to the experimentally measured value or even shorter. Analogous to the case of **Ir-1** deviation of the predicted and measured emission decay time values is also found for complex **Ir-2**. In this case, the characteristics of T_1 substates, suggested by the fit of Eq. 1.1 predict the average emission decay time at T = 300 K to be of τ = 3.22 μs, whereas the measured radiative decay time, is only of τ_r(300 K) = 1.64 μs in toluene and τ_r(300K) = 1.33 μs in PS film (Table 4.1). Such an unusual photophysical behavior exhibited by complexes **Ir-1** and **Ir-2** could be explained by the thermal population of the state(s) energetically lying above the state T_1 which contribute to the emission increasingly with temperature. As estimated from the deviation of the experimental τ_r(300 K) value and the average decay time value approximated from decay times of T_1 substates for T = 300 K via Eq. 1.1., the emission intensity contribution of this fourth state could be approaching 50 %. This model was approximated by fitting the experimental decay time values of **Ir-1** and **Ir-2** with to the four-level model described by Boltzmann type Eq. 2.1, which was applied in Chapter 2 to analyze the properties of **Ir_2I_2**.

The fitting was done with the τ(I) parameter fixed to the experimental value and with the parameters τ(II), τ(III), ΔE(II−I) and ΔE(III−I) fixed to values determined by the best fit of the three-level model of Eq. 1.1 (Figure 4.4). The experimental data point for T = 300 K in the case of complex **Ir-1** was fixed to τ^r(300K) = 6.67 μs and in the case of complex **Ir-2** was fixed to τ^r(300 K)×0.9 = 1.47 μs as in this case the cryogenic temperature decay time values are assumed to correspond to the emission quantum yield of Φ_{PL}(77 K) = 90 %. The best fit of the four-level model (Eq. 2.1) suggests the fourth state parameter values of ΔE(IV−I) ≈ 1700 cm^{-1} and τ(IV) ≈ 0.002 μs (2 ns) for complex **Ir-1**, and of ΔE(IV−I) ≈ 1000 cm^{-1} and τ(IV) ≈ 0.010 μs (10 ns) for complex **Ir-2**. There were no evidence to distinguish whether state IV is singlet (S_1) or triplet (T_2) state's substate(s), though it can be noted that according to TD-DFT calculations, the second-lowest excited state is S_1 in complex **Ir-1** and T_2 in complex **Ir-2** (Tables 8.16 and 8.17). The calculated triplet character of state IV of **Ir-2** is in line with it being predicted slower than state IV of **Ir-1** by the fit of Eq. 2.1 as otherwise, according to the several times larger extinction coefficient of S_1←S_0 transition in **Ir-2**, the state IV of **Ir-2** should have been predicted several times faster than state IV of **Ir-1**. However, the 10 ns decay time still seems extraordinarily short for a triplet state and may be contributed by the S_1 (1.794 eV) state which is calculated to lay nearby the state T_2 (1.789 eV). Therefore, it should be noted that in both cases, **Ir-1** and **Ir-2**, the obtained values τ(IV) and ΔE(IV−I) are rather rough and also may represent convoluted properties of two or more contributing (sub)states. The key point here, however, is that the room temperature emission of

both **Ir-1** and **Ir-2** is probably strongly contributed by the excited state(s) laying above the state T_1 with the intensity share close to 50 %. Such a photophysical behavior of **Ir-1** and **Ir-2** relates them with the materials characterized with thermally activated delayed fluorescence (TADF) where thermally populated state S_1 significantly enhances the emission rate with temperature increase.[54,97] This is also in line with the emission maximum of both **Ir-1** and **Ir-2** in liquid toluene at T = 300 K being rather close to and even slightly blue-shifted than that measured in frozen toluene medium at T = 77 K (Figure 4.2 and Table 4.1), which contrasts the phosphorescent complexes investigated in Chapters 1, 2 and 5. In **Ir-1** and **Ir-2** the better solvation of the T_1 state in liquid medium at T = 300 K, which is expected to cause red-shift of the spectrum, might be counteracted by more efficient thermal population of the state(s) laying above T_1, compared to that in the frozen medium at T = 77 K.

4.3 DFT and TD-DFT computations. To gain a deeper insight into the photophysical properties of complexes **Ir-1** and **Ir-2**, a theoretical analysis of their electronic structures was conducted. The calculations were carried out for model structures **Ir-1'** and **Ir-2'** where, compared to the complexes **Ir-1** and **Ir-2**, respectively, the alkyl chains are truncated to methoxy groups to save computational time. The optimized ground state (S_0) geometries are in very good agreement with XRD determined geometries (Tables 8.12 and 8.13 in Section 8.2). The, S_0 state geometry obtained for the model complex **Ir-2'** reproduces the XRD determined geometry of complex **Ir-2** with the bent and twisted N^C^N−N^C^N bridging ligand and the wedge-shaped configuration of the C^N^C ligands. The TD-DFT calculations conducted for the S_0 geometries of **Ir-1'** and **Ir-2'** suggest absorption spectra comparable to the experimental ones obtained for **Ir-1** and **Ir-2** (Figure 7.6 in Section 7.4), which indicates a reliable simulation of the electronic structures.

As mentioned above, discussing the spectroscopic results, the $S_1 \leftarrow S_0$ absorption band of complex **Ir-2** is about four-fold more intense than that of complex **Ir-1** (Figure 4.2). According to the TD-DFT calculations carried out at the ground state geometries (S_0), the $S_1 \leftarrow S_0$ excitation has HOMO→LUMO origin in both **Ir-1'** and **Ir-2'** with the oscillator strengths of $f(S_0 \rightarrow S_1) = 0.1221$ for **Ir-1'** and to $f(S_0 \rightarrow S_1) = 0.3200$ for **Ir-2'**. Although these values do not exactly reproduce the experimentally found four-fold increase, the value calculated for **Ir-2'** is still drastically larger in comparison to the one of **Ir-1'**. Such a strong increase of the oscillator strength in the dinuclear structure could be explained using the symmetry principles. In the c_{2v} point group symmetry of **Ir-2,'** its HOMO (ϕ) and LUMO (ϕ') belong to the B_1 and A_2 irreducible representations, respectively (Figure 4.5). Then, the transition dipole moment (TDM, μ) of HOMO→LUMO transition must belong to the B_2 irreducible representation, so that the product $\phi \cdot \mu \cdot \phi'$ belongs to the totally symmetric irreducible representation A_1 and its integral over all the space (dr) does not cancel out, e.g., $\int \phi \cdot \mu \cdot \phi' dr > 0$. The TDM belonging to B_2 irreducible representation means its vector is directed

along the y-axis, that in case of **Ir-2'** is along the line containing the two coordination centers. Since the HOMO is symmetric to $\sigma_v(xz)$ operation, reflection at the plane bisecting the pyrimidine ring to two coordination sites (*quasi*-mononuclear parts) (Figure 4.5), the light-induced oscillations of the two sites along the y-axis can couple constructively thus increasing the TDM magnitude up to two times, which squared would result in up to a four-fold increase of the oscillator strength.[3]

As discussed in Chapters 1-3, $T_1 \rightarrow S_0$ phosphorescence, formally forbidden by spin selection rule $\Delta S = 0$, is promoted by the spin-orbit coupling (SOC) of the T_1 state with singlet states. The two states can have an efficient SOC if they comply with the electronic requirement that a particular Natural Transition Orbital (NTO) of both states (either the hole or electron) is contributed by the same heavy transition metal atom (such as Ir) but with atomic orbitals of different angular momentum (El-Sayed's rule[34]) orientations, whereas the other NTO is common for the two states.[24,34] Considering the Ir(III) complexes, the outer five 5d-orbitals of Ir(III) ion (d^6) are split by the (*quasi*)-octahedral ligand field to three occupied *quasi*-degenerate t_{2g} symmetry orbitals d_{xy}, d_{xz} and d_{zy}, and two unoccupied e_g symmetry orbitals d_z^2 and d_z^2-$_y^2$. This splitting results in the higher occupied orbitals of the Ir(III) complexes being strongly contributed by the three t_{2g} orbitals as seen for **Ir-1'** and **Ir-2'** in Figure 4.5 (also see Tables 8.14 and 8.15 in Section 8.2). According to the TD-DFT calculations, the T_1 states of both **Ir-1'** and **Ir-2'** are of HOMO→LUMO origin (Tables 8.16 and 8.17) and hence have a significant $^3d_i\pi^*$ (^{3}MLCT) character. Such triplet states can have effective direct SOC only with singlet states bearing $^1d_j\pi^{*\prime}$ (^{1}MLCT) character where $d_j \neq d_i$ and $\pi^* = \pi^{*\prime}$ as to fulfill the requirements posed above.

Electronic coupling of two coordination sites in the symmetric dinuclear structure of **Ir-2'** doubles the number of higher occupied molecular orbitals contributed by Ir(III) t_{2g} orbitals (Figure 4.5) as in the case of dinuclear $\mathbf{Ir_2Cl_2}$ considered in Chapter 1. Consequently, this doubles the number of singlet states ($^1d_j\pi^{*\prime}$) electronically suited for direct SOC with state T_1.[19,59,92] Indeed, analysis of the TD-DFT calculated singlet states within 1 eV above the T_1 state shows one such state for **Ir-1'**, S_5 (HOMO−1→LUMO), and two states, S_4 (HOMO−2→LUMO) and S_7 (HOMO−3→LUMO), for structure **Ir-2'**. Here, by the involved 5d-orbital, the HOMO−1 of **Ir-1'** is analogous to the pair HOMO−2 and HOMO−3 of **Ir-2'** where the last two orbitals differ only by symmetry as HOMO−2 is symmetric and HOMO−3 is antisymmetric with regard to C_2 rotation of **Ir-2'**. With twice the number of singlet states having SOC with the T_1 state, the dinuclear structure **Ir-2'** is expected to show a higher $T_1 \rightarrow S_0$ (phosphorescence) rate. Indeed, this is seen well comparing the decay time values which were determined above for the three T_1 substates of **Ir-1** and **Ir-2.** A similar conclusion can be reached comparing the measured radiative rates of **Ir-1** and **Ir-2** at either T = 77 K or T = 300 K (Table 4.1).[19]

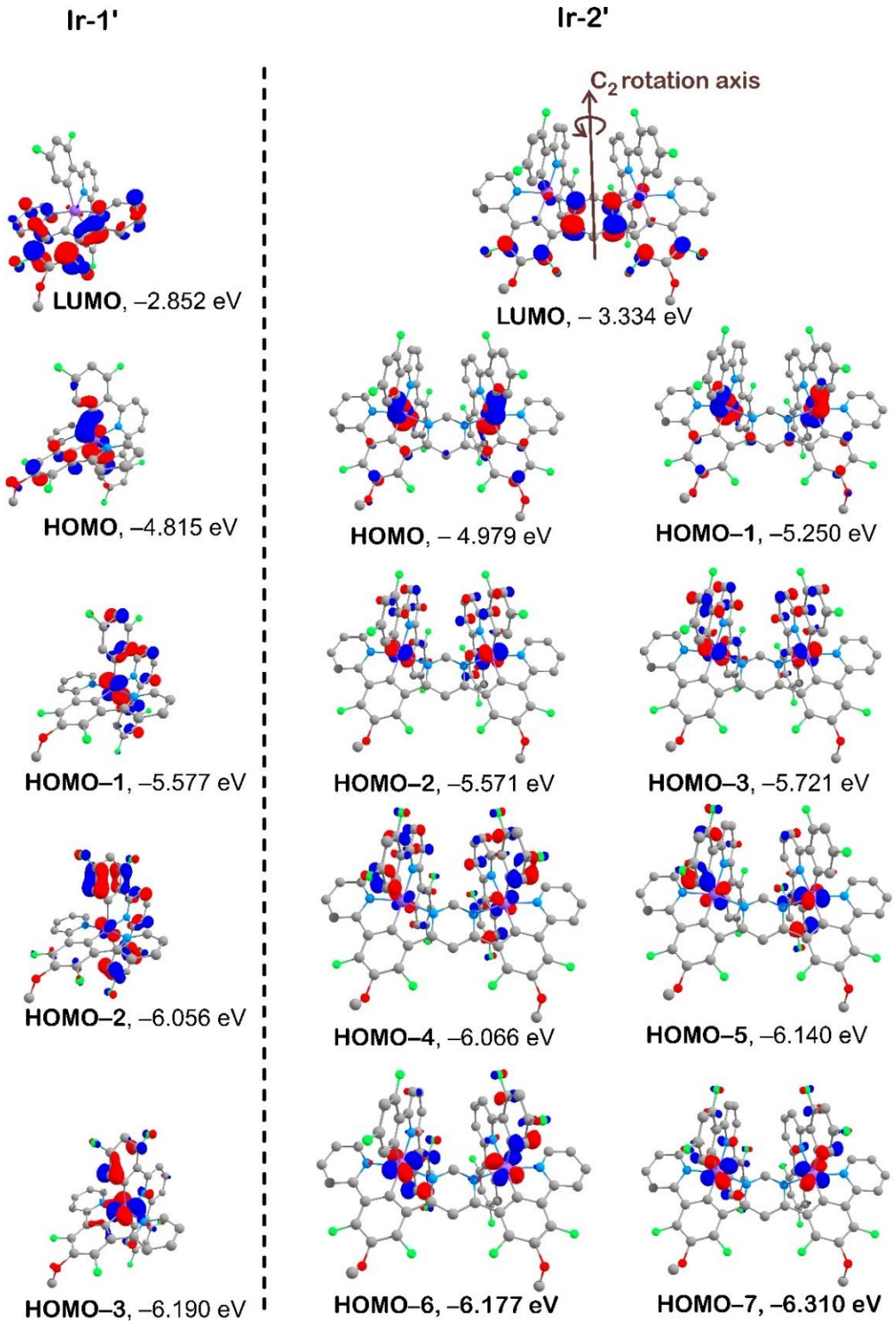

Figure 4.5. The iso-surface contour plots (iso-value = 0.05) of several selected Mos of model complexes **Ir-1'** and **Ir-2'** at the optimized T_1 state geometry. (cf. ref.[91])

4.4 Concluding remarks. The dinuclear molecular design with the judicious approach to the structure of the bridging ligand proved to be very effective to combine strong red-shift and enhanced rate of emission. The photophysical properties of the dinuclear complex **Ir-2** are

excellent. In degassed toluene solution under ambient temperature, **Ir-2** shows unusually fast and efficient red emission (λ_{max} = 642 nm) with a quantum yield of Φ_{PL} = 80 % and a radiative decay time of only τ_r =1.64 μs. For comparison, under the same conditions the analogous mononuclear complex **Ir-1**, emitting in the green optical range (λ_{max} = 537 nm), is less luminescent with Φ_{PL} = 15 % and τ_r = 6.67 μs. The relatively high emission efficiency of **Ir-2** is attributed to its dinuclear design which affords enhanced SOC of T_1 state with singlets, giving a relatively high oscillator strength $f(T_1 \rightarrow S_0)$, and rigid molecular structure, suppressing non-radiative relaxation processes. An important finding in photophysical properties of **Ir-1** and **Ir-2** is probable thermal activation of the excited state(s) lying above the state T_1 which further enhances the ambient temperature emission rates of the complexes. These are the first examples of Ir(III) complexes, showing photophysical behavior reminiscent of that of TADF materials.

5. Hetero-Dinuclear Ir(III)/Pt(II) design to afford intense red phosphorescence with sub-microsecond radiative decay time

Considering the complexes with dinuclear molecular structure as a design motif for efficient phosphors it is appealing to consider also the complexes containing different metal centers within one molecule. With this aim, an Ir(III)/Pt(II) hetero-dinuclear complex **IrPt**, synthesized for the mononuclear Ir(III) complex **Ir** (Scheme 5.1), was investigated.

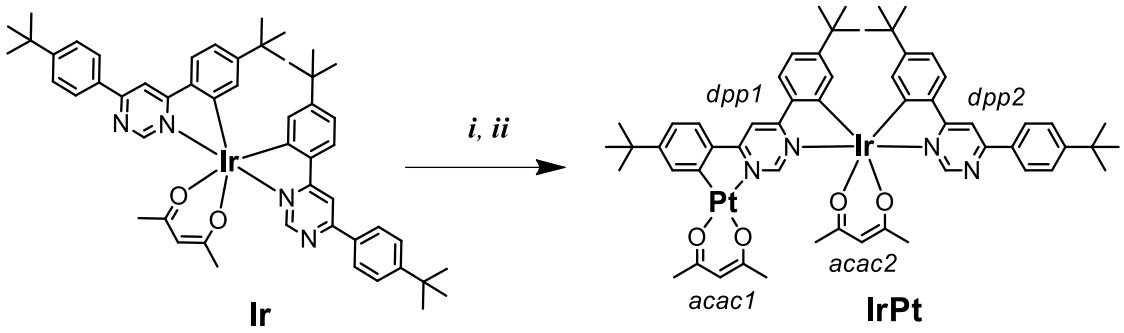

Chart 5.1. Synthesis of the hetero-dinuclear Ir(III)/Pt(II) complex **IrPt** from previously reported mononuclear Ir(III) complex **Ir**.[98] Reagents and conditions: i) K_2PtCl_4, AcOH, reflux, 48 h. ii) Na(acac), ethoxyethanol, reflux, 14 h.[61] (cf. ref.[61])

Complex **IrPt** comprises two metal centers, Ir(III) and Pt(II), that are bridged by a ditopic C^N−C^N coordinating 4,6-bis(4-(tret-butyl)phenyl)pyrimidine (H_2dpp) derivative further referred to as dpp1 ligand. The four coordinated Pt(II) is also chelated by an acetylacetonate (acac) ligand, referred to as acac1, whereas the six-coordinated Ir(III) center is coordinated to an additional monocoordinated H_2dpp derivative, referred to as dpp2, and an acac ligand, referred to as acac2. The use of dpp ligand comprising π-deficient 1,3-pyrimidine for this purpose is inspired by previously reported investigations[17], including Chapters 1 and 2 of this works, which demonstrate that the ligand affords a strong contribution of the metals to the HOMO of the complex and thus facilitates a strong MLCT character of the lowest excited states and, consequently fast phosphorescence. It is noted that a trinuclear complex of similar structure, with one Ir(III) center and two Pt(II) centers, has been reported earlier[98], but without detailed investigation of the photophysical properties and their interpretation from the electronic structure viewpoint.

5.1 X-ray diffraction analysis. Single crystals of complex **IrPt** suitable for XRD analysis were grown by slow diffusion of methanol into a solution of complex **IrPt** in dichloromethane. The corresponding coordination bond lengths and bond angles are reported in Table 8.18. The Pt(II) metal center exhibits a square planar geometry with the acac1 ligand and the opposite dpp1

ligand (see the structure in Chart 5.1 for identification of the different ligands). More specifically, acac1 is only slightly twisted from dpp1, as quantified by the O1-Pt-C1-C2 and O2-Pt-N1-C3 torsion angles of 172.8° and 176.9°, respectively (See Figure 5.1 for atom numbering). The Ir(III) metal center features an octahedral coordination geometry with the dpp2 ligand, the acac2 ligand and the dpp1 bridging ligand. The N2 atom of the dpp1 ligand and the N3 atom of the dpp2 ligand are in a *trans* configuration with an N2-Ir-N3 angle of 172.1°, while the C7 and C8 atoms are in a *cis* arrangement (Figure 5.1). The acac2 ligand has the O3 and O4 atoms in *trans* positions to C7 (dpp1) and to C8 (dpp2), respectively, with O3 being below and C8 above the plane of the dpp1 ligand in the perspective of Figure 5.1. The non-coordinated phenyl group of the dpp2 ligand is out of the coordination plane with a torsion angle N4-C11-C12-C13 of 28.4°. More details on the XRD experiment can be found in the Experimental part (Section 7.6).

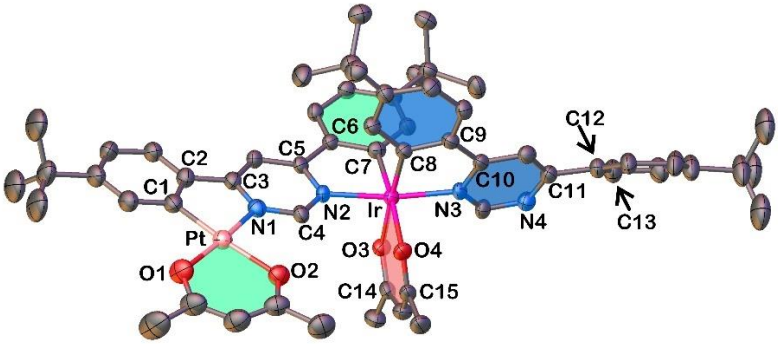

Figure 5.1. The molecular structure of complex **IrPt**, as determined by XRD on a single crystal**.** The thermal ellipsoids are shown at a 50 % probability level and hydrogens are omitted for clarity. (cf. ref.[61])

5.2 Optical spectroscopy. The absorption and photoluminescence spectra of complex **IrPt** in toluene at room temperature are shown in Figure 5.2, and key numerical data are summarized in Table 5.1. The absorption spectrum features three distinct regions, which, according to DFT calculations, can be interpreted as follows: (i) the low-intensity bands ($\varepsilon \approx 1\times10^4$ $M^{-1}cm^{-1}$) at wavelengths range $600 \geq \lambda \geq 500$ nm represent charge-transfer transitions from the Ir(III) center to the dpp1 and dpp2 ligands[60,99,100] and are assigned to $^1MLCT^{Ir(III)}$ states; (ii) the bands of average intensity ($\varepsilon \approx 2\times10^4$ $M^{-1}cm^{-1}$) at wavelengths range $500 \geq \lambda \geq 380$ nm originate from transitions either solely from the Pt(II) center or from a combination of the Pt(II) and Ir(III) centers to the dpp1 and dpp2 ligands, which are accordingly assigned to states of either $^1MLCT^{Pt(II)}$ or $^1MLCT^{Pt(II)/Ir(III)}$ character;[60,98,101] (iii) high-intensity bands with the averaged maxima at 326 nm are assigned to states of $\pi\pi^*$ character within the [dpp1-Pt-acac1] moiety and the dpp2 ligand with a minor contribution from a ligand-to-ligand charge-transfer (^{1}LLCT) transition (See Tables 8.19 and 8.20).

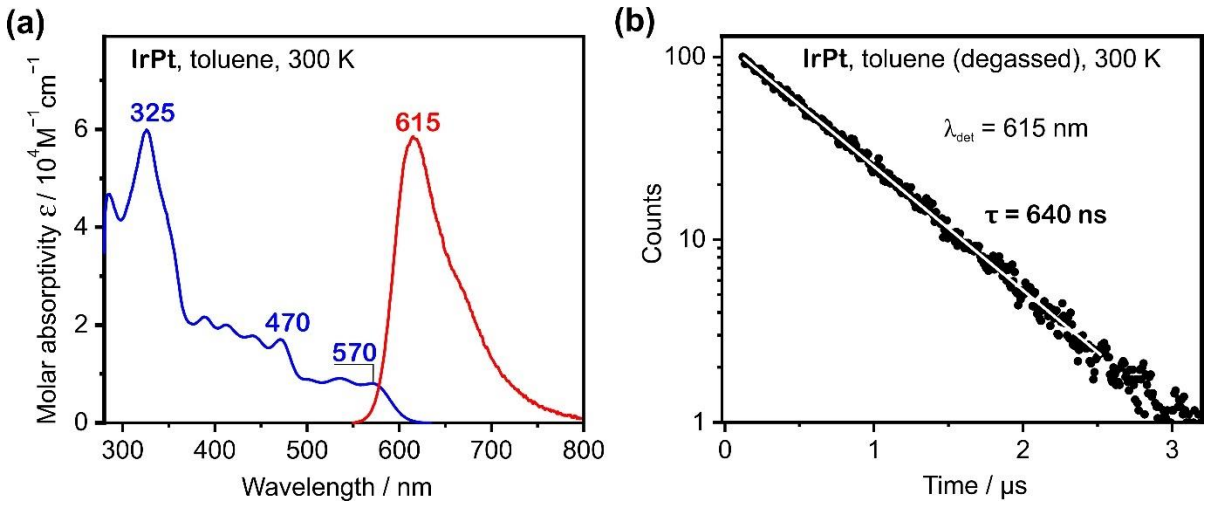

Figure 5.2. (a) Absorption (blue trace) and emission (red trace) spectra of **IrPt** in toluene under ambient conditions. (b) The emission decay profile of complex **IrPt** in degassed toluene ($c \approx 10^{-5}$ M) under ambient temperature. (cf. ref.[61])

The photoluminescence spectrum of complex **IrPt** (in toluene solution at room temperature) appears in the red spectral region, with the maximum at λ_{max} = 615 nm. This represents a notable red-shift in comparison to the starting mononuclear complex **Ir** that emits at λ_{max} = 585 nm.[98] The red-shift is rationalized as being the result of the extension of dpp1 ligand's π-conjugated system to the Pt(II) ion and the acac1 ligand, which decreases the HOMO–LUMO energy gap. The photoluminescence spectrum is broad and unstructured, which is characteristic for the emission from a charge-transfer state[17,23,60,98,101-104] due to a strong Franck-Condon coupling of the T_1 state and the ground state. The measured photoluminescence quantum yield of **IrPt** in degassed toluene at room temperature is very high at Φ_{PL} = 0.85 (85 %) with a sub-microsecond decay time of only τ(300 K) = 640 ns (Figure 5.2b). These values reveal an outstanding radiative rate (calculated as $k_r = \Phi_{PL}/\tau$) of $k_r = 1.33\times10^6$ s^{-1} that is an order of magnitude higher than of the fastest Pt(II) complexes[40,62] and notably higher than most other Ir(III) complexes.[15,23,104] This behavior shows the dominant role of the Ir(III) center in the properties of the T_1 state and the photoluminescent characteristics of complex **IrPt** which is supported by DFT calculations discussed below (Section 5.3). A radiative rate of similar magnitude has only been reported for Ir(III) complexes, primarily of dinuclear design.[16,17,19,38,59,60,98,101] It is noted that the high efficiency of phosphorescence is particularly valuable and hard to achieve for a red emitter. This is because Einstein's constant of spontaneous emission is inversely proportional to the cube of emission wavelength $(1/\lambda^3)^3$, and the non-radiative rate increases exponentially with decreasing energy gap between the emitting state and the ground state, as stated by the energy gap law.[15]

Table 5.1. A summary of key photophysical properties of complex **IrPt** in toluene ($c \approx 10^{-5}$ M). The emission quantum yield and decay time values reported for T = 300 K are measured for the degassed sample. (cf. ref.[61])

Absorption	570 (8043), 535 (9068), 503 (8800), 471
λ_{max}/nm	(17036), 441 (17783) 412 (20025), 389
(ε/$M^{-1}cm^{-1}$)	(21635), 326 (59917), 285 (46600)
Photoluminescence	
at T = 300 K	
λ_{max}/nm	615
Φ_{PL}	0.85
τ (τ_r)/μs*	0.64 (0.75)
$k_r/10^6$ s^{-1}	1.33
$k_{nr}/10^6$ s^{-1}	0.23
Photoluminescence	
at T = 77 K	
λ_{max}/nm	595, 645
Φ_{PL}/%	80
τ (τ_r)/μs*	8.80 (11)

*τ_r – radiative decay time calculated as $\tau_r = \tau/\Phi_{PL} = 1/k_r$.

The measured fast phosphorescence of complex **IrPt** implies a strong mixing of the T_1 state with the excited singlet states via SOC. The individual properties of the substates of state T_1 were analyzed by measuring the emission decay times at cryogenic temperatures, in the range $1.7 \leq T \leq 120$ K, similarly to the analysis conducted in previous chapters.

At temperature T = 1.7 K the decay time of **IrPt** is τ(1.7 K) = 81 μs (Figure 5.3), and it is assigned to the transition from the lowest T_1 substate I to the ground state, I→S_0.

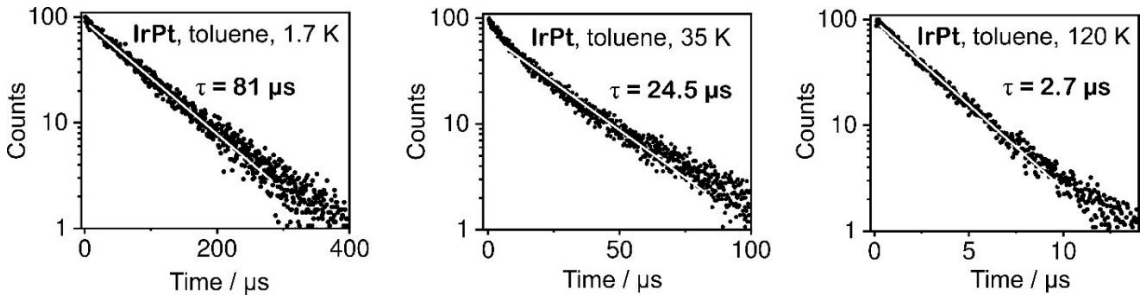

Figure 5.3. Emission decay profiles of **IrPt** in toluene ($c \approx 10^{-5}$ M) at temperatures indicated in the insets. (cf. ref.[61])

With the increase of temperature, the photoluminescence decay time decreases strongly. This is due to the thermal population of the higher triplet substate II and the opening of an additional transition channel II→S_0. In the temperature range of $20 \leq T \leq 40$ K, the decay time forms a *quasi*-plateau, with the average decay time of the substates I and II of $\tau(I/II) \approx 25$ µs measured at T = 35 K (Figure 5.3 and 5.4a). A further increase of the temperature is accompanied by a drop of the phosphorescence decay time by an order of magnitude to $\tau(120\ K) = 2.7$ µs (Figure 3e), which is due to the thermal population of the highest triplet substate III and the opening of the III→S_0 decay channel.

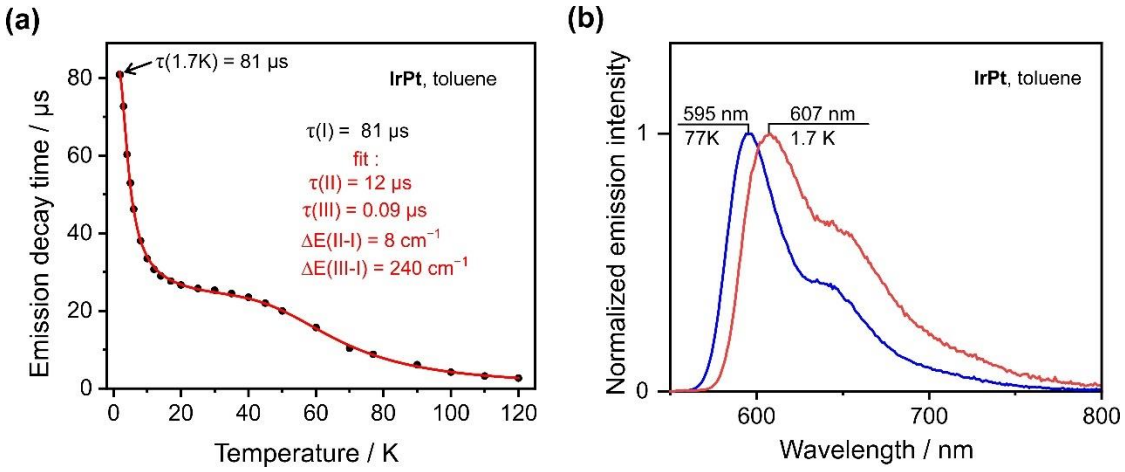

Figure 5.4. (a) Measured photoluminescence decay times of **IrPt** plotted as a function of temperature (black dots), and the best fit of eq. 2.1 to the experimental values (red line). (b) The PL spectra of **IrPt** in toluene at 1.7 K (red trace) and 77 K (blue trace). (cf. ref.[61])

This gradual population of higher and faster-emitting triplet substates II and III with increasing temperature is also traced from a notable blue-shift of the photoluminescence spectrum from T = 1.7 K (λ_{max} = 607 nm) to T = 77 K (λ_{max} = 595 nm) shown in Figure 5.4b. It is noted that the photoluminescence spectra taken in frozen media are blue-shifted compared to that measured in a liquid medium at T = 300 K which might be due to the better solvation of the excited state under the latter conditions (compare Figures 5.2a and 5.3b).

The photophysically important characteristics of the T_1 state were analyzed by fitting the emission decay time values obtained in the range $1.7 \leq T \leq 120$ K to the three-level model of Eq. 1.1 (Chapter 1). Analogously to the previously analyzed cases in this work, the parameter τ(I) was fixed to the value obtained experimentally at T = 1.7 K, τ(I) = 81 µs. The best fit, shown in Figure 5.4a, suggests substate II and III individual decay times of τ(II) = 12 µs and τ(III) = 0.09 µs, respectively, and energy gap values of $\Delta E(II-I) = 8\ cm^{-1}$ and $\Delta E(III-I) = 240\ cm^{-1}$. The T_1 state ZFS of 240 cm^{-1} is the largest reported so for an Ir(III) complex and may evidence particularly strong SOC of state T_1 with other states. The obtained individual decay times are comparatively short, especially for substate III. The decay time value as short as τ(III) = 0.09 µs show a

particularly large singlet admixture to substate III. Therefore, the record-breaking ZFS size of state T_1 of complex **IrPt** has to be strongly contributed by SOC to the singlet states. The diagram shown in Figure 5.5 summarizes the photophysical properties of **IrPt**.

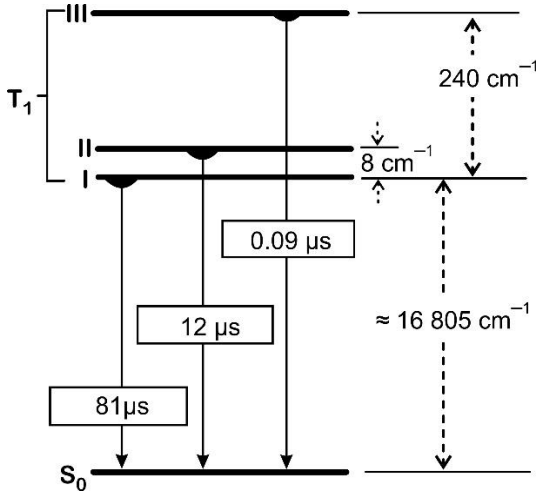

Figure 5.5. Simplified energy level diagram summarizing the photoluminescent properties of complex **IrPt**. (cf. ref.[61])

5.3 DFT and TD-DFT computations. The density functional theory (DFT) calculations were carried out on a model complex **IrPt'**, with the tret-butyl substituents of complex **IrPt** being truncated to methyl groups, to save computational time.

Coordination center bond lengths and angles of the S_0 and T_1 state optimized geometries are presented in Table 8.18. The geometry of the S_0 ground state is in very good agreement with the XRD-measured solid-state geometry of complex **IrPt**, as all of the coordination center bond lengths and almost all of the bond angles differ by less than 0.1 Å and 6°, respectively (Table 8.18). The only difference is for the non-coordinated phenyl group of the dpp2 ligand, which is in the coordination plane of the ligand for **IrPt'** in solution and out of the plane for **IrPt** in the crystal (see Figure 5.1). This difference can be attributed to the more relaxed environment in the solution as compared to the crystalline solid state.

The optimized geometry of the T_1 state differs from that of the ground state (S_0) primarily at the Ir(III) coordination center (Table 8.18, Section 8.2). Specifically, the N2-Ir-O3-C14 and N2-Ir-O4-C15 torsion angles in the T_1 state decreased by more than 20°, in comparison, which is indicative of a significant charge redistribution at the Ir(III) center between the ground state (S_0) and T_1 state. This is in line with the charge transfer character of the T_1 state involving Ir(III) center, as also suggested by the TD-DFT calculations discussed further below.

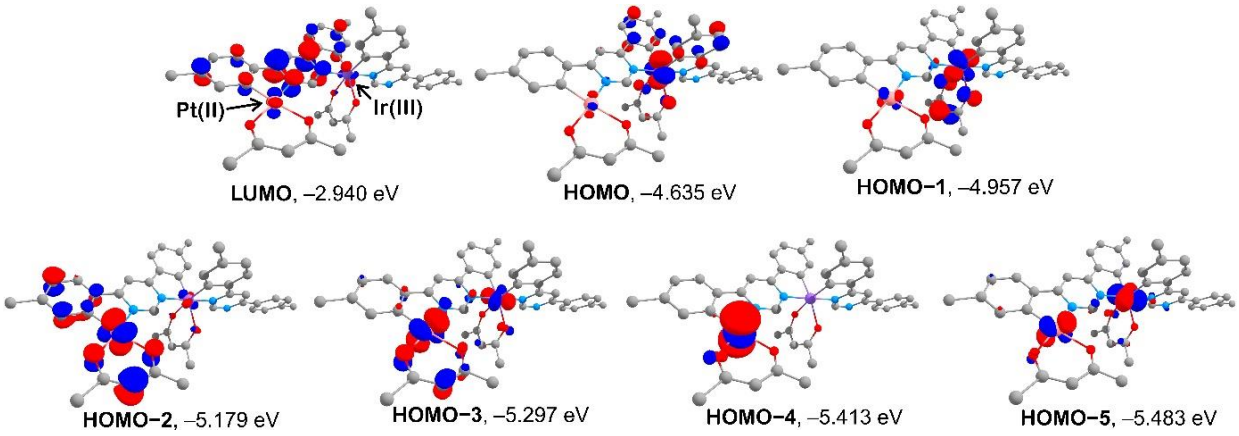

Figure 5.6. The iso-surface contour plots of several selected MOs of model complex **IrPt'** at T_1 state optimized geometry. (cf. ref.[61])

The SOC of state T_1 with singlets, opening the otherwise spin-forbidden phosphorescent $T_1 \rightarrow S_0$ transition is particularly strong at heavy transition metal atoms with large SOC constants (ζ_ℓ) such as Pt(II) ($\zeta_\ell = 4481$ cm^{-1}) and Ir(III) ($\zeta_\ell = 3909$ cm^{-1})[33] when the states of concern comply with the requirements based on El-Sayed's rule. According to the rule, state T_1 carrying $^3d_i\pi^*$ character can have efficient SOC with a singlet state carrying $^1d_j\pi^{*\prime}$ character when they are contributed by different d-orbitals of the same metal center e.g., $d_i \neq d_j$, where d_i and d_j belong to the same metal, and $\pi^* = \pi^{*\prime}$. This is to ensure the conservation of the total momentum of the electronic configuration at the spin-flip (for details see Section 8.1).

According to TD-DFT calculations, state T_1 of **IrPt'** has HOMO→LUMO origin, where HOMO is strongly contributed by an Ir 5d orbital (d_i), whereas the LUMO is largely represented by a π^* orbital localized on the dpp1 ligand (Figure 5.6). Thus, according to these data, the triplet state T_1 can be assigned a Metal-to-Ligand Charge Transfer character ($^3MLCT^{Ir(III)}$) involving the Ir(III) center that can also be denoted as a $^3d_i\pi^*$ excited state. State T_1 of **IrPt'** can spin-orbit couple with close in energy singlet states contributed by a HOMO–n→LUMO transition where HOMO–n (n > 0) is an occupied orbital contributed by the Ir atom and different from HOMO (for $d_i \neq d_j$). Analysis of the TD-DFT data shows that within 0.5 eV energy gap state T_1 can couple via SOC with state S_1 (has 3% contribution from HOMO–1→LUMO transition) and state S_3 (has 92% contribution from HOMO–1→LUMO transition). State S_2 contributed solely by HOMO→LUMO+1 transition does not fulfill $d_i \neq d_j$ and $\pi^* = \pi^{\prime *}$ requirements to have direct SOC with state T_1. According to the electronic origin of state S_3, its SOC with state T_1 at the Ir center is expected to be particularly strong, which, due to a comparatively high oscillator strength ($f(S_0 \rightarrow S_3) = 0.0707$), would well enhance the oscillator strength $f(T_1 \rightarrow S_0)$ and hence the radiative rate $k_r(T_1 \rightarrow S_0)$.[31] Interestingly, along with the Iridium center the requirements for efficient SOC of state T_1 with state S_3 are also fulfilled at the oxygen atoms of the acac2 ligand, which contribute

to the HOMO and HOMO−1 with atomic orbitals of different angular momentum orientations (Figure 5.6). Taking into account a relatively large SOC constant of oxygen of ζ_ℓ = 154 cm^{-1} (compare to that of carbon [ζ_ℓ = 32 cm^{-1}] and nitrogen [ζ_ℓ = 78 cm^{-1}])[33], the acac2 induced SOC may have a notable contribution to relaxation of the $\Delta S = 0$ selection rule for $T_1 \rightarrow S_0$ phosphorescence and thus enhance its rate. In the range 0.5 – 1 eV above state T_1 singlet states S_4−S_8 and S_{10} are contributed by transitions HOMO−n→LUMO with $n \geq 2$ strongly involving Pt atom (Figure 5.6, Tables 8.19 and 8.20). Since state T_1 is of HOMO→LUMO origin and HOMO is mildly contributed by the Pt atom (Figure 5.6, Table 8.19), these higher laying singlets can spin-orbit couple with state T_1 also at the Pt(II) center, which would further enhance the rate of $T_1 \rightarrow S_0$ phosphorescence.

Thus, the analysis of the TD-DFT data predicts that in **IrPt'** SOC of state T_1 with singlets is primarily induced at the Ir center and is further intensified at the Pt center and the acac1 ligand and allows to expect a relatively high oscillator strength for the T_1−S_0 radiative transition. This agrees very well with the unusually high phosphorescence rate measured for **IrPt**, which corresponds to a radiative decay time in the sub-microsecond range.

5.4 Concluding remarks. Utilization of the π-deficient 4,6-bis(4-(tret-butyl)phenyl)pyrimidine derivative (dpp) as a chromophoric ligand bridging Ir(III) and Pt(II) metal center afforded complex **IrPt** – a material with unusually fast and highly efficient red phosphorescence. The coordination of the Pt as an additional metal center worked in two ways: (i) introduced an additional SOC center that allowed to enhance the phosphorescence rate; (ii) caused a notable red-shift of emission by expanding the chromophoric system of the ligand to the metal center and the ancillary acac1 ligand. This afforded a chromophoric system that is broad enough for red-phosphorescence yet does not sacrifice the MLCT character of the T_1 state, important for efficient SOC with the singlets (Compare to ref.[71]). This shows a valuable design approach to counteract the typical decrease of the phosphorescence rate due to a smaller Einstein's coefficient at a relatively lower energy of the emitting state. Another important notion is that the acac ligand, commonly regarded as ancillary, is seemingly not innocent and contributes to the SOC of state T_1 with the singlets thus further enhancing the rate of phosphorescence.

6. Summary

Throughout this work, it is demonstrated that the dinuclear molecular design of Ir(III) complexes can be highly beneficial to enhance the phosphorescence rate and yet to red-shift its spectral range, compared to the mononuclear analogues. The increased rate of phosphorescence in the dinuclear complex, despite relatively lower energy of the emitting state giving a smaller Einstein's coefficient of spontaneous emission, indicates strong modulation of the electronic factor with an increase of the oscillator strength of phosphorescence. It is discussed that mechanistically such an increase of the oscillator strength in dinuclear structure, compared to mononuclear, is due to the doubled number of excited singlet states that are electronically suited for SOC with the state T_1, which, in turn, results from the electronic coupling of the two coordination sites. Despite that SOC is a short-range phenomenon, splitting the SOC-inducing metal contribution between the two centers does not affect the SOC efficiency of state T_1 with an electronically suited singlet state, as compared to that in a mononuclear structure. This is the benefit of (*quasi*)-symmetric design of the studied dinuclear complexes, which gives about the equal contribution of the two metal centers to the MOs that participate in electronic transitions forming the state T_1 and excited singlet states suited for SOC with T_1. Therefore, the symmetricity of the multinuclear structure seems to be important for efficient cooperation of the metal centers in SOC of state T_1 with singlets.

The strength of SOC of the phosphorescent state T_1 with singlet states can be effectively modulated via the chromophoric and ancillary ligands. For instance, the coordination of a halide to the metal atom introduces an additional SOC center that enhances the SOC and thus also the phosphorescence rate. In fact, as discussed in the case of **Ir$_2$I$_2$**, when several highest occupied MOs of the complex are predominantly localized on the halides, the role of the halides in SOC is even higher than that of the Ir(III) centers.

Increasing the π-excessiveness of the chromophoric bridging ligand, which increases the energies of the frontier orbitals, decreases the contribution of SOC-inducing centers to the formation of the lowest excited states and thus diminishes the rate of the formally spin-forbidden processes, such as intersystem crossing and phosphorescence. In the case of **IrIr** the slow intersystem crossing even results in the occurrence of an unusual for Ir(III) complexes fluorescence in steady-state spectra that accompanies the phosphorescence. The π-deficient character of the chromophoric bridging ligand, on the other hand, is found as beneficial to design materials with fast phosphorescence as it results in a relatively strong contribution of the SOC-inducing atoms to the formation of the lowest excited states. The π-deficient bis-tridentate ligand in dinuclear **Ir-2** afforded an efficient red emission with a remarkable rate of phosphorescence. In fact, the strong π-deficiency of the ligand, due to one 1,3-pyrimidine and two pyridine rings, in **Ir-2** effectively counteracted the effect of its relatively expanded π-conjugation system, which, along

with decreasing the HOMO−LUMO energy gap, also plays for an increase of the energy and ligand localization of the HOMO thus reducing the SOC-inducing MLCT character of state T_1. These findings demonstrate that varying the π-excessiveness/deficiency and expansion of the π-conjugated system of the chromophoric ligand can afford smooth tuning of the photoluminescence between phosphorescence with high radiative rate and dual emission with a relatively slow phosphorescence.

An efficient way found in this work to reach efficient red phosphorescence is to utilize a π-deficient ligand with a relatively small chromophoric (π-conjugated) system to bridge Pt(II) and Ir(III) centers. The π-deficiency and relatively small π-system of the ligand in such cases can afford strong involvement of the Ir(III) center(s) to the formation of the lowest excited states preserving efficient SOC of state T_1 with singlet states. Meanwhile, the square-planar coordination geometry of Pt(II) expands the chromophoric system to Pt(II) and the ancillary ligand, decreasing the T_1 state's energy and reaching red optical range, and yet Pt(II) plays as an additional center for SOC of T_1 with the singlets. As a result of this design strategy, complex **IrPt**, utilizing the same chromophoric bridging ligand (dpp) as the green to yellow phosphorescent complexes **IrCl**, **Ir_2Cl_2** and **Ir_2I_2**, affords red phosphorescence with an unprecedented combination of high emission rate and high quantum yield.

7. Experimental

7.1 Analytic characterization. All solvents and reagents were purchased from commercial suppliers and used without further purification unless otherwise noted. NMR spectra were recorded on a JEOL ECS400FT Delta spectrometer (399.78 MHz for ^{1}H NMR, 100.53 MHz for ^{13}C NMR and 376.17 MHz for ^{19}F NMR) at Northumbria University (United Kingdom). Chemical shifts are reported in parts per million (ppm) relative to tetramethylsilane as an internal standard. Coupling constants (J) are measured in hertz. Elemental analyses were carried out on ELEMENTAR vario MICRO CUBE instrument at the central analytical services of the University of Regensburg. Field-desorption mass-spectroscopy analyses were performed on a JEOL AccuTOF-GCX instrument at the central analytical services of the University of Regensburg. High-resolution mass spectrometry (HRMS) analysis of complex **IrPt** was performed on a LTQ Orbitrap XL spectrometer at the EPSRC National Mass-Spectrometry Service (University of Swansea).

The investigated complexes were synthesized at the research group of Dr. Valery Kozhevnikov at Northumbria University (United Kingdom).

Complex **IrCl**

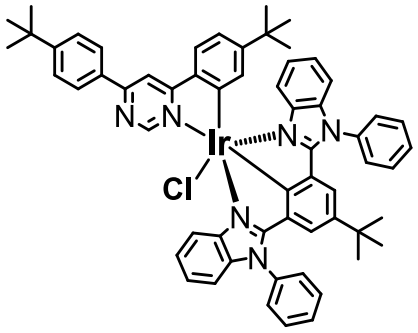

The compound is synthesized at the research group of Dr. Valery Kozhevnikov at Northumbria University (United Kingdom). For synthetic details and procedure see ref.[19]

^{1}H NMR (400 MHz, $CDCl_3$): δ 11.17 (br.s, 1H), 8.44 (d, *J* = 8.2 Hz, 2H), 8.34 (s, 1H), 7.67 (d, *J* = 8.2 Hz, 2H), 7.62-7.67 (m, 8H), 7.67 (d, *J* = 8.2 Hz, 1H) 7.37 (m, 2H),7.08 (m, 2H), 6.98 (m, 4H), 6.75 (s, 2H), 6.70 (br.d, *J* = 8.2 Hz, 1H), 6.64 (br.d, *J* = 8.2 Hz, 2H), 5.76 (br.s, 1H), 1.45 (s, 9H), 0.92 (s, 9H), 0.88 (s, 9H). Field-desorption mass-spectrometry (FD-MS). For [M^+] ($C_{60}H_{56}N_6ClIr$) calculated 1088.3884, found 1088.3563. Elemental (C, H, N) analysis. Calculated for $C_{60}H_{56}N_6ClIr$, %: C, 66.19; H, 5.18; N, 7.72. Found: C, 66.07; H, 5.28; N, 7.55

Complex **Ir_2Cl_2**

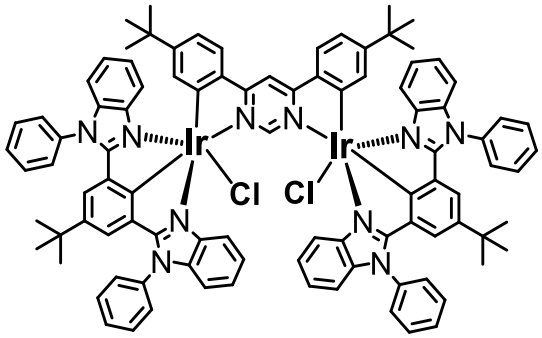

The compound is synthesized at the research group of Dr. Valery Kozhevnikov at Northumbria University (United Kingdom). For synthetic details and procedure see ref.[19]

^{1}H NMR (400 MHz, $CDCl_3$): δ 12.90 (s, 1H), 8.51 (s, 1H), 7.75-7.68 (m, 18H), 7.46-7.44 (m, 4H), 7.39 (d, 4H, *J* = 8.2), 7.0826-7.02 (m, 8H), 6.83-6.77 (m, 10H), 5.91 (br. s, 2H), 0.98 (s, 18H), 0.96 (s, 18H). Field-desorption mass-spectrometry (FD-MS). For [M^+] ($C_{96}H_{84}N_{10}Ir_2Cl_2$) calculated 1832.5516, found 1832.4818. Elemental (C, H, N) analysis. Calculated for $C_{96}H_{84}Cl_2Ir_2N_{10}$, %: C, 62.90; H, 4.62; N, 7.64. Found: C, 62.69; H, 4.93; N, 7.32

Complex **Ir_2I_2**

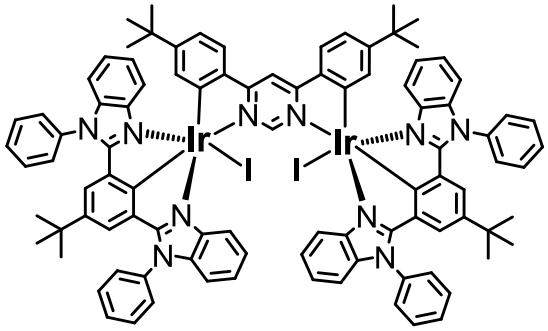

The compound is synthesized at the research group of Dr. Valery Kozhevnikov at Northumbria University (United Kingdom). For synthetic details and procedure see ref.[19]

^{1}H NMR (400 MHz, $CDCl_3$) δ 0.97 (18H, s), 0.98 (18H, s), 5.81 (2H, d, *J* = 2.0 Hz), 6.81 – 6.87 (10H, m), 7.03 – 7.08 (8H, m), 7.43 – 7.49 (8H, m), 7.66 – 7.72 (18H, m), 8.43 (1H, s), 13.87 (1H, s). ^{13}C NMR (101 MHz, $CDCl_3$) δ 31.0 (CH_3), 31.4 (CH_3), 34.6 (quat.), 104.7 (CH), 110.5 (CH), 116.6 (CH), 118.6 (CH), 122.4 (CH), 123.1 (CH), 124.9 (CH), 125.6 (CH), 127.9 (CH), 129.0 (CH), 130.0 (CH), 130.1 (CH), 130.5 (CH), 131.4 (CH), 135.4 (quat.), 135.8 (quat.), 139.9 (quat.), 141.6 (quat.), 142.9 (quat.), 154.3 (quat.), 154.8 (quat.), 161.4 (quat.), 171.4 (quat.), 172.2 (quat.), 178.5 (quat.) Field-desorption mass-spectrometry (FD-MS). For [M^+] ($C_{96}H_{84}N_{10}Ir_2I_2$) calculated 2016.4240, found 2016.3726. Elemental (C, H, N) analysis. Calculated for $C_{96}H_{84}N_{10}Ir_2I_2$ %: C, 57.19; H, 4.20; N, 6.95. Found: C, 56.46; H, 4.27; N, 6.72.

Complex **IrIr**

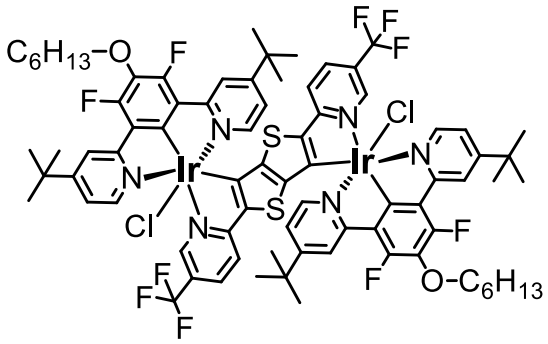

The compound is synthesized at the research group of Dr. Valery Kozhevnikov at Northumbria University (United Kingdom). For synthetic details and procedure see ref.[69]

^{1}H NMR (400 MHz, CD_2Cl_2) δ 10.00 (2 H, s), 8.04 (4 H, s), 7.97 (2 H, dd, *J* = 8.6 and 2.1), 7.46 (2 H, d, *J* = 8.4), 7.32 (4 H, d, *J* = 6.1), 6.88 (4 H, dd, *J* = 6.1 and 2.1), 4.30 (4 H, t, *J* = 6.8), 1.95 – 2.02 (4 H, m), 1.62 - 1.70 (4 H, m), 1.41 - 1.51 (8 H, m), 1.23 (36 H, s), 0.99 (6 H, t, *J* = 6.8).

^{13}C NMR (101 MHz, CD_2Cl_2) δ 14.3, 23.1, 26.0, 30.5, 30.6, 32.1, 35.3, 76.4, 117.9, 120.4, 120.5, 120.6, 121.0, 122.7, 123.0, 125.4, 125.8, 131.5, 135.5, 140.1, 142.6, 146.7, 149.3, 151.3, 154.1, 156.4, 156.8, 162.7, 164.1, 165.8, 167.9. ^{19}F NMR (376 MHz, CD_2Cl_2) δ -126.27, -61.87

Field-desorption mass-spectrometry (FD-MS). For [M^+] ($C_{78}H_{80}Cl_2F_{10}Ir_2N_6O_2S_2$) calculated 1842.4240, found 1842.3983. Elemental (C, H, N) analysis. Calculated for $C_{78}H_{80}Cl_2F_{10}Ir_2N_6O_2S_2$, %: C, 50.83; H, 4.38; N, 4.56. Found: C, 50.92; H, 4.53; N, 4.40

Complex **Ir-1**

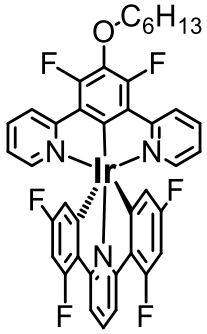

The compound is synthesized at the research group of Dr. Valery Kozhevnikov at Northumbria University (United Kingdom). For synthetic details and procedure see ref.[91]

^{1}H NMR (400 MHz, $CDCl_3$); δ 8.15 (d, J = 8.4 Hz, 4H), 7.85 (t, J = 7.6 Hz, 1H), 7.50-7.55 (m, 4H), 6.69 (t, J = 7.2 Hz, 2H), 6.22 (t, J = 12.0 Hz, 2H), 5.68 (d, 6.8 = Hz, 2H), 4.28 (t, J = 6.8 Hz, 2H), 1.90-1.98 (m, 2H), 1.58-1.66 (m, 2H), 1.39-1.47 (m, 4H), 0.94-0.98 (m, 3H). Field-desorption mass-spectrometry (FD-MS). For [M^+] ($C_{39}H_{28}F_6IrN_3O$) calculated 861.1766, found 861.0960. Elemental (C, H, N) analysis. Calculated for $C_{39}H_{28}F_6IrN_3O$, %: C, 54.41; H, 3.28; N, 4.88. Found: C, 54.57; H, 2.97; N, 4.77l

Complex **Ir-2**

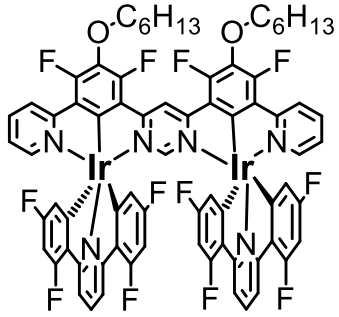

The compound is synthesized at the research group of Dr. Valery Kozhevnikov at Northumbria University (United Kingdom). For synthetic details and procedure see ref.[91]

^{1}H NMR (400MHz, $CDCl_3$) δ 8.75 (s, 1H), 8.10 (d, 2H, *J* = 7.79Hz), 8.02 (d, 4H, J= 8.24Hz), 7.83 (t, 2H, J= 8Hz), 7.52 (t, 2H, J= 7.79Hz), 7.35 (d, 2H, J= 5.50Hz), 7.08 (s, 1H), 6.68 (t, 2H, J= 7Hz), 6.17 (t, 4H, J= 9.52, 4.62Hz), 5.43 (dd, 4H, J= 6.89, 2.29Hz), 4.27 (t, 4H, J= 6.65Hz), 2.02 (quin, 4H, J= 6.87Hz), 1.70 (br.quin, 4H, J= 7.33Hz), 1.50 (m, 8H), 1.05 (t, 6H, J= 6.87Hz). Field-desorption mass-spectrometry (FDMS). For [M^+] ($C_{72}H_{50}F_{12}Ir_2N_6O_2$) calculated 1642.3039, found 1642.3358. Elemental (C, H, N) analysis. Calculated for $C_{72}H_{50}F_{12}Ir_2N_6O_2$, %: C, 52.61; H, 3.07; N, 5.02. Found: C, 52.34; H, 3.01; N, 5.02

Complex **IrPt**

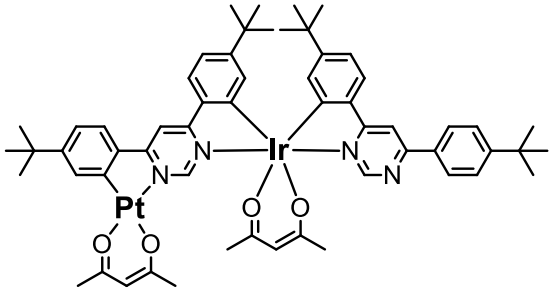

The compound is synthesized at the research group of Dr. Valery Kozhevnikov at Northumbria University (United Kingdom). For synthetic details and procedure see ref.[61]

NMR (400MHz, $CDCl_3$) δ 9.47 (s, 1H), 9.11 (s, 1H), 8.18 (d, *J* = 8.4 Hz, 2H), 8.09 (s, 1H), 7.83 (s, 1H), 7.75 (s, 1H), 7.60-7.66 (m, 5H), 7.26 (1H), 6.94 (d, *J* = 8.4 Hz, 2H), 6.56 (s, 1H), 6.42 (s, 1H), 2.03 (s, 3H), 1.91 (s, 3H), 1.86 (s, 3H), 1.84 (s, 3H), 1.42 (s, 18H), 1.08 (s, 9H), 1.05 (s, 9H).

High resolution mass-spectrometry (HRMS). For [MH^+] ($C_{58}H_{67}N_4O_4{}^{193}Ir^{195}PtH$) calculated 1272.4520, found 1272.4561. Elemental (C, H, N) analysis. Calculated for $C_{72}H_{50}F_{12}Ir_2N_6O_2$, %: C, 54.79; H, 5.31; N, 4.41. Found: C, 54.84; H, 5.37; N, 4.37.

7.2 Steady-state optical spectroscopy. The measurements were performed using commercially available solvents of the spectroscopical grade of purity. The UV-Vis absorption spectra were measured with a Varian Cary 300 double-beam spectrometer. The photoluminescence

(PL) spectra were measured with a Horiba Jobin Yvon Fluorolog-3 steady-state fluorescence spectrometer, modified to allow for time-dependent measurements. The low-temperature photoluminescent properties were investigated with the sample deposited in a helium cryostat (Cryovac Konti Cryostat IT) in which the helium gas flow, gas pressure, and heating were controlled. Thus, the temperature could be varied between 1.7 and 120 K. The photoluminescence decay times were measured with a PicoBright PB-375 pulsed diode laser (λ_{exc} = 378 nm, pulse width 100 ps) used as the excitation source. The photoluminescence signal was detected with a cooled photomultiplier attached to a FAST ComTec multichannel scalar PCI card with a time resolution of 250 ps. The photoluminescence quantum yields were determined with a Hamamatsu C9920-02 system equipped with a Spectralon® integrating sphere.

7.3 Transient absorption measurements and data analysis.

This part of the work was carried out in collaboration with Fabian Brandl and Dr. Roger-Jan Kutta at Universität Regensburg, Institut für Physikalische und Theoretische Chemie

Sub-picoseconds Pump/Supercontinuum-Probe Spectroscopy. The measurements were performed using a solution in commercially available dichloromethane of spectroscopical purity grade. The femtosecond transient absorption apparatus is based on the design published earlier[105]. A Ti:Sapphire oscillator-regenerative amplifier laser system (Coherent Libra) generates 100 fs pulses with 1.0 mJ energy at 1 kHz repetition rate. With 0.67 mJ of these pulses a collinear parametric amplifier (TOPAS-C, Light Conversion) was pumped. The output of the TOPAS was compressed with a pair of quartz prisms and used to excite the sample at the $S_1 \leftarrow S_0$ absorption band. The pulse energy was set to ca. 300 nJ focused to ca. 100 µm. The remaining 0.33 mJ of the Ti:Sa output drive a two-stage NOPA[106] which produces ca. 20 µJ pulses at 510 nm. These were compressed with a quartz prism pair and focused onto a 1 mm thick CaF_2 plate to generate a white-light supercontinuum for the probe beam. The plate was mounted on an XY stage and moved continuously. The white light supercontinuum was spectrally filtered and split into a reference and signal beam path. At the sample position the spot size of the probe pulse was ca. 60 µm. The signal and reference beams were imaged onto entrance slits of two home-build grating spectrographs and recorded with photodiode arrays (Hamamatsu, S3901-512Q, 512 pixels) at 1.5 nm resolution. The time delay between probe and pump is controlled via variation of the probe beam path using a delay stage (Physik Instrumente M-531.2S) equipped with an open corner cube reflector.

The sample solution was pumped continuously through a self-made quartz cell. Each scan was performed from −0.36 ps to 1.0 ps in 6 fs steps, and from 1 ps to 1.8 ns in 240 steps with logarithmic temporal spacing. At each delay position of a scan, an average over typically 100 transient absorption spectra were taken, each calculated for a baseline-corrected single shot. Averaging of

at least eight independent scans result in the final spectra for either parallel $\Delta A_{\parallel}$ and perpendicular $\Delta A_{\perp}$ polarization with respect to the angles between pump and probe pulse polarization, which was set via an l/2λ plate in the pump beam path. The averaged pre-t_0 laser scatter signal was subtracted from the data and the ca. 1.5 ps chirp of the white light was corrected prior to data analysis using the coherent artefact as an indicator for time zero at each wavelength. Spectra under magic-angle polarization were calculated via Eq. 7.1. No smoothing or filtering procedures were applied to the data. The raw data are shown in Figure 7.1.

$$\Delta A_{M} = \frac{(2\Delta A_{\perp} + \Delta A_{\parallel})}{3} \tag{7.1}$$

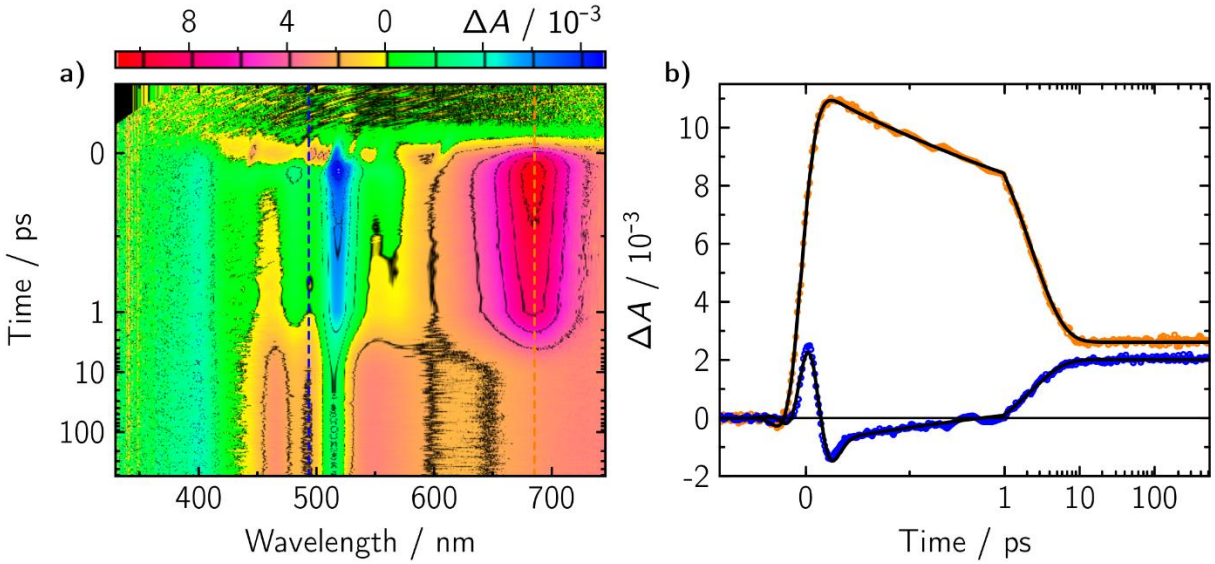

Figure 7.1. Transient absorption spectra in false color representation of **IrIr** (a) in dcm when exciting into the corresponding $S_1 \leftarrow S_0$ transition. b shows two selected time traces each along a certain probe wavelength as indicated by a dashed line in (a). The black solid lines in (b) show the corresponding global fit to the data.

Transient absorption data analysis and modelling. Global fitting was performed using an in-house written program described previously.[81,82] Transient absorption data consist of a series of difference spectra recorded at a number of delay times, ΔA(t,λ), which may be represented as a rectangular matrix ΔA of dimension $N_T \times N_L$. In this matrix each column is a time trace for a fixed wavelength of N_T points, and each row is a spectrum at a given delay time of N_L points. This matrix can be decomposed into a sum of products of one-dimensional functions by a global fit. Here, the assumption is made that the data can be modelled by a linear combination of products between spectra, $S_k(\lambda)$, and concentration-time profiles, $c_k(t)$, according to Eq. 7.2.

$$\Delta A_{ij} = \sum_{k=1}^{N} c_k(t_i) S_k(\lambda_j) = \sum_{k=1}^{N} c_{ik} S_{jk} \tag{7.2}$$

In Eq. 7.2 ΔA_{ij} can be approximated by matrix D, in which the time profiles are represented as a linear combination of known analytic functions, $f_k(t)$:

$$D_{ij} = \sum_{k=1}^{N_C} c_k(t_i) S_k(\lambda_j) \tag{7.3}$$

$$c_k(t) = \sum_{k=1}^{N_F} f_l(t) X_{lk} \tag{7.4}$$

where N_C is the number of distinct spectral species and N_F is the number of analytic time functions. The model data matrix D can be written as

$$D = CS = FXS = FB \tag{7.5}$$

where C is defined as a $N_T \times N_C$ matrix with elements, $C_{ik} = c_k(t_i)$, and F is defined as a $N_T \times N_C$ matrix with elements, $F_{il} = f_l(t_i)$. Thus, the *k*-th row of the matrix B, with elements $B_{kj} = b_k(\lambda_j)$, corresponds to the spectral changes associated with the time function, $f_k(t)$. When using exponential decays (convoluted with the instrument response) as analytical function the corresponding spectra are called decay associated difference spectra (DADS). The linear least squares problem

$$\chi^2 = \|\Delta A - FB\|^2 = \text{Min} \tag{7.6}$$

for given matrices ΔA and F can be solved by efficient existing algorithms. A nonlinear least squares algorithm is used for further optimization of χ^2 by optimizing the rate constants in F, so that the DADS and the corresponding rate constants are the unique result of the global fit not requiring any model for the kinetics involved in the transient processes. The details of a model will be entirely defined in the matrix X that relates the actual species kinetics to the elementary function, $f_k(t)$. The appropriate matrix, X, can be chosen depending on the model and the species associated spectra (SAS) in matrix S are calculated according to Eq. 7.7.

$$S = X^{-1}B \tag{7.7}$$

The χ^2 value found in the global fit does not change by this step and, thus, this procedure has the advantage that all interpretation is performed with the same quality of fit.

General kinetic model. The analytic fitting function shown in Eq. 7.8 was used in the global lifetime analysis in order to determine the dynamics of each complex

$$f_k(t) = \sum_{i=0}^{2} \frac{d^i}{dt^i} g_{art}(t - t_0) + \left(\delta(t) + \sum_{j=1}^{N} \exp(-\kappa_k t) \right) \otimes g_{app}(t - t_0) \tag{7.8}$$

where $\otimes\, g_{app}(t - t_0)$ indicates convolution with the apparatus function approximated by a Gaussian, $\delta(t)$ is the Dirac delta function, $\sum_{i=0}^{2} \frac{d^i}{dt^i} g_{art}(t - t_0)$ are a Gaussian and its first and second derivatives with identical temporal widths as the apparatus function allowing to account for the coherent artefact, and N is the number of exponentials describing the dynamics of the TA change over time. The general photophysical processes can be described with the differential equations of Eq. 7.9.

$$\frac{d}{dt}\begin{pmatrix}[S_1]\\ [T_1]\end{pmatrix} = -\begin{pmatrix} k_{ic} + k_r + k_{isc} & 0 \\ -k_{isc} & k_{bisc}\end{pmatrix}\begin{pmatrix}[S_1]\\ [T_1]\end{pmatrix} \tag{7.9}$$

The eigenvalues of the rate constant matrix are given in Eq. 7.10 to 7.11 and are absolutely determined by the global fit described above.

$$\kappa_1 = k_{ic} + k_r + k_{isc} \tag{7.10}$$

$$\kappa_2 = k_{bisc} \tag{7.11}$$

In this simple model one obtains the following relationship between the species associated spectra, SAS_i, and the DADS, D_i, c_0 is the contribution of the ground state spectrum, SAS_{S_0}, and Φ_{T_1} is the triplet state quantum yield:

$$SAS_{S_1} = \frac{(D_1 + D_2)}{c_0} + SAS_{S_0} \tag{7.12}$$

$$SAS_{T_1} = \frac{(\kappa_1 - \kappa_2)D_2}{c_0 \Phi_{T_1} \kappa_1} + SAS_{S_0} \tag{7.13}$$

Here, c_0 and Φ_{T_1} are the only undetermined parameters. However, one can at least find upper or lower bounds by the requirement that the resulting SAS must be positive, and should not show any of the characteristic bands of the other species. In particular the negative peaks from the ground state bleach should disappear in the SAS. The determination of the individual parameters for each individual case is shown in Figure 7.2

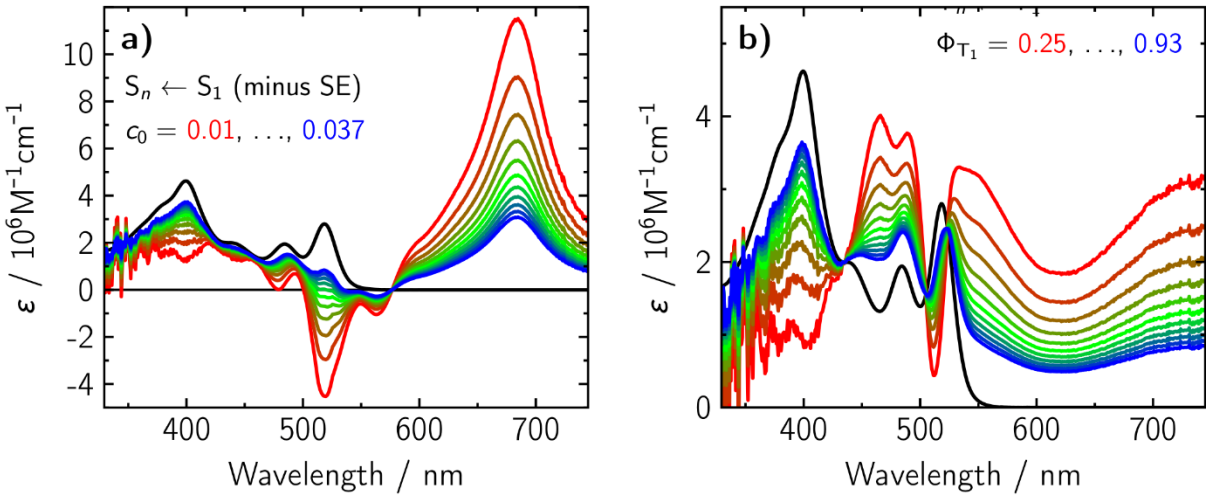

Figure 7.2. SAS of complex **IrIr** in dichloromethane in the S_1 state, Sn←S_1 transitions (minus stimulated emission (SE)), (a), and in the T_1 state, Tn←T1 transitions, (b). The contribution of the ground state spectrum, c_0, was varied between 0.01 (red) and 0.037 (blue). Below $c_0 = 0.025$ the S_1 spectrum becomes negative and above contributions of the S_0 spectrum arise. The triplet yield, Φ_{T_1}, was varied between 0.25 (red) and 0.93 (blue). The lower bound for Φ_{T_1} is 0.2 since below this value the T_1 spectrum becomes negative. Since no significant signatures of the S_0 spectrum start to arise even at full scaling, the preferred value of Φ_{T_1} is close to unity. The S_0 spectrum is also plotted in both panels for comparison.

7.4 Computations.

Throughout the work, electronic structure computations were carried out with the Gaussian 09 package[107] utilizing the DFT approach with the "tight" criteria for geometry optimizations. All the complexes, except **IrPt**, were computed using the M11L[108] functional[109,110] for both, geometry optimizations (DFT) as well as the time-dependent (TD-DFT) calculations. In the case of **IrPt** the geometry optimizations were conducted with M06[111] functional while the TD-DFT calculations were conducted with M06L[112] functional. All the calculations utilized the def2-SVP[113,114] basis set with effective core potentials (ECP) for the Ir(III) and Pt(II) ions, and the C-PCM solvation model[115] with the parameters of the solvent used for the photophysical measurements (toluene or dichloromethane).

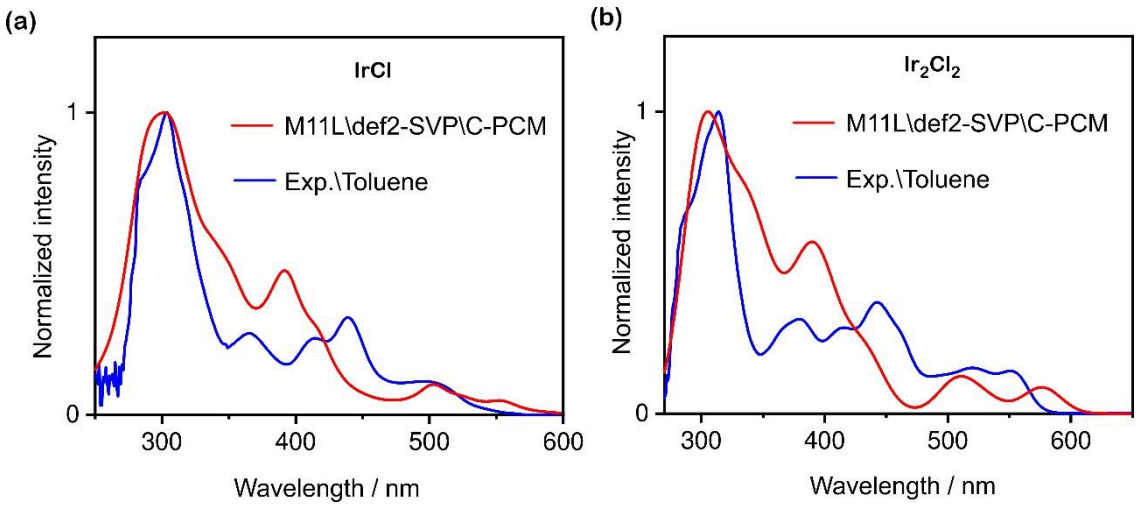

Figure 7.3. The experimental (blue) and TD-DFT calculated (red), in optimized ground state geometry, absorption spectra of complex **IrCl** (a) and complex **Ir_2Cl_2** (b). (cf. ref.[19])

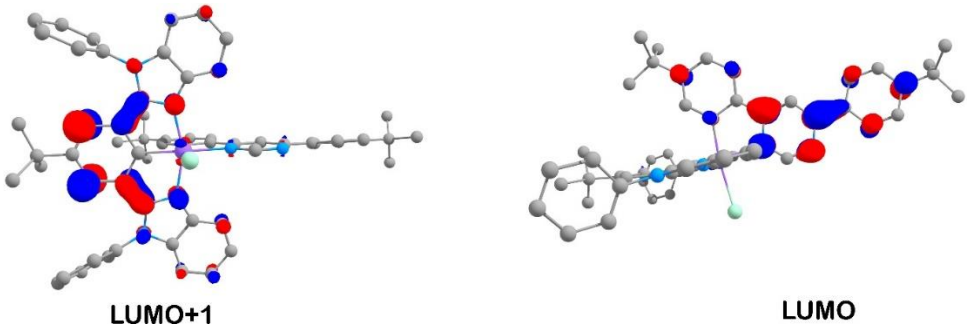

Figure 7.4. DFT calculated Iso-surface contour plots (iso-value=0.05) of the lower unoccupied orbitals of complex **IrCl** calculated at relaxed ground state (S_0) geometry. (cf. ref.[19])

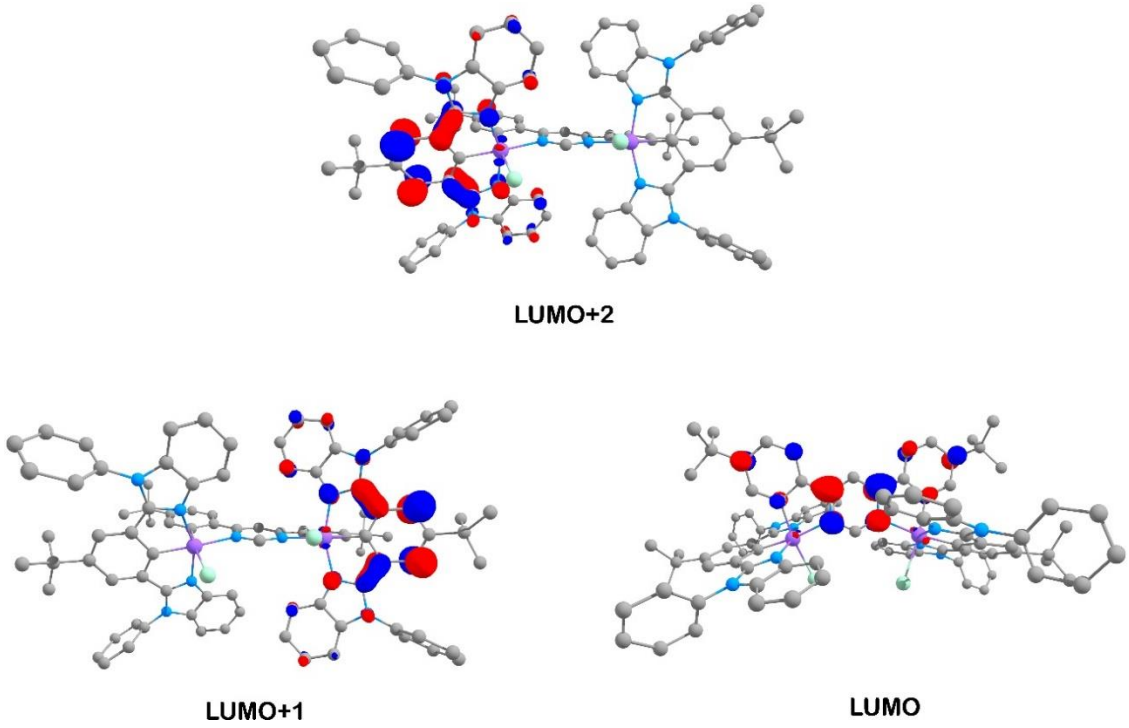

Figure 7.5. DFT calculated Iso-surface contour plots (iso-value = 0.05) of the lower unoccupied orbitals of complex **Ir_2Cl_2** calculated at relaxed ground state (S_0) geometry. (cf. ref.[19])

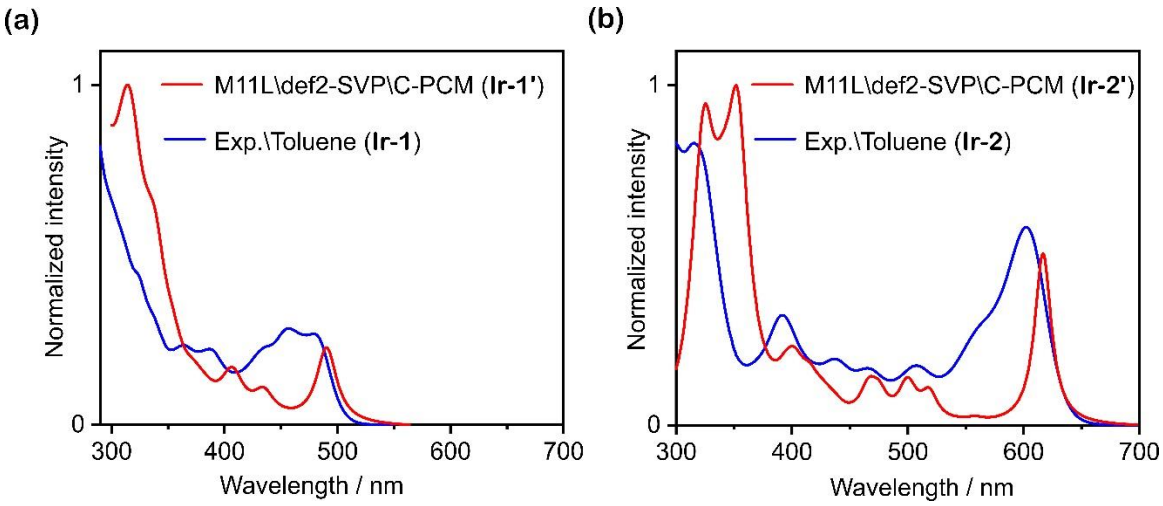

Figure 7.6. The TD-DFT calculated absorption spectra (red traces) of **Ir-1'** (a) and **Ir-2'** (b) respectively compared with the experimental absorption spectra (blue traces) obtained for **Ir-1** and **Ir-2** in toluene. (cf. ref.[91])

7.5 Confocal microscopy imaging.

This part of the work was carried out in collaboration with the research group of Prof. Dr. Konrad Kowalski at the University of Łódź.

For confocal microscopy analysis, the HeLa cells (ATTC1 Catalog No. CCL-2TM, human epithelial cells) were cultivated in RPMI 1640 medium without phenol red, supplemented with 10% fetal bovine serum (FBS) at 37 °C in a humidified atmosphere with 5% CO_2. Twenty-four

hours before the experiment, HeLa cells at density 1 x 10^5 /mL were plated in 4 chamber culture slide with glass bottom and cultured at the same conditions. After incubation overnight, the cells were treated with 500 μM of **IrIr** for 3 hours, were fixed with 4% formaldehyde for 30 min, and rinsed three times with phosphate-buffered saline (PBS). Confocal imaging was performed using DMI 6000 CS inverted microscope with TCS SP8 confocal system operated by LAS 2.0.215022 software (Leica Microsystem, Wetzlar, Germany). The observations were made using HC PLAPO CS2 63x/1.40 oil immersion objective. The parameters of the excitation and the emission were unified for the control material and that stained with tested compound. The UV diode laser (405 nm, 5 mW nominal power with 10% intensity) was used and the emission was collected at the range of 680-790 nm by the hybrid detector (HyD) in bright R mode (gain 153%, offset 0%). Additionally, transmitted light was also collected by the conventional detector -photomultiplier tube (PMT). Confocal scans were performed bidirectionally at 400Hz speed and line average set at 5. The fluorescence was registered from the single confocal section (pinhole 1.0 Airy unit). To check intercellular localisation of **IrIr** the cells were stained with 4′,6-diamidino-2-phenylindole (DAPI) for DNA and then with and 3′-dihexyloxacarbocyanine iodide ($DiOC_6$) to stain endoplasmic reticulum, vesicle membranes and mitochondria. Both dyes were used at the concentration of 0.5 □g/mL for 5 min. and three steps of PBS rinsing were performed. The settings of confocal system for AVZ were set up as described above and the sequences for DAPI (excitation 5% 405 nm of UV diode laser, detection - PMT 420-485 nm) and $DiOC_6$ (excitation - 488 nm 1% white laser (WLL), detection - PMT 499-570 nm) were added.

7.6 X-Ray crystallography. All the single crystal x-ray diffraction (XRD) experiments were carried out at the central analytical services of the University of Regensburg. The XRD obtained structures were all deposited at the Cambridge Crystallographic Data Center (CCDC).

Experimental for complex **IrCl**. Single clear orange prism-shaped crystals were obtained by slow convectional diffusion of methanol into the solution of **IrCl** in dichloromethane. A suitable crystal (0.18×0.09×0.03) mm^3 was selected and mounted on a Lindemann tube oil on a GV1000, TitanS2 diffractometer. The crystal was kept at T = 123.00(19) K during data collection. Using Olex2[108], the structure was solved with the ShelXT[116] structure solution program, using the Intrinsic Phasing solution method. The model was refined with version 2016/6 of ShelXL[116] using least squares minimization.

Experimental for complex **Ir_2Cl_2**. Single orange plate-shaped crystals were obtained by slow convectional diffusion of methanol into the solution of **Ir_2Cl_2** in dichloromethane. A suitable crystal (0.18×0.13×0.07) was selected and mounted on a MITIGEN holder oil on a SuperNova, Single source at offset, Atlas diffractometer. The crystal was kept at T = 123.00(10) K during data

collection. Using Olex2[108], the structure was solved with the SIR2004[117] structure solution program, using the Direct Methods solution method. The model was refined with ShelXL[116] using least squares minimization and SQUEEZE method[118] to address the solvent disorder issue.

Experimental for complex **IrIr** A suitable clear orange needle crystal with dimensions 0.18 × 0.07 × 0.04 mm^3 was selected and mounted on a MITIGEN holder with inert oil on a SuperNova, Single source at offset/far, Atlas diffractometer. The crystal was kept at T = 123.01(10) K during data collection. The structure was solved with the ShelXT 2018/2[119] solution program using dual methods and by using Olex2[108] as the graphical interface. The model was refined with ShelXL 2018/3[116] using least squares minimization.

Experimental for complex **Ir-1**. Single clear light-yellow plate crystals were obtained by slow convectional diffusion of methanol into the solution of **Ir-1** in dichloromethane. A suitable crystal (0.18 × 0.07 × 0.06) mm^3 was selected and mounted on a MITIGEN holder oil on a SuperNova, single source at offset, Atlas diffractometer. The crystal was kept at T = 123.01(10) K during data collection. Using Olex2[108], the structure was solved with the ShelXT 2018/2 solution program[116] using dual methods. The model was refined with ShelXL 2018/3[116] using least squares minimization.

Experimental for complex **Ir-2**. Single clear brown prism crystals were obtained by slow convectional diffusion of methanol into solution of **Ir-2** in dichloromethane. A suitable crystal (0.19 × 0.06 × 0.05 mm^3) mm^3 was selected and mounted on a MITIGEN holder oil on a GV1000, TitanS2 diffractometer. The crystal was kept at T = 89.4(9) K during data collection. Using Olex2[108], the structure was solved with the ShelXT solution program[116] using dual methods. The model was refined with ShelXL 2018/3[116] using least squares minimisation**.**

Experimental for complex **IrPt**. Red needle-shaped single crystals of complex **IrPt** were obtained by slow convectional diffusion of methanol into a solution of **IrPt** in dichloromethane. A representative 0.34×0.09×0.05 mm^3 crystal was selected and mounted with mineral oil on a MITIGEN holder on a SuperNova diffractometer equipped with an Atlas CCD detector. The crystal was kept at T = 123.01(10) K during data collection. The structure was solved with the ShelXT[116] structure solution program using the Intrinsic Phasing solution method and by using Olex2[108] as the graphical interface. The model was refined with version 2018/3 of ShelXL[116] using least squares minimization.

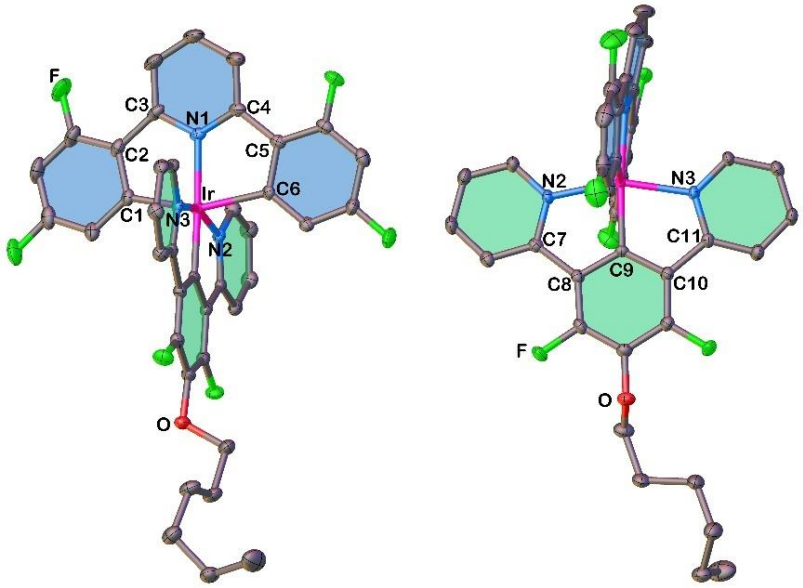

Figure 7.7. The XRD obtained molecular structure of complex **Ir-1** shown from different perspectives with atom numbering. (cf. ref.[91])

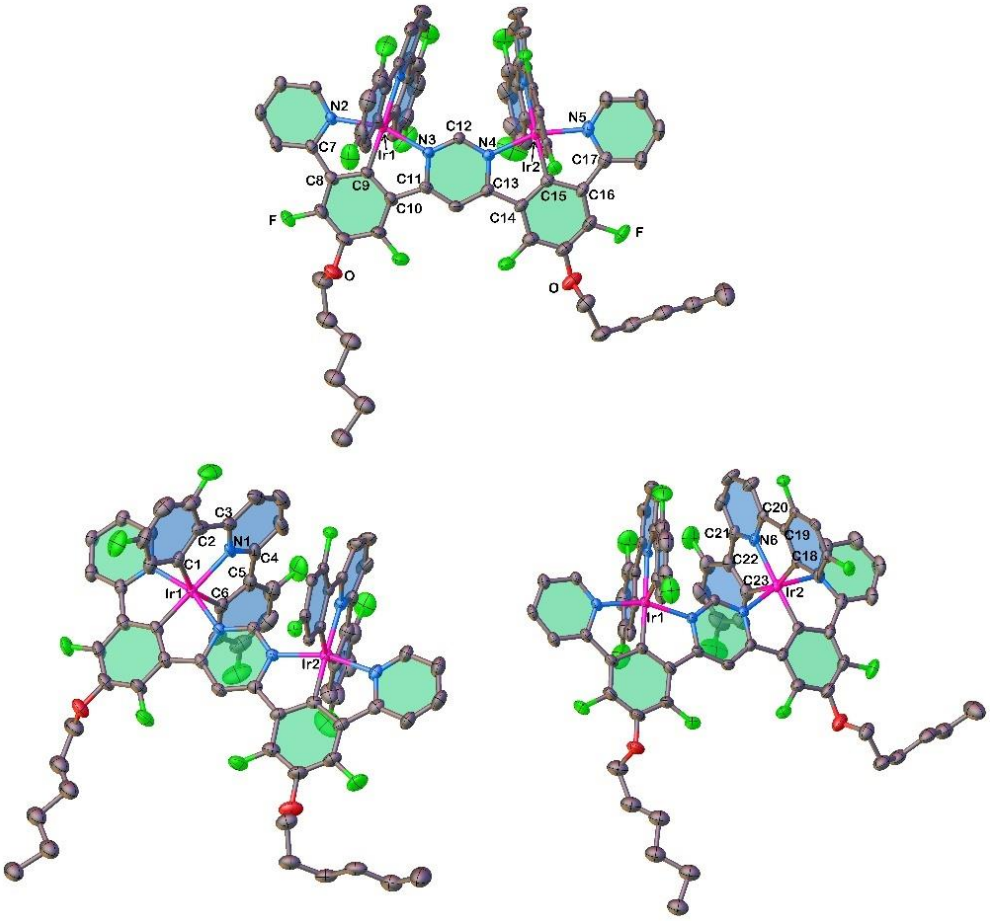

Figure 7.8. The XRD obtained molecular structure of complex **Ir-2** shown from different perspectives with atom numbering. (cf. ref.[91])

Table 7.1. Crystallographic data for complexes **IrCl**, **Ir_2Cl_2** and **IrIr**. (cf. ref.[19,69])

	IrCl	**Ir_2Cl_2**	**IrIr**
Crystallographic parameter			
CCDC number	1922650	1922651	1979956
Formula	$C_{60}H_{56}ClIrN_6$	$C_{99}H_{96}Cl_2Ir_2N_{10}O_3$	$C_{80.5}H_{85}Cl_7F_{10}Ir_2N_6O_2S$
$D_{calc.}$/ g cm^{-3}	1.384	1.316	1.662
μ/mm^{-1}	5.749	6.118	9.367
Formula Weight	1088.75	1929.15	2055.21
Colour	clear orange	orange	clear orange
Shape	prism	plate	needle
Size/mm^3	0.18×0.09×0.03	0.18×0.13×0.07	0.18×0.07×0.04
T/K	123.00(19)	123.00(10)	123.01(10)
Crystal System	triclinic	triclinic	monoclinic
Space Group	P-1	P-1	$P2_1/n$
a/Å	15.7708(4)	14.7346(2)	11.08060(10)
b/Å	18.1452(5)	14.9699(3)	15.66330(10)
c/Å	20.4160(6)	23.4455(3)	23.8140(2)
α/°	75.089(2)	74.6940(10)	90
β/°	68.707(3)	79.2030(10)	96.4830(10)
γ/°	78.676(2)	80.8400(10)	90
V/Å^3	5225.7(3)	4866.79(14)	4106.70(6)
Z	4	2	1
Z'	2	1	0.25
Wavelength/Å	1.54184	1.54184	1.54184
Radiation type	CuK_α	CuK_α	Cu K_α
Θ_{min}/°	2.372	3.392	3.384
Θ_{max}/°	74.066	73.867	76.387
Measured Refl.	56260	104437	67621
Independent Refl.	20352	19481	8564
Reflections Used	17799	17385	8035
R_{int}	0.0733	0.0386	0.0413
Parameters	1299	1137	613
Restraints	123	216	0
Largest Peak	1.947	1.450	1.340
Deepest Hole	-1.939	-1.575	-1.583
GooF	1.038	1.074	1.067
wR_2 (all data)	0.0985	0.0714	0.0847
wR_2	0.0941	0.0677	0.0831
R_1 (all data)	0.0421	0.0331	0.0312
R_1	0.0364	0.0280	0.0292

Table 7.2. Crystallographic data for complexes **Ir-1**, **Ir-2** and **IrPt**. (cf. ref.[61,91])

	Ir-1	**Ir-2**	**IrPt**
Crystallographic parameter			
CCDC number	1976640	1976641	1901014
Formula	$C_{39}H_{28}F_6IrN_3O$	$C_{72}H_{50}F_{12}Ir_2N_6O_2$	$C_{58}H_{67}IrN_4O_4Pt$
$D_{calc.}$/ g cm^{-3}	1.783	1.783	1.452
μ/mm^{-1}	8.697	9.134	9.146
Formula Weight	860.84	1657.65	1271.44
Colour	clear light yellow	clear brown	clear red
Shape	plate	prism	needle
Size/mm^3	0.18×0.07×0.06	0.19×0.06×0.05	0.34×0.09×0.05
T/K	123.01(10)	89.9(4)	123.01(10)
Crystal System	triclinic	triclinic	orthorhombic
Space Group	P-1	P-1	$Pca2_1$
a/Å	8.87020(10)	14.36016(16)	17.6736(2)
b/Å	9.84900(10)	18.2431(2)	20.2100(2)
c/Å	19.7342(3)	24.4691(3)	16.28070(10)
α/°	101.0260(10)	84.3111(10)	90
β/°	95.0430(10)	79.3824(10)	90
γ/°	106.5320(10)	79.1746(10)	90
V/Å^3	1603.59(4)	6174.54(13)	5815.20(9)
Z	2	4	4
Z'	1	2	1
Wavelength/Å	1.54184	1.54184	1.54184
Radiation type	Cu Kα	Cu Kα	CuKα
Θ_{min}/°	4.619	3.179	3.322
Θ_{max}/°	76.183	74.062	76.635
Measured Refl.	47220	128048	69489
Independent Refl.	6662	24556	11699
Reflections Used	6446	22067	11482
R_{int}	0.0446	0.0424	0.0387
Parameters	452	1798	685
Restraints	0	347	109
Largest Peak	1.495	2.197	1.244
Deepest Hole	-1.514	-1.699	-0.681
GooF	1.068	1.030	1.021
wR_2 (all data)	0.0569	0.0797	0.0707
wR_2	0.0563	0.0754	0.0700
R_1 (all data)	0.0231	0.0353	0.0276
R_1	0.0222	0.0304	0.0270

8. Supplementary information

8.1 Spin-orbit coupling (SOC), and triplet state zero field splitting (ZFS).

The probability (intensity) of electronic transitions in molecules is subject to selection rules which consider the wavefunction properties of the involved states and predict limitations that may arise. Transitions between states of different multiplicities, such as singlet↔triplet, that require spin-flip of an electron do not fulfill the spin-selection rule $\Delta S = 0$ (S is the total spin of a state involved in transition) and therefore are called spin-forbidden. Such forbiddenness, however, can be relaxed by Spin-Orbit Coupling (SOC).

SOC is an effect of coupling of an electron's spin magnetic moment (μ_s) with the magnetic moment induced by the movement of an electron around a charged nucleus (μ_l – angular magnetic moment). Strong SOC makes the spin momentum (s) and orbital momentum (l) of the electron inseparable from each other giving total (coupled) spin-orbit momentum (j = s+l). Therefore, in electronic systems with strong SOC the electronic transitions become subject to $\Delta J = 0$ selection rule, where J is a sum of the total spin (S) and total orbital momentum (L) (J = S+L) of an electronic state involved in the transition. Consequently, in such systems, the total spin of a state, and hence the spin multiplicity, can change during the transition if compensated by the change of the orbital angular momentum.

The strength of SOC at a particular atom depends on the spin-orbit coupling constant (ζ_ℓ) of the atom.[18,120] The SOC induced modulation of the electronic energy in an atom is proportional to the fourth power of the atomic nucleus' charge (Z^4)[8,18] and inversely proportional to the third power of the distance between the atomic nucleus and electron ($1/r^3$).[18] Because SOC weakens rapidly with the distance, the simple presence of a heavy atom in the molecule is not enough by itself for an electron to undergo strong SOC. It should also be probable that the electron of interest occurs at that heavy atom. This is defined by the contribution of the atom to the molecular orbital occupied by the electron. The larger the contribution of the heavy atom to a molecular orbital, the stronger the SOC it induces on the electrons which occupy the orbital.

The spin of a spin-orbit coupled electron can efficiently change only if the electronic structure of the molecule is such that the total (spin+orbital) angular momentum of the electron can be conserved ($\Delta j = 0$, where j = s + l) which ensures that $\Delta J = 0$. This condition is also known as El-Sayed's rule.[34] Accordingly, if the spin of a spin-orbit coupled electron changes by a unit of momentum (e.g. from $-1/2\hbar$ to $+1/2\hbar$, $\hbar$ - reduced Planck's constant), to compensate for this the coupled orbital angular momentum should also change its orientation by a unit of momentum. Considering *p* or *d* atomic orbitals, such change of orientation can be achieved by spatial rotation of the orbital by 90° along an axis perpendicular to the axis of the orbital, e.g., rotating p_x orbital

along the y-axis. Such rotation is the same as coinciding with another *p* or *d* orbital, respectively (*e.g* $p_x \rightarrow p_z$ or $d_{xz} \rightarrow d_{yz}$ rotation). For instance, the p_x-orbital rotated by 90° along the y-axis coincides with the p_z-orbital. In other words, a spin-orbit coupled electron can flip its spin conserving the total momentum by with simultaneous change of its orbital. It is favorable for efficient SOC if the two atomic orbitals are (*quasi*)-degenerate, the importance of which is discussed further below.

Favorable conditions for efficient SOC of excited states, for example, are found in octahedral complexes of d^6 metals with large SOC constant such as Ir(III) (ζ_ℓ(Ir) = 3909 cm^{-1}).[33] Here, the octahedral ligand field splits the d orbitals to a set of lower laying quasi-degenerate d_{xy}, d_{xz}, d_{yz} orbitals of t_{2g} symmetry and to a set of higher laying orbitals d_{z2} and d_{x2-y2} of e_g symmetry. In the metal centers with d^6 electronic configuration, such as Ir(III), the lower laying d-orbitals d_{xy}, d_{xz}, d_{yz} are doubly occupied. Therefore, in complexes of Ir(III) with organic cyclometalating ligands, such as the archetypal $Ir(ppy)_3$ (ppyH – 2-phenylpyridine), the d_{xy}, d_{xz} and d_{yz} atomic orbitals of iridium contribute to several highest occupied MOs. Consequently, the lowest triplet T_1 state has significant metal to ligand (π* orbital) charge transfer character (^{3}MLCT) or $^3d_i\pi^*$, where d_i is a t_{2g} atomic orbital of Ir. Such triplet state has an unpaired electron partially localized at the iridium atom (on the d_i orbital). The SOC effect at the Iridium atom can flip the spin of this electron as coupled with orbital rotation $d_i \rightarrow d_j$, where d_j is another t_{2g} d-orbital of Ir orthogonal to d_i, consequently changing the character and multiplicity of the electronic state to singlet $^1d_j\pi^*$. This transition can occur in both directions, $^3d_i\pi^* \leftrightarrow {}^1d_j\pi^*$, with the ΔJ=0 rule fulfilled. It is said that the states $^3d_i\pi^*$ and $^1d_j\pi^*$ are coupled by SOC induced at the heavy atom of a transition metal. Similarly, state T_1 can also couple with another singlet state via another t_{2g} d-orbital of the Ir atom. Such SOC paths perturb the state T_1 endowing it with some singlet character which affects the transitions probabilities between T_1 state and other singlets. In particular, the SOC induced singlet admixtures to state T_1 are largely responsible for fulfilling the ΔJ = 0 rule (or relaxing the ΔS = 0 rule) for phosphorescent transition $T_1 \rightarrow S_0$ thus enhancing its probability (rate) significantly.

The quasi-degeneracy of d_{xy}, d_{xz}, d_{yz} orbitals at the Ir(III) center strongly favors efficient SOC. A large energy separation between orbitals d_i and d_j ($\Delta E(d_j - d_i)$) would result in the unpaired electron at the iridium atom being trapped in the higher energy orbital d_i (with the lower energy d_j orbital doubly occupied) which traps the molecule in the lower energy state $^3d_i\pi^*$ (T_1).[8] In such a case $d_i \leftrightarrow d_j$ orbital rotation is retarded and, consequently, SOC of state $^3d_i\pi^*$ (T_1) with the $^1d_j\pi^*$ singlet state is diminished. In general, projecting the contribution of the energy gap between orbitals $\Delta E(d_j - d_i)$ to the energy gap between states $^1d_j\pi^*$ (S_n) and $^3d_i\pi^*$ (T_1), $\Delta E(^1d_j\pi^* - {}^3d_i\pi^*)$, it can be said that a smaller gap between the states favors stronger SOC of the states.

A triplet state corresponds to three variants of mutual orientations of the two unpaired spins when they couple constructively which represent the three substates of the triplet (Figure 8.1).

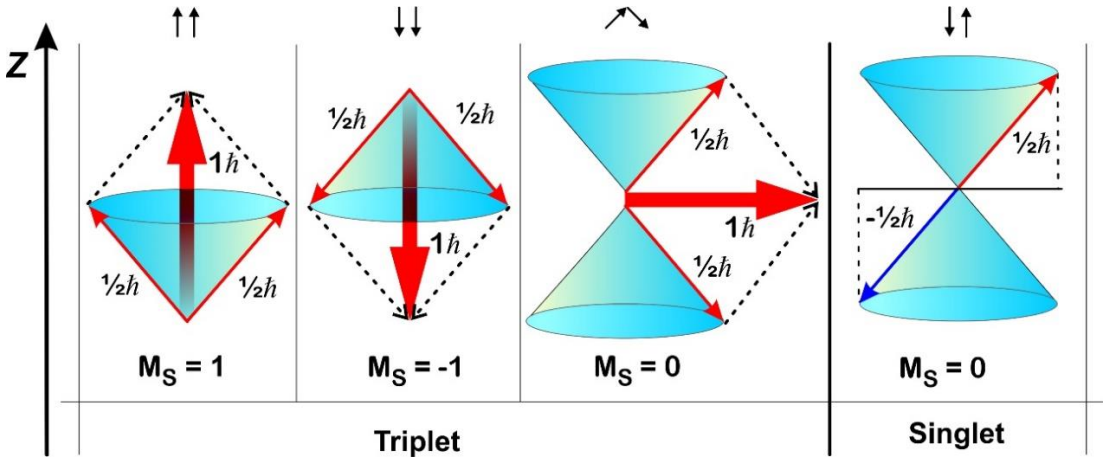

Figure 8.1. Schematic representation of four possible mutual orientations of the two unpaired spins. Three variants correspond to substates of a triplet state and one to a single state. M_S -total magnetic moment with respect to the direction Z.

Since the distribution of the electron density at the SOC inducing atom is typically not spherically symmetric, the electromagnetic field around the atom is also not uniform (anisotropic). Therefore, different orientations of an unpaired spin at the SOC inducing atom, undergo SOC of different strengths. As a result, the three substates of a triplet state become non-degenerate and split in energy that is called *zero-field splitting* (ZFS) e.g., splitting in the absence of an externally applied field. Considering the SOC of the state T_1 with higher-lying excited states, a T_1 substate having stronger SOC obtains larger energy correction (more admixtures of higher laying states) and therefore is higher in energy than a substate having weaker SOC. Therefore, the higher T_1 substates often have more SOC-induced singlet admixtures and, consequently, higher radiative transition rates to other singlet states, for example to the singlet ground state (S_0). For instance, considering the metal center of coordination compounds, the field anisotropy is brought by spherically non-symmetric coordination patterns. This makes different directions of the spin magnetic moment not equal to the electron's orbital magnetic moment and brings differences in SOC induced energy correction to the three T_1 substates. When the electromagnetic field at the SOC center is less anisotropic, the ZFS is smaller because the SOC induced energy corrections for the three substates become closer in values, although their absolute magnitudes can still be large.[68]

Due to the ZFS effect, the triplet substates have different thermal populations, which is a Boltzmann-type dependency function. Since the three substates also differ by the radiative rates, the emission rate is sensitive to temperature, especially at low temperatures. This allows the assessment of the T_1 substate radiative rates and ZFS size by measuring the variation of emission

decay time in a wide range of temperatures, given that the emission quantum yield does no vary strongly, which is exploited in Chapter 1, 2, 4 and 5.

8.2 Supporting data.

Table 8.1. The key structural parameters derived from single crystal XRD experiment and DFT optimized ground state (S_0) and T_1 state geometries of complex **IrCl**. The atom numbering corresponds to that given in Figure 1.1. esd – estimated standard deviation. The asymmetric unit sell of **IrCl** contains two independent molecules. (cf. ref.[19])

Parameter	XRD (esd)		Ground state (S_0)	Emitting state (T_1)
	Molecule 1	Molecule 2		
Bonds (Å)				
Ir−C1	2.011(3)	2.025(3)	1.999	2.001
Ir−C10	1.945(4)	1.944(4)	1.935	1.947
Ir−N1	2.152(4)	2.165(4)	2.164	2.176
Ir−N3	2.059(3)	2.056(3)	2.053	2.026
Ir−N4	2.049(3)	2.061(3)	2.053	2.022
Ir−Cl	2.4581(8)	2.4833(11)	2.494	2.451
N1−C3	1.366(4)	1.351(4)	1.347	1.355
N2−C5	1.356(4)	1.354(4)	1.335	1.346
Angles (degree^o)				
C1−Ir−N1	78.71(14)	78.94(14)	78.551	78.911
N3−Ir−C10	79.23(13)	78.23(15)	79.141	79.950
C1−Ir−C10	92.61(15)	90.15(14)	94.139	93.850
N1−Ir−Cl	92.67(8)	93.22(9)	94.258	94.167
C10−Ir−Cl	96.02(9)	97.72(9)	93.052	93.073
C1−Ir−Cl	171.37(12)	171.77(13)	172.808	173.067
N3−Ir−N4	158.19(14)	157.76(15)	158.251	159.833
N1−Ir−C10	171.17(11)	169.06(12)	172.690	172.760
Torsion angles (degree^o)				
C1−Ir−C10−C9	86.9(2)	76.7(3)	86.549	86.217
C1−Ir−C10−C11	87.80(18)	88.0(3)	86.677	86.010
C1−Ir−N3−C8	91.0(2)	81.9(2)	93.395	93.508
C1−Ir−N4−C12	88.5(2)	89.2(2)	93.145	93.435
C4−N1−Ir−N3	88.4(3)	94.4(4)	91.969	92.286
C4−N1−Ir−Cl	3.8(3)	2.6(4)	0.431	0.152
Cl−Ir−C10−C9	93.0(2)	100.9(3)	93.345	94.166
Ir1−N1−C4−N2	179.9(3)	179.7(3)	179.735	179.652

Table 8.2. The key structural parameters derived from single crystal XRD experiment and DFT optimized ground state (S_0) and T_1 state geometries of complex **Ir_2Cl_2**. The atom numbering corresponds to that given in Figure 1.1. esd – estimated standard deviation. (cf. ref.[19])

Parameter	XRD (esd)	DFT	
		Ground state (S_0)	Emitting state (T_1)
Bonds (Å)			
Ir1−C1	2.018(3)	2.000	1.997
Ir1−C10	1.946(2)	1.932	1.940
Ir1−N1	2.143(3)	2.171	2.162
Ir1−N3	2.058(2)	2.058	2.049
Ir1−N4	2.057(2)	2.051	2.041
Ir1−Cl1	2.4776(8)	2.484	2.469
Ir2−C7	2.009(3)	2.000	1.997
Ir2−C15	1.951(3)	1.933	1.939
Ir2−N2	2.133(3)	2.171	2.161
Ir2−N5	2.060(2)	2.052	2.041
Ir2−N6	2.068(3)	2.058	2.051
Ir2−Cl2	2.4654(8)	2.484	2.470
N1−C3	1.375(4)	1.353	1.376
N2−C5	1.374(4)	1.353	1.376
Angles (degree^o)			
C1−Ir1−N1	78.64(11)	78.489	79.355
N3−Ir1−C10	79.25(11)	79.182	79.452
C1−Ir1−C10	92.25(12)	93.289	92.723
N1−Ir1−Cl	92.04(6)	93.342	93.312
C10−Ir1−Cl	97.00(9)	94.799	94.527
C1−Ir1−Cl	170.13(9)	171.439	172.075
N3−Ir1−N4	157.97(11)	158.266	158.749
N1−Ir1−C10	170.85(10)	171.638	171.972
C7−Ir2−N2	78.89(11)	78.515	79.350
N5−Ir2−C15	79.05(12)	79.059	79.299
C7−Ir2−C15	94.56(13)	93.454	92.941
N2−Ir2−Cl2	91.06(7)	93.266	93.208
C15−Ir2−Cl2	95.38(9)	94.679	94.415
C7−Ir2−Cl2	169.72(9)	171.278	171.895
N5−Ir2−N6	157.84(10)	158.253	158.698
N2−Ir−C15	173.00(12)	171.845	172.186
Torsion angles (degree^o)			
C1−Ir1−C10−C9	85.8(2)	84.402	84.108
C1−Ir1−N3−C8	92.7(2)	92.981	91.960
C1−Ir1−N4−C12	84.7(2)	90.106	89.030
C4−N1−Ir1−N3	101.6(2)	98.638	99.096
C4−N1−Ir1−Cl1	11.4(2)	7.772	8.940
Cl1−Ir1−C10−C9	90.7(2)	94.803	95.337
C7−Ir2−C15−C14	90.7(3)	88.863	88.493
C7−Ir2−N5−C13	90.4(2)	90.633	89.622
C7−Ir2−N6−C17	94.33(19)	93.023	92.248
C4−N2−Ir2−N5	83.3(3)	83.557	82.863
C4−N2−Ir2−Cl2	7.6(2)	7.865	8.677
Cl2−Ir2−C15−C14	92.0(2)	94.291	94.915
Ir1−N1−C4−N2	175.3(2)	171.055	170.995
Ir2−N2−C4−N1	167.1(2)	170.557	170.244

Table 8.3. DFT calculated frontier orbital energies and atomic contributions of complex **IrCl** in the state T_1 geometry resulting from Mulliken population analysis. (cf. ref.[19])

Orbital	Energy, eV	Contribution (Mulliken), (%)			
		Ir	Phbib	Cl	dpp
LUMO+4	−1.959	0	99	1	0
LUMO+3	−2.255	4	94	1	1
LUMO+2	−2.338	1	1	0	98
LUMO+1	−2.872	2	1	0	97
LUMO	−3.012	2	97	0	0
HOMO	−4.927	45	21	22	12
HOMO−1	−5.121	41	23	31	5
HOMO−2	−5.783	43	31	15	11
HOMO−3	−5.840	12	59	20	9
HOMO−4	−5.876	12	58	18	12

dpp – diphenylpyrimidine

Phbib – 1,3-bis(N-phenylbenzimidazolyl)-5-*tert*-butylbenzene

Table 8.4. DFT calculated frontier orbital energies and atomic contributions of complex **Ir_2Cl_2** in the state T_1 geometry resulting from Mulliken population analysis. (cf. ref.[19])

Orbitals	Energy, eV	Contribution (Mulliken), (%)						
		Ir1	Phbib1	Cl1	dpp	Ir2	Phbib2	Cl2
LUMO+4	−2.073	2	57	0	1	2	38	0
LUMO+3	−2.258	1	2	0	95	1	1	0
LUMO+2	−2.709	0	1	0	3	2	94	0
LUMO+1	−2.714	2	92	0	5	0	1	0
LUMO	−2.919	2	5	0	87	2	4	0
HOMO	−4.906	22	8	13	19	20	7	12
HOMO−1	−4.958	21	8	13	16	22	7	14
HOMO−2	−5.013	20	12	17	4	19	12	16
HOMO−3	−5.068	18	12	15	4	20	14	16
HOMO−4	−5.600	24	16	5	13	22	15	4
HOMO−5	−5.610	18	8	15	15	19	9	16

dpp – diphenylpyrimidine

Phbib1 – 1,3-bis(N-phenylbenzimidazolyl)-5-*tert*-butylbenzene coordinated to Ir1

Phbib2 – 1,3-bis(N-phenylbenzimidazolyl)-5-*tert*-butylbenzene coordinated to Ir2

Table 8.5. TD-DFT calculated lowest triplet and singlet states of **IrCl** in the T_1 state geometry. (cf. ref.[19])

State, energy (eV)	*f* (oscillator strength)	Contributing transition coefficients*	Character**
triplets			
T_1, 1.781	(triplet)	HOMO→LUMO (0.70)	$MXL^{Phbib}CT$
T_2, 2.027	(triplet)	HOMO→LUMO+1 (0.70)	$MXL^{dpp}CT$
T_3, 2.058	(triplet)	HOMO−1→LUMO (0.70)	$MXL^{Phbib}CT$
singlets			
S_1, 2.031	0.0759	HOMO→LUMO (0.66) HOMO→LUMO+1 (0.21)	$MXL^{Phbib}CT$\ $MXL^{dpp}CT$
S_2, 2.084	0.0004	HOMO→LUMO (-0.21) HOMO→LUMO+1 (0.67)	$MXL^{dpp}CT$\ $MXL^{Phbib}CT$
S_3, 2.180	0.0772	HOMO−1→LUMO (0.70)	$MXL^{Phbib}CT$
S_4, 2.250	0.0009	HOMO−→LUMO+1 (0.70)	$MXL^{dpp}CT$
S_5, 2.613	0.0066	HOMO→LUMO+2 (0.70)	$MXL^{dpp}CT$

*Square of the coefficient multiplied by two gives percentage contribution of the transition to formation of the excited state.

**MXLCT – Metal (M) and Halide (X) to Ligand (L) Charge Transfer.

Table 8.6. TD-DFT calculated lowest triplet and singlet states of **Ir_2Cl_2** in the T_1 state geometry. (cf. ref.[19])

State, Energy (eV)	*f* (oscillator strength)	Transition (coefficient)*	Character**
triplets			
T_1, 1.954	(triplet)	HOMO→LUMO (0.70)	$MXL^{dpp}CT$
T_2, 2.001	(triplet)	HOMO−1→LUMO (0.70)	$MXL^{dpp}CT$
T_3, 2.077	(triplet)	HOMO−2→LUMO (0.70)	$MXL^{dpp}CT$
singlets			
S_1, 2.030	0.1359	HOMO→LUMO (0.70)	$MXL^{dpp}CT$
S_2, 2.079	0.0097	HOMO−2→LUMO (−0.12) HOMO−1→LUMO (0.69)	$MXL^{dpp}CT$
S_3, 2.100	0.0063	HOMO−2→LUMO (0.70) HOMO−1→LUMO (0.11)	$MXL^{dpp}CT$
S_4, 2.156	0.0010	HOMO−3→LUMO (0.70)	$MXL^{dpp}CT$
S_5, 2.216	0.0027	HOMO−1→LUMO+1 (0.33) HOMO→LUMO+1 (0.57) HOMO→LUMO+2 (0.24)	$MXL^{Phbib}CT$

*Square of the given coefficient multiplied by two gives percentage contribution of the corresponding transition to formation of the excited state.

**MXLCT – Metal (M) and Halide (X) to Ligand (L) Charge Transfer.

Table 8.7. DFT calculated frontier orbital energies and atomic contributions of complex **Ir_2I_2** in the state T_1 geometry resulting from Mulliken population analysis. (cf. ref.[59])

Orbitals	Energy, eV	Contribution (Mulliken), (%)						
		Ir1	Phbib1	I1	dpp	Ir2	Phbib2	I2
LUMO+2	−2.735	0	6	0	2	2	90	0
LUMO+1	−2.740	2	89	2	3	0	4	0
LUMO	−3.069	2	3	0	90	2	3	0
HOMO	−4.932	8	2	37	6	8	2	37
HOMO−1	−5.016	12	6	34	6	10	5	27
HOMO−2	−5.039	9	3	29	6	12	4	37
HOMO−3	−5.135	9	5	33	4	10	6	33
HOMO−4	−5.400	13	14	13	15	14	18	14
HOMO−5	−5.424	9	23	20	9	11	24	13
HOMO−6	−5.471	5	15	11	5	10	30	24
HOMO−7	−5.531	10	30	17	6	6	20	11
HOMO−8	−5.744	7	13	27	19	6	9	19
HOMO−9	−5.771	2	15	25	13	2	14	29

dpp – diphenylpyrimidine

Phbib1 – 1,3-bis(N-phenylbenzimidazolyl)-5-*tert*-butylbenzene coordinated to Ir1

Phbib2 – 1,3-bis(N-phenylbenzimidazolyl)-5-*tert*-butylbenzene coordinated to Ir2

Table 8.8. TD-DFT calculated lowest triplet and singlet states of **Ir_2I_2** in the T_1 state geometry. (cf. ref.[59])

State, Energy (eV)	*f* (oscillator strength)	Transition (coefficient)*	Character**
triplets			
T_1, 1.971	(triplet)	HOMO→LUMO (0.71)	$MXL^{dpp}CT$
T_2, 2.058	(triplet)	HOMO−1→LUMO (0.71)	$MXL^{dpp}CT$
T_3, 2.074	(triplet)	HOMO−2→LUMO (0.70)	$MXL^{dpp}CT$
singlets			
S_1, 1.990	0.0160	HOMO→LUMO (0.70)	$MXL^{dpp}CT$
S_2, 2.086	0.0341	HOMO−1→LUMO (0.70)	$MXL^{dpp}CT$
S_3, 2.107	0.0098	HOMO−2→LUMO (0.70)	$MXL^{dpp}CT$
S_4, 2.199	0.0010	HOMO−3→LUMO (0.70)	$MXL^{dpp}CT$
S_5, 2.227	0.0047	HOMO→LUMO+1 (0.67) HOMO→LUMO+2 (0.21)	$MXL^{Phbib1}CT$
S_6, 2.229	0.0023	HOMO→LUMO+1 (-0.21) HOMO→LUMO+2 (0.67)	$MXL^{Phbib2}CT$

*Square of the given coefficient multiplied by two gives percentage contribution of the corresponding transition to formation of the excited state.
**MXLCT – Metal (M) and Halide (X) to Ligand (L) Charge Transfer.

Table 8.9. The key structural parameters of complex **IrIr** derived from single crystal XRD experiment and DFT optimized ground state (S_0) and T_1 state geometries of **IrIr'**. The atom numbering corresponds to that given in Figure 3.1. esd – estimated standard deviation. (cf. ref.[69])

Parameter	XRD (esd)*	DFT	
		Ground state (S_0)	Emitting state (T_1)
Bonds (Å)			
Ir−C1	2.011(3)	1.995	1.983
Ir-C6	1.933(3)	1.918	1.921
Ir−N1	2.174(3)	2.201	2.195
Ir−N2	2.055(3)	2.053	2.054
Ir−N3	2.054(3)	2.053	2.054
Ir−Cl	2.4314(8)	2.479	2.474
C1−C2	1.392(5)	1.392	1.436
C2−C3	1.431(5)	1.427	1.408
C3−N1	1.364(4)	1.352	1.367
Angles (degree^o)			
C1−Ir−N1	78.75(12)	78.361	79.584
C1−Ir−C6	96.41(13)	96.103	95.168
N2−Ir−N3	160.08(13)	160.786	160.854
C1−Ir−Cl	169.67(10)	171.582	172.610
N1−Ir−N2	100.63(12)	99.548	99.530
N2−Ir−Cl	87.54(8)	90.531	90.399
Torsion angles (degree^o)			
C1−C2−C3−N1	0.8(4)	0.047	0.000
N2−C4−C5−C6	5.9(4)	0.035	0.040
C4−C5−C6−C7	0.8(4)	179.557	179.417
C3−N1−Ir−N2	84.5(2)	88.973	89.086
C3−N1−Ir−N3	97.4(2)	88.859	89.086
C3−N1−Ir−Cl	172.3(2)	179.946	180.000
C4−N2−Ir−Cl	88.6(2)	92.334	92.572

Table 8.10. DFT calculated frontier orbital energies and atomic contributions of complex **IrIr'** in the state T_1 geometry resulting from Mulliken population analysis. (cf. ref.[69])

Orbitals	Energy, eV	Contribution (Mulliken), (%)						
		Ir1	NCN1	Cl1	CN−CN	Ir2	NCN2	Cl2
LUMO+4	−2.669	2	47	1	0	2	47	1
LUMO+3	−2.678	3	46	1	0	3	46	1
LUMO+2	−2.810	1	49	0	0	1	49	0
LUMO+1	−2.815	1	49	0	0	1	49	0
LUMO	−3.473	1	1	0	96	1	1	0
HOMO	−5.168	8	2	2	76	8	2	2
HOMO−1	−5.624	20	21	7	4	20	21	7
HOMO−2	−5.660	23	7	11	19	23	7	11
HOMO−3	−5.665	8	2	7	66	8	2	7
HOMO−4	−5.976	19	10	8	26	19	10	8

CN−CN – ditopic C^N–C^N ligand bridging the two metal centers

NCN1 – N^C^N ligand coordinated to Ir1

NCN2 – N^C^N ligand coordinated to Ir2

Table 8.11. TD-DFT calculated lowest triplet and singlet states of **IrIr'** in the T_1 state geometry. (cf. ref.[69])

State, energy (eV)	*f* (oscillator strength)	Contributing transition coefficients*	Character**
triplets			
T_1, 1.514	(triplet)	HOMO→LUMO (0.70)	LC^{CN-CN}/ $M^{Ir1/Ir2}L^{CN-CN}CT$
T_2, 2.124	(triplet)	HOMO−2→LUMO (0.70)	$M^{Ir1/Ir2}L^{CN-CN}CT$/$L^{Cl1/Cl2}L^{CN-CN}CT$/ LC^{CN-CN}
T_3, 2.140	(triplet)	HOMO−1→LUMO (0.70)	$M^{Ir1/Ir2}L^{CN-CN}CT$/$L^{Cl1/Cl2}L^{CN-CN}CT$/ $L^{NCN1/NCN2}L^{CN-CN}CT$
T_4, 2.182	(triplet)	HOMO−3→LUMO (0.70)	LC^{CN-CN} /$M^{Ir1/Ir2}L^{CN-CN}CT$/ $L^{Cl1/Cl2}L^{CN-CN}CT$
T_5, 2.344	(triplet)	HOMO→LUMO+1 (0.70)	$L^{CN-CN}L^{NCN1/NCN2}CT$
singlets			
S_1, 2.048	0.2915	HOMO→LUMO (0.68) HOMO−4→LUMO (−0.15)	LC^{CN-CN}/ $M^{Ir1/Ir2}L^{CN-CN}CT$
S_2, 2.153	0.0000	HOMO−1→LUMO (0.70)	$M^{Ir1/Ir2}L^{CN-CN}CT$/$L^{Cl1/Cl2}L^{CN-CN}CT$/ $L^{NCN1/NCN2}L^{CN-CN}CT$
S_3, 2.194	0.0012	HOMO−3→LUMO (0.71)	LC^{CN-CN} /$M^{Ir1/Ir2}L^{CN-CN}CT$/ $L^{Cl1/Cl2}L^{CN-CN}CT$
S_4, 2.252	0.0000	HOMO−2→LUMO (0.70)	$M^{Ir1/Ir2}L^{CN-CN}CT$/$L^{Cl1/Cl2}L^{CN-CN}CT$/ LC^{CN-CN}
S_5, 2.359	0.0184	HOMO→LUMO+1 (0.71)	$L^{CN-CN}L^{NCN1/NCN2}CT$

*Square of the coefficient multiplied by two gives percentage contribution of the transition to formation of the excited state.

** MLCT – Metal (M) to Ligand (L) Charge Transfer. LC−Ligand Centered. LLCT – Ligand to Ligand Charge Transfer.

Table 8.12. The key structural parameters of **Ir-1** derived from single crystal XRD experiment and DFT optimized ground state (S_0) and T_1 state geometries of model complex **Ir-1'**. The atom numbering corresponds to that given in Figure 7.7. esd – estimated standard deviation (cf. ref.[91])

Parameter	XRD (esd)*	DFT	
		Ground state (S_0)	Emitting state (T_1)
Bonds (Å)			
Ir−C1	2.070(3)	2.078	2.071
Ir−C6	2.071(3)	2.077	2.067
Ir−C9	1.928(2)	1.916	1.909
Ir−N1	2.0689(17)	2.085	2.147
Ir−N2	2.049(3)	2.050	2.060
Ir−N3	2.049(3)	2.050	2.061
Angles (degree^o)			
C1−Ir−N1	79.23(9)	78.817	75.661
C1−Ir−C6	158.24(10)	157.662	151.635
N2−Ir−N3	160.11(7)	160.205	162.263
N2−Ir−C9	79.86(10)	80.103	81.175
C1−Ir−C9	102.17(10)	101.282	105.647
N1−Ir−N2	104.41(9)	99.898	98.745
Torsion angles (degree^o)			
C1−C2−C3−N1	6.6(5)	0.000	0.279
C2−C3 −N1−C4	176.8(3)	180.000	179.914
N2−C7−C8−C9	0.9(3)	0.183	1.058
C7−C8−C9−C10	179.0(3)	179.957	179.420
C3−N1−Ir−N2	92.8(3)	89.989	89.288
C3−N1−Ir−N3	89.1(3)	89.988	89.565

Table 8.13 The key structural parameters of **Ir-2** derived from single crystal XRD experiment and DFT optimized ground state (S_0) and T_1 state geometries of model complex **Ir-2'**. The atom numbering corresponds to that given in Figure 7.8. esd – estimated standard deviation. (cf. ref.[91])

Parameter	XRD (esd)		DFT	
	Molecule 1	Molecule 2	Ground state (S_0)	Emitting state (T_1)
Bonds (Å)				
Ir1−C1	2.082(4)	2.085(3)	2.077	2.075
Ir1−C6	2.087(4)	2.071(3)	2.084	2.080
Ir1−C9	1.929(5)	1.931(4)	1.916	1.917
Ir1−N1	2.099(4)	2.075(3)	2.089	2.116
Ir1−N2	2.055(3)	2.049(3)	2.049	2.061
Ir1−N3	2.055(3)	2.055(3)	2.045	2.045
Ir2−C18	2.074(4)	2.084(4)	2.079	2.076
Ir2−C23	2.087(4)	2.086(6)	2.079	2.076
Ir2−C15	1.912(4)	1.920(5)	1.915	1.917
Ir2−N6	2.087(4)	2.075(4)	2.088	2.116
Ir2−N4	2.038(3)	2.051(3)	2.043	2.043
Ir2−N5	2.055(4)	2.043(3)	2.047	2.058
Angles (degree^o)				
C1−Ir1−N1	78.30(16)	79.13(13)	78.806	77.488
C1−Ir1−C6	156.27(19)	158.18(5)	157.099	154.264
N2−Ir1−N3	159.35(14)	159.87(13)	159.662	160.765
N2−Ir1−C9	80.08(15)	80.32(16)	80.236	80.345
C1−Ir1−C9	102.65(17)	97.76(15)	97.823	99.320
N1−Ir1−N2	99.24(13)	99.20(12)	98.141	97.553
C18−Ir2−N6	79.21(15)	78.88(15)	78.711	77.289
C18−Ir2−C23	157.54(18)	157.23(17)	157.475	154.618
N4−Ir2−N5	160.10(15)	159.46(15)	160.003	161.109
N4−Ir2−C15	79.58(15)	79.14(15)	79.894	80.973
C18−Ir2−C15	101.36(16)	103.59(16)	102.739	103.995
N6−Ir2−N5	97.67(14)	100.45(13)	101.608	102.009
Torsion angles (degree^o)				
C1−C2−C3−N1	4.7(5)	2.9(4)	2.949	3.426
C2−C3 −N1−C4	178.4(4)	178.4(3)	178.808	179.091
N2−C7−C8−C9	1.4(5)	0.6(5)	1.159	1.035
C7−C8−C9−C10	179.3(4)	179.4(3)	178.603	178.860
C3−N1−Ir1−N2	85.1(3)	87.3(2)	86.620	86.391
C3−N1−Ir1−N3	96.2(3)	94.4(2)	94.327	94.271
Ir1−N3−C12−N4	171.5(3)	174.6(3)	173.412	173.270
C18−C19−C20−N6	6.6(5)	6.0(5)	2.107	2.474
C19−C20 −N6−C21	179.0(3)	176.6(3)	178.852	179.124
N5−C17−C16−C15	3.3(5)	1.1(6)	1.023	0.915
C17−C16−C15−C14	179.8(3)	179.1(4)	177.764	177.931
C20−N6−Ir2−N5	86.6(3)	84.9(3)	90.041	90.732
C20−N6−Ir2−N4	93.7(3)	94.5(3)	91.123	90.150
Ir2−N4−C12−N3	178.2(5)	175.9(3)	171.444	171.914

Table 8.14. DFT calculated frontier orbital energies and atomic contributions of complex **Ir-1'** in the state T_1 geometry resulting from Mulliken population analysis. (cf. ref.[91])

Orbital	Energy, eV	Contribution (Mulliken), (%)		
		Ir	CNC	NCN
LUMO+4	−2.063	1	11	88
LUMO+3	−2.283	2	90	8
LUMO+2	−2.473	7	7	86
LUMO+1	−2.561	4	95	1
LUMO	−2.852	1	1	98
HOMO	−4.815	27	38	35
HOMO−1	−5.577	33	57	10
HOMO−2	−6.056	9	79	12
HOMO−3	−6.190	48	28	14
HOMO−4	−6.225	4	29	66

CNC – the C^N^C ligand
NCN – the N^C^N ligand

Table 8.15. DFT calculated frontier orbital energies and contributions of complex **Ir-2'** in the state T_1 geometry resulting from Mulliken population analysis. (cf. ref.[91])

Orbitals	Energy, eV	Contribution (Mulliken), (%)				
		Ir1	CNC1	2×NCN	CNC2	Ir2
LUMO+4	−2.552	2	39	2	55	2
LUMO+3	−2.613	3	4	87	3	3
LUMO+2	−2.652	2	57	2	37	2
LUMO+1	−2.897	1	1	95	2	1
LUMO	−3.334	3	3	89	2	3
HOMO	−4.979	14	18	33	20	15
HOMO−1	−5.250	14	20	36	18	12
HOMO−2	−5.571	13	25	11	33	17
HOMO−3	−5.721	15	36	6	31	12
HOMO−4	−6.066	5	36	9	43	7
HOMO−5	−6.140	11	29	8	38	14
HOMO−6	−6.177	18	34	9	21	18
HOMO−7	−6.310	19	28	8	23	23
HOMO−8	−6.385	0	5	68	24	1
HOMO−9	−6.426	1	23	72	3	0

2×NCN – the ditopic bis−terdentate ligand N^C^N – N^C^N
CNC1 – C^N^C ligand coordinated to metal ion Ir1
CNC2 – C^N^C ligand coordinated to metal ion Ir2

Table 8.16. TD-DFT calculated lowest triplet and singlet states of **Ir-1'** in the T_1 state geometry. (cf. ref.[91])

State, energy (eV)	*f* (oscillator strength)	Contributing transition coefficients*	Character**
triplets			
T_1, 1.902	(triplet)	HOMO→LUMO (0.71)	$ML^{NCN}CT/LC^{NCN}$
T_2, 2.164	(triplet)	HOMO→LUMO+2 (0.70)	$ML^{NCN}CT/ LC^{NCN}$
T_3, 2.208	(triplet)	HOMO→LUMO+1 (0.70)	$ML^{CNC}CT/ LC^{CNC}$
singlets			
S_1, 2.116	0.1193	HOMO→LUMO (0.70)	$ML^{NCN}CT/LC^{NCN}$
S_2, 2.261	0.0011	HOMO→LUMO+1 (0.70)	$ML^{CNC}CT/ LC^{CNC}$
S_3, 2.535	0.0060	HOMO→LUMO+3 (0.70)	$ML^{CNC}CT/ LC^{CNC}$
S_4, 2.568	0.0087	HOMO→LUMO+2 (0.70)	$ML^{NCN}CT/ LC^{NCN}$
S_5, 2.770	0.0184	HOMO−1→LUMO (0.67)	$ML^{NCN}CT/ L^{CNC}L^{NCN}CT$
S_6, 2.796	0.0261	HOMO→LUMO+5 (0.70)	$ML^{NCN}CT/ LC^{NCN}$
S_7, 2.951	0.0196	HOMO→LUMO+6 (0.68)	$ML^{CNC}CT/ L^{NCN}L^{CNC}CT$
S_8, 3.058	0.0036	HOMO−1→LUMO+1 (0.70)	$ML^{CNC}CT/ CT^{CNC}$

*Square of the coefficient multiplied by two gives percentage contribution of the transition to formation of the excited state.

** MLCT – Metal (M) to Ligand (L) Charge Transfer. LC−Ligand Centered. LLCT – Ligand to Ligand Charge Transfer.

Table 8.17. TD-DFT calculated lowest triplet and singlet states of **Ir-2'** in the T_1 state geometry. (cf. ref.[91])

State, Energy (eV)	*f* (oscillator strength)	Transition (coefficient)*	Character**
triplets			
T_1, 1.580	(triplet)	HOMO→LUMO (0.71)	$M^{Ir1/Ir2}L^{2xNCN}$ CT/LC^{2xNCN}
T_2, 1.789	(triplet)	HOMO−1→LUMO (0.69)	$M^{Ir1/Ir2}L^{2xNCN}$ CT/LC^{2xNCN}
T_3, 2.025	(triplet)	HOMO→LUMO+1 (0.70)	$M^{Ir1/Ir2}L^{2xNCN}$ CT/LC^{2xNCN}
singlets			
S_1, 1.794	0.3373	HOMO→LUMO (0.70)	$M^{Ir1/Ir2}L^{2xNCN}$ CT/LC^{2xNCN}
S_2, 2.050	0.0240	HOMO−1→LUMO (0.66)	$M^{Ir1/Ir2}L^{2xNCN}$ CT/LC^{2xNCN}
S_3, 2.159	0.0025	HOMO→LUMO+1 (0.68)	$M^{Ir1/Ir2}L^{2xNCN}$ CT/LC^{2xNCN}
S_4, 2.297	0.0396	HOMO−2→LUMO (0.67)	$M^{Ir1/Ir2}L^{2xNCN}$ CT/$L^{CNC1/CNC2}L^{2xNCN}$ CT
S_5, 2.331	0.0007	HOMO→LUMO+2 (0.70)	$M^{Ir1/Ir2}L^{CNC1/CNC2}$CT/$L^{2xNCN}L^{CNC1/CNC2}$CT
S_6, 2.370	0.0002	HOMO−1→LUMO+1 (0.54) HOMO→LUMO+3 (−0.42)	$M^{Ir1/Ir2}L^{2xNCN}$ CT/ LC^{2xNCN}
S_7, 2.409	0.0602	HOMO−3→LUMO (0.66)	$M^{Ir1/Ir2}L^{2xNCN}$ CT/ $L^{CNC1/CNC2}L^{2xNCN}$ CT
S_8, 2.430	0.0001	HOMO→LUMO+4 (0.70)	$M^{Ir1/Ir2}L^{CNC1/CNC2}$CT/$L^{2xNCN}L^{CNC1/CNC2}$CT
S_9, 2.512	0.0157	HOMO→LUMO+3 (0.54) HOMO−1→LUMO+1 (0.38)	$M^{Ir1/Ir2}L^{2xNCN}$ CT/ LC^{2xNCN}
S_{10}, 2.590	0.0002	HOMO−1→LUMO+3 (0.19) HOMO→LUMO+5 (0.67)	$M^{Ir1/Ir2}L^{2xNCN}$CT/$M^{Ir1/Ir2}L^{CNC1/CNC2}$CT/ $L^{2xNCN}L^{CNC1/CNC2}$CT/ LC^{2xNCN}
S_{11}, 2.602	0.0002	HOMO−1→LUMO+2 (0.70)	$M^{Ir1/Ir2}L^{2xNCN}$CT/$L^{2xNCN}L^{CNC1/CNC2}$CT

*Square of the given coefficient multiplied by two gives percentage contribution of the corresponding transition to formation of the excited state.

**MLCT – Metal (M) to Ligand (L) Charge Transfer. LC−Ligand Centered. LLCT – Ligand to Ligand Charge Transfer.

2xNCN stands for N^C^N−N^C^N (bridging) ligand and CNC stand for C^N^C coordinating ligand.

Table 8.18. The key structural parameters of **IrPt** derived from single crystal XRD experiment and DFT optimized ground state (S_0) and T_1 state geometries of model complex **IrPt'**. The atom numbering corresponds to that given in Figure 5.1. esd – estimated standard deviation. (cf. ref.[61])

Parameter	XRD (esd)	DFT	
		Ground state (S_0)	Emitting state (T_1)
Bond length (Å)			
Pt−C1	1.966(6)	1.978	1.982
Pt−N1	1.996(4)	2.030	2.017
Pt−O1	2.010(4)	2.035	2.049
Pt−O2	2.094(5)	2.150	2.177
Ir−C7	1.997(6)	1.994	1.970
Ir−C8	1.995(5)	1.997	1.991
Ir−N2	2.042(5)	2.068	2.056
Ir−N3	2.038(5)	2.055	2.071
Ir−O3	2.145(4)	2.190	2.179
Ir−O4	2.158(4)	2.186	2.171
Bond angle (°)			
C1−Pt−N1	81.0(2)	80.854	81.129
C1−Pt−O1	93.4(3)	93.639	94.003
C1−Pt−O2	175.0(2)	175.896	175.891
N1−Pt−O1	173.3(2)	174.492	175.095
O1−Pt−O2	91.6(2)	90.449	89.661
C7−Ir−N2	80.2(2)	80.379	82.193
C7−Ir−N3	94.7(2)	97.657	96.973
C7−Ir−O4	175.1(2)	175.945	172.460
C7−Ir−O3	87.9(2)	91.969	91.064
C7−Ir−C8	92.2(2)	89.939	94.612
N2−Ir−C8	93.8(2)	98.366	98.130
N2−Ir−N3	172.11(18)	177.618	178.400
N2−Ir−O3	89.14(16)	85.399	86.636
N2−Ir−O4	96.42(16)	95.795	92.544
C8−Ir−N3	80.3(2)	80.238	80.560
C8−Ir−O3	177.0(2)	176.021	173.028
C8−Ir−O4	91.64(19)	91.960	91.465
O3−Ir−O4	88.44(16)	86.358	83.209
Torsion angle (°)			
O1−Pt−C1−C2	172.8(4)	179.802	177.202
O2−Pt−N1−C3	176.9(4)	179.472	175.204
C6−C7−Ir−C8	98.9(5)	101.788	103.586
C5−N2−Ir−N3	52.3(15)	38.466	65.518
C6−C7−Ir−O3	84.0(4)	81.704	80.465
C5−N2−Ir−O4	173.7(4)	174.704	167.711
N2−Ir−O3−C14	102.6(5)	94.023	72.811
N2−Ir−O4−C15	99.5(5)	86.713	63.604

Table 8.19. DFT calculated frontier orbital energy levels and atomic contributions of complex **IrPt'** resulting from Mulliken population analysis in the lowest triplet state (T_1) geometry. (cf. ref.[61])

Orbital	Energy, (eV)	Contribution (Mulliken), (%)					
		Pt	Ir	dpp1[a]	dpp2[b]	acac1[c]	acac2[d]
LUMO+4	−1.700	3	0	4	0	92	2
LUMO+3	−2.048	0	1	11	87	1	0
LUMO+2	−2.170	1	1	83	12	2	1
LUMO+1	−2.651	0	4	1	94	0	1
LUMO	−2.940	5	5	89	1	1	1
HOMO	−4.635	2	42	25	20	1	10
HOMO−1	−4.957	3	40	11	7	0	39
HOMO−2	−5.179	35	4	31	1	26	3
HOMO−3	−5.297	33	20	19	6	15	7
HOMO−4	−5.413	91	0	6	0	3	0

dpp1 – Pt(II)/Ir(III) two−coordinated diphenylpyrimidine

dpp2 – Ir(III) mono−coordinated diphenylpyrimidine

acac1 – Pt(II) coordinated acetylacetonate

acac2 – Ir(III) coordinated acetylacetonate

Table 8.20 TD-DFT calculated lowest triplet and singlet states of **IrPt'** in the T_1 state geometry. (cf. ref.[61])

State, Energy (eV)	*f* (oscillator strength)	Contributing transition coefficients*	Character**
triplets			
T_1, 1.615	(triplet)	HOMO→LUMO (0.70)	$M^{Ir(III)/Pt(II)}L^{dpp1}CT/L^{dpp2}L^{dpp1}CT/LC^{dpp1}$
T_2, 1.921	(triplet)	HOMO−1→LUMO (0.68) HOMO−3→LUMO (0.16)	$M^{Ir(III)/Pt(II)}L^{dpp1}CT$
T_3, 1.931	(triplet)	HOMO→LUMO+1 (0.70)	$M^{Ir(III)}L^{dpp2}CT/L^{dpp1}L^{dpp2}CT/LC^{dpp2}$
singlets			
S_1, 1.805	0.1058	HOMO→LUMO (0.69) HOMO−1→LUMO (0.12)	$M^{Ir(III)/Pt(II)}L^{dpp1}CT$
S_2, 2.028	0.0203	HOMO→LUMO+1 (0.70)	$M^{Ir(III)}L^{dpp2}CT/L^{dpp1}L^{dpp2}CT/LC^{dpp2}$
S_3, 2.088	0.0707	HOMO→LUMO (−0.11) HOMO−1→LUMO (0.68) HOMO−3→LUMO (−0.10)	$M^{Ir(III)/Pt(II)}L^{dpp1}CT$
S_4, 2.348	0.1126	HOMO−1→LUMO+1 (−0.17) HOMO−2→LUMO (0.61) HOMO−3→LUMO (−0.30)	$M^{Ir(III)/Pt(II)}L^{dpp1}CT/M^{Ir(III)/Pt(II)}L^{dpp2}CT$
S_5, 2.360	0.0362	HOMO−1→LUMO+1 (0.66) HOMO−2→LUMO (−0.15)	$M^{Ir(III)/Pt(II)}L^{dpp2}CT/$ $M^{Ir(III)/Pt(II)}L^{dpp1}CT$
S_6, 2.476	0.0497	HOMO−4→LUMO (0.49) HOMO−3→LUMO (0.41) HOMO−2→LUMO (0.20) HOMO→LUMO+2 (−0.20)	$M^{Ir(III)}L^{dpp1}CT/L^{acac1}L^{dpp1}CT$
S_7, 2.484	0.0469	HOMO−4→LUMO (0.50) HOMO−3→LUMO (−0.40) HOMO−2→LUMO (−0.17) HOMO→LUMO+2 (0.21)	$M^{Ir(III)}L^{dpp1}CT/L^{acac1}L^{dpp1}CT$
S_8, 2.505	0.0319	HOMO−3→LUMO (0.25) HOMO−2→LUMO (0.13) HOMO→LUMO+2 (0.63)	$M^{Ir(III)}L^{dpp1}CT/L^{acac1}L^{dpp1}CT$
S_9, 2.532	0.0045	HOMO−2→LUMO+1 (0.70)	$M^{Ir(III)/Pt(II)}L^{dpp2}CT/L^{dpp1}L^{dpp2}CT/L^{acac1}L^{dpp2}CT$
S_{10}, 2.575	0.0352	HOMO−5→LUMO (0.659)	$M^{Ir(III)/Pt(II)}L^{dpp1}CT$

*Square of the coefficient multiplied by two gives percentage contribution of the transition to formation of the excited state

** MLCT – Metal (M) to Ligand (L) Charge Transfer. LC−Ligand Centered. LLCT – Ligand to Ligand Charge Transfer.

References and notes

1. Valeur, B.; Berberan-Santos, M. N., A Brief History of Fluorescence and Phosphorescence before the Emergence of Quantum Theory. *J. Chem. Educ.* **2011,** *88* (6), 731-738.

2. Dirac, P. A. M., The Quantum Theory of the Emission and Absorption of Radiation. *Proceedings of the Royal Society of London A: Mathematical, Physical and Engineering Sciences* **1927,** *114* (767), 243-265.

3. Hilborn, R. C., Einstein coefficients, cross sections, f values, dipole moments, and all that. *Am. J. Phys.* **1982,** *50* (11), 982-986.

4. Kasha, M., Characterization of electronic transitions in complex molecules. *Disc. Faraday Soc.* **1950,** *9* (0), 14-19.

5. Stokes, G. G., On the Change of Refrangibility of Light. *Philos. Trans.* **1852,** *142*, 463–562.

6. Tang, C. W.; VanSlyke, S. A., Organic electroluminescent diodes. *Appl. Phys. Lett.* **1987,** *51* (12), 913-915.

7. Baldo, M. A.; O'Brien, D. F.; You, Y.; Shoustikov, A.; Sibley, S.; Thompson, M. E.; Forrest, S. R., Highly efficient phosphorescent emission from organic electroluminescent devices. *Nature* **1998,** *395* (6698), 151-154.

8. Turro, N. J.; Ramamurthy, V.; Scaiano, J. C., Spin-Orbit Coupling: A Dominant Mechanism for Inducing Spin Changes in Organic Molecules. In *Modern Molecular Photochemistry of Organic Molecules*, University Science Books: Saisalito, 2010; pp 149-156.

9. Zhen, X.; Qu, R.; Chen, W.; Wu, W.; Jiang, X., The development of phosphorescent probes for in vitro and in vivo bioimaging. *Biomater. Sci.* **2021,** *9* (2), 285-300.

10. Shiu, H.-Y.; Chong, H.-C.; Leung, Y.-C.; Zou, T.; Che, C.-M., Phosphorescent proteins for bio-imaging and site selective bio-conjugation of peptides and proteins with luminescent cyclometalated iridium(III) complexes. *Chem. Commun.* **2014,** *50* (33), 4375-4378.

11. Chen, Y.; Xu, W.; Zuo, J.; Ji, L.; Chao, H., Dinuclear iridium(III) complexes as phosphorescent trackers to monitor mitochondrial dynamics. *J. Mater. Chem. B* **2015,** *3* (16), 3306-3314.

12. Solomatina, A. I.; Su, S.-H.; Lukina, M. M.; Dudenkova, V. V.; Shcheslavskiy, V. I.; Wu, C.-H.; Chelushkin, P. S.; Chou, P.-T.; Koshevoy, I. O.; Tunik, S. P., Water-soluble cyclometalated platinum(II) and iridium(III) complexes: synthesis, tuning of the photophysical properties, and in vitro and in vivo phosphorescence lifetime imaging. *RSC Adv.* **2018,** *8* (31), 17224-17236.

13. Zhang, P.; Huang, H.; Banerjee, S.; Clarkson, G. J.; Ge, C.; Imberti, C.; Sadler, P. J., Nucleus-Targeted Organoiridium–Albumin Conjugate for Photodynamic Cancer Therapy. *Angew. Chem. Int. Ed.* **2019,** *58* (8), 2350-2354.

14. Yersin, H.; Rausch, A. F.; Czerwieniec, R.; Hofbeck, T.; Fischer, T., The triplet state of organo-transition metal compounds. Triplet harvesting and singlet harvesting for efficient OLEDs. *Coord. Chem. Rev.* **2011,** *255* (21-22), 2622-2652.

15. Englman, R.; Jortner, J., The energy gap law for radiationless transitions in large molecules. *Mol. Phys.* **1970,** *18* (2), 145-164.

16. Yang, X.; Xu, X.; Dang, J.-s.; Zhou, G.; Ho, C.-L.; Wong, W.-Y., From Mononuclear to Dinuclear Iridium(III) Complex: Effective Tuning of the Optoelectronic Characteristics for Organic Light-Emitting Diodes. *Inorg. Chem.* **2016,** *55* (4), 1720-1727.

17. Daniels, R. E.; Culham, S.; Hunter, M.; Durrant, M. C.; Probert, M. R.; Clegg, W.; Williams, J. A.; Kozhevnikov, V. N., When two are better than one: bright phosphorescence from non-stereogenic dinuclear iridium(III) complexes. *Dalton Trans.* **2016,** *45* (16), 6949-6962.

18. Griffith, J. S., Magnetic Effects in Atomic Structure. In *The Theory of Transition-Metal Ions*, Cambridge University Press: 1964; pp 106-128.

19. Shafikov, M. Z.; Daniels, R.; Kozhevnikov, V. N., Unusually Fast Phosphorescence from Ir(III) Complexes via Dinuclear Molecular Design. *J. Phys. Chem. Lett.* **2019,** *10* (22), 7015-7024.

20. Wilkinson, A. J.; Puschmann, H.; Howard, J. A. K.; Foster, C. E.; Williams, J. A. G., Luminescent Complexes of Iridium(III) Containing N^C^N-Coordinating Terdentate Ligands. *Inorg. Chem.* **2006,** *45* (21), 8685-8699.

21. Finkenzeller, W. J.; Yersin, H., Emission of $Ir(ppy)_3$. Temperature dependence, decay dynamics, and magnetic field properties. *Chem. Phys. Lett.* **2003,** *377* (3-4), 299-305.

22. Mak, C. S. K.; Pentlehner, D.; Stich, M.; Wolfbeis, O. S.; Chan, W. K.; Yersin, H., Exceptional Oxygen Sensing Capabilities and Triplet State Properties of $Ir(ppy\text{-}NPh_2)_3$. *Chem. Mater.* **2009,** *21* (11), 2173-2175.

23. Hofbeck, T.; Yersin, H., The Triplet State of *fac*-$Ir(ppy)_3$. *Inorg. Chem.* **2010,** *49* (20), 9290-9299.

24. Rausch, A. F.; Homeier, H. H. H.; Yersin, H., Organometallic Pt(II) and Ir(III) triplet emitters for OLED applications and the role of spin-orbit coupling: A study based on high-resolution optical spectroscopy. *Top. Organomet. Chem.* **2010,** *29*, 193-235.

25. Rausch, A. F.; Thompson, M. E.; Yersin, H., Matrix effects on the triplet state of the OLED emitter $Ir(4,6\text{-}dFppy)_2(pic)$ (FIrpic): investigations by high-resolution optical spectroscopy. *Inorg. Chem.* **2009,** *48* (5), 1928-1937.

26. Rausch, A. F.; Murphy, L.; Williams, J. A. G.; Yersin, H., Probing the Excited State Properties of the Highly Phosphorescent Pt(dpyb)Cl Compound by High-Resolution Optical Spectroscopy. *Inorg. Chem.* **2009,** *48* (23), 11407-11414.

27. Finkenzeller, W. J.; Thompson, M. E.; Yersin, H., Phosphorescence dynamics and spin-lattice relaxation of the OLED emitter $Ir(btp)_2(acac)$. *Chem. Phys. Lett.* **2007,** *444* (4-6), 273-279.

28. Czerwieniec, R.; Finkenzeller, W. J.; Hofbeck, T.; Starukhin, A.; Wedel, A.; Yersin, H., Photophysical properties of $Re(pbt)(CO)_4$ studied by high resolution spectroscopy. *Chem. Phys. Lett.* **2009,** *468* (4–6), 205-210.

29. Azumi, T.; O'Donnell, C. M.; McGlynn, S. P., On the multiplicity of the phosphorescent state of organic molecules. *J. Chem. Phys.* **1966,** *45* (8), 2735-2742.

30. Hager, G. D.; Crosby, G. A., Charge-transfer exited states of Ruthenium(II) complexes. I. Quantum yield and decay measurements. *J. Amer. Chem. Soc.* **1975,** *97* (24), 7031-7037.

31. Baryshnikov, G.; Minaev, B.; Ågren, H., Theory and Calculation of the Phosphorescence Phenomenon. *Chem. Rev.* **2017,** *117* (9), 6500-6537.

32. Minaev, B.; Baryshnikov, G.; Agren, H., Principles of phosphorescent organic light emitting devices. *Phys. Chem. Chem. Phys.* **2014,** *16* (5), 1719-1758.

33. Montalti, M.; Credi, A.; Prodi, L.; Gandolfi, M. T., *Handbook of Photochemistry, 3rd Ed.* CRC Press: 2006; p 633.

34. El-Sayed, M. A., Spin-Orbit Coupling and the Radiationless Processes in Nitrogen Heterocyclics. *J. Chem. Phys.* **1963,** *38* (12), 2834-2838.

35. Song, J.; Kim, K.-H.; Kim, E.; Moon, C.-K.; Kim, Y.-H.; Kim, J.-J.; Yoo, S., Lensfree OLEDs with over 50% external quantum efficiency via external scattering and horizontally oriented emitters. *Nat. Commun.* **2018,** *9* (1), 3207.

36. Tan, G.; Chen, S.; Sun, N.; Li, Y.; Fortin, D.; Wong, W.-Y.; Kwok, H.-S.; Ma, D.; Wu, H.; Wang, L.; Harvey, P. D., Highly efficient iridium(III) phosphors with phenoxy-substituted ligands and their high-performance OLEDs. *J. Mater. Chem. C* **2013,** *1* (4), 808-821.

37. Tang, M. C.; Chan, A. K. W.; Chan, M. Y.; Yam, V. W. W., Platinum and Gold Complexes for OLEDs. *Top. Curr. Chem.* **2016,** *374*.

38. Cui, L.-S.; Liu, Y.; Liu, X.-Y.; Jiang, Z.-Q.; Liao, L.-S., Design and Synthesis of Pyrimidine-Based Iridium(III) Complexes with Horizontal Orientation for Orange and White Phosphorescent OLEDs. *ACS Appl. Mater. Interfaces* **2015,** *7* (20), 11007-11014.

39. Cherpak, V.; Stakhira, P.; Minaev, B.; Baryshnikov, G.; Stromylo, E.; Helzhynskyy, I.; Chapran, M.; Volyniuk, D.; Tomkuté-Lukšiené, D.; Malinauskas, T.; Getautis, V.; Tomkeviciene, A.; Simokaitiene, J.; Grazulevicius, J. V., Efficient "warm-white" OLEDs based

on the phosphorescent bis-cyclometalated iridium(III) complex. *J. Phys. Chem. C* **2014,** *118* (21), 11271-11278.

40. Gildea, L. F.; Williams, J. A. G., Iridium and Platunum Complexes for OLEDs. In *Organic light-emitting diodes: materials, devices and applications*, A., B., Ed. Woodhead Publishing: Cambridge, 2013; pp 77-113.

41. Lamansky, S.; Kwong, R. C.; Nugent, M.; Djurovich, P. I.; Thompson, M. E., Molecularly doped polymer light emitting diodes utilizing phosphorescent Pt(II) and Ir(III) dopants. *Org. Electron.* **2001,** *2* (1), 53-62.

42. Adachi, C.; Baldo, M. A.; Forrest, S. R.; Lamansky, S.; Thompson, M. E.; Kwong, R. C., High-efficiency red electrophosphorescence devices. *Appl. Phys. Lett.* **2001,** *78* (11), 1622-1624.

43. Baldo, M. A.; Lamansky, S.; Burrows, P. E.; Thompson, M. E.; Forrest, S. R., Very high-efficiency green organic light-emitting devices based on electrophosphorescence. *Appl. Phys. Lett.* **1999,** *75* (1), 4-6.

44. Tsutsui, T.; Yang, M.-J.; Yahiro, M.; Nakamura, K.; Watanabe, T.; Tsuji, T.; Fukuda, Y.; Wakimoto, T.; Miyaguchi, S., High Quantum Efficiency in Organic Light-Emitting Devices with Iridium-Complex as a Triplet Emissive Center. *Jpn. J. Appl. Phys.* **1999,** *38* (Part 2, No. 12B), L1502-L1504.

45. Adachi, C.; Baldo, M. A.; Forrest, S. R.; Thompson, M. E., High-efficiency organic electrophosphorescent devices with tris(2-phenylpyridine)iridium doped into electron-transporting materials. *Appl. Phys. Lett.* **2000,** *77* (6), 904-906.

46. Lee, C.-L.; Lee, K. B.; Kim, J.-J., Polymer phosphorescent light-emitting devices doped with tris(2-phenylpyridine) iridium as a triplet emitter. *Appl. Phys. Lett.* **2000,** *77* (15), 2280-2282.

47. Liao, J. L.; Rajakannu, P.; Gnanasekaran, P.; Tsai, S. R.; Lin, C. H.; Liu, S. H.; Chang, C. H.; Lee, G. H.; Chou, P. T.; Chen, Z. N.; Chi, Y., Luminescent Diiridium Complexes with Bridging Pyrazolates: Characterization and Fabrication of OLEDs Using Vacuum Thermal Deposition. *Adv. Opt. Mater.* **2018,** *6* (11), 1800083.

48. Shi, S.; Jung, M. C.; Coburn, C.; Tadle, A.; Sylvinson M. R, D.; Djurovich, P. I.; Forrest, S. R.; Thompson, M. E., Highly Efficient Photo- and Electroluminescence from Two-Coordinate Cu(I) Complexes Featuring Nonconventional N-Heterocyclic Carbenes. *J. Am. Chem. Soc.* **2019,** *141* (8), 3576-3588.

49. Shafikov, M. Z.; Suleymanova, A. F.; Czerwieniec, R.; Yersin, H., Design Strategy for Ag(I)-Based Thermally Activated Delayed Fluorescence Reaching an Efficiency Breakthrough. *Chem. Mater.* **2017,** *29* (4), 1708-1715.

50. Shafikov, M. Z.; Suleymanova, A. F.; Czerwieniec, R.; Yersin, H., Thermally Activated Delayed Fluorescence from Ag(I) Complexes: A Route to 100% Quantum Yield at Unprecedentedly Short Decay Time. *Inorg. Chem.* **2017,** *56* (21), 13274-13285.

51. Shafikov, M. Z.; Suleymanova, A. F.; Schinabeck, A.; Yersin, H., Dinuclear Ag(I) complex designed for highly efficient thermally activated delayed fluorescence. *J. Phys. Chem. Lett.* **2018,** *9*, 702-709.

52. Wallesch, M.; Volz, D.; Zink, D. M.; Schepers, U.; Nieger, M.; Baumann, T.; Bräse, S., Bright Coppertunities: Multinuclear Cu^{I} Complexes with N–P Ligands and Their Applications. *Chem. Eur. J.* **2014,** *20* (22), 6578-6590.

53. Leitl, M. J.; Krylova, V. A.; Djurovich, P. I.; Thompson, M. E.; Yersin, H., Phosphorescence versus Thermally Activated Delayed Fluorescence. Controlling Singlet-Triplet Splitting in Brightly Emitting and Sublimable Cu(I) Compounds. *J. Am. Chem. Soc.* **2014,** *136* (45), 16032-16038.

54. Hofbeck, T.; Monkowius, U.; Yersin, H., Highly Efficient Luminescence of Cu(I) Compounds: Thermally Activated Delayed Fluorescence Combined with Short-Lived Phosphorescence. *J. Am. Chem. Soc.* **2015,** *137* (1), 399-404.

55. Hamze, R.; Peltier, J. L.; Sylvinson, D.; Jung, M.; Cardenas, J.; Haiges, R.; Soleilhavoup, M.; Jazzar, R.; Djurovich, P. I.; Bertrand, G.; Thompson, M. E., Eliminating nonradiative decay in Cu(I) emitters: >99% quantum efficiency and microsecond lifetime. *Science* **2019,** *363* (6427), 601.

56. Volz, D.; Chen, Y.; Wallesch, M.; Liu, R.; Fléchon, C.; Zink, D. M.; Friedrichs, J.; Flügge, H.; Steininger, R.; Göttlicher, J.; Heske, C.; Weinhardt, L.; Bräse, S.; So, F.; Baumann, T., Bridging the Efficiency Gap: Fully Bridged Dinuclear Cu(I)-Complexes for Singlet Harvesting in High-Efficiency OLEDs. *Adv. Mater.* **2015,** *27* (15), 2538-2543.

57. Zeng, W.; Zhou, T.; Ning, W.; Zhong, C.; He, J.; Gong, S.; Xie, G.; Yang, C., Realizing 22.5% External Quantum Efficiency for Solution-Processed Thermally Activated Delayed-Fluorescence OLEDs with Red Emission at 622 nm via a Synergistic Strategy of Molecular Engineering and Host Selection. *Adv. Mater.* **2019**, e1901404.

58. Hamze, R.; Shi, S.; Kapper, S. C.; Muthiah Ravinson, D. S.; Estergreen, L.; Jung, M.-C.; Tadle, A. C.; Haiges, R.; Djurovich, P. I.; Peltier, J. L.; Jazzar, R.; Bertrand, G.; Bradforth, S. E.; Thompson, M. E., "Quick-Silver" from a Systematic Study of Highly Luminescent, Two-Coordinate, d^{10} Coinage Metal Complexes. *J. Am. Chem. Soc.* **2019,** *141* (21), 8616-8626.

59. Shafikov, M. Z.; Zaytsev, A. V.; Kozhevnikov, V. N., Halide-Enhanced Spin–Orbit Coupling and the Phosphorescence Rate in Ir(III) Complexes. *Inorg. Chem.* **2021,** *60* (2), 642–650.

60. Lanoë, P.-H.; Tong, C. M.; Harrington, R. W.; Probert, M. R.; Clegg, W.; Williams, J. A. G.; Kozhevnikov, V. N., Ditopic bis-terdentate cyclometallating ligands and their highly luminescent dinuclear iridium(III) complexes. *Chem. Commun.* **2014,** *50* (52), 6831-6834.

61. Shafikov, M. Z.; Tang, S.; Larsen, C.; Bodensteiner, M.; Kozhevnikov, V. N.; Edman, L., An Efficient Heterodinuclear Ir(III)/Pt(II) Complex: Synthesis, Photophysics and Application in Light-Emitting Electrochemical Cells. *J. Mater. Chem. C* **2019,** *7* (34), 10672-10682.

62. Shafikov, M. Z.; Daniels, R.; Pander, P.; Dias, F. B.; Williams, J. A. G.; Kozhevnikov, V. N., Dinuclear Design of a Pt(II) Complex Affording Highly Efficient Red Emission: Photophysical Properties and Application in Solution-Processible OLEDs. *ACS Appl. Mater. Interfaces* **2019,** *11* (8), 8182-8193.

63. Yersin, H.; Czerwieniec, R.; Shafikov, M. Z.; Suleymanova, A. F., TADF Material Design: Photophysical Background and Case Studies Focusing on Cu(I) and Ag(I) Complexes. *ChemPhysChem* **2017,** *18* (24), 3508-3535.

64. Czerwieniec, R.; Leitl, M. J.; Homeier, H. H. H.; Yersin, H., Cu(I) complexes – Thermally activated delayed fluorescence. Photophysical approach and material design. *Coord. Chem. Rev.* **2016,** *325*, 2-28.

65. Azumi, T.; Miki, H., Spectroscopy of the spin sublevels of transition metal complexes. In *Electronic and Vibronic Spectra of Transition Metal Complexes II*, Yersin, H., Ed. Springer Berlin Heidelberg: Berlin, Heidelberg, 1997; pp 1-40.

66. Yu-Tzu Li, E.; Jiang, T.-Y.; Chi, Y.; Chou, P.-T., Semi-quantitative assessment of the intersystem crossing rate: an extension of the El-Sayed rule to the emissive transition metal complexes. *Phys. Chem. Chem. Phys.* **2014,** *16* (47), 26184-26192.

67. Nozaki, K., Theoretical Studies on Photophysical Properties and Mechanism of Phosphorescence in [*fac*-Ir(2-phenylpyridine)$_3$]. *J. Chin. Chem. Soc.-TAIP* **2006,** *53* (1), 101-112.

68. Griffith, J. S., The spin-Hamiltonian. In *The Theory of Transition-Metal Ions*, Cambridge University Press: 1964; pp 330-340.

69. Shafikov, M. Z.; Zaytsev, A.; Suleymanova, A. F.; Brandl, F.; Kowalczyk, A.; Gapinska, M.; Kowalski, K.; Kozhevnikov, V. N.; Czerwieniec, R., Near Infrared Phosphorescent Dinuclear Ir(III) Complex Exhibiting Unusually Slow Intersystem Crossing and Dual Emissive Behavior. *J. Phys. Chem. Lett.* **2020,** *11* (15), 5849-5855.

70. Tsuboyama, A.; Takiguchi, T.; Okada, S.; Osawa, M.; Hoshino, M.; Ueno, K., A novel dinuclear cyclometalated iridium complex bridged with 1,4-bis[pyridine-2-yl]benzene: its structure and photophysical properties. *Dalton Trans.* **2004,** (8), 1115-1116.

71. Kozhevnikov, D. N.; Kozhevnikov, V. N.; Shafikov, M. Z.; Prokhorov, A. M.; Bruce, D. W.; Williams, J. A., Phosphorescence vs fluorescence in cyclometalated platinum(II) and iridium(III) complexes of (oligo)thienylpyridines. *Inorg. Chem.* **2011,** *50* (8), 3804-3815.

72. Hao, Z.; Li, M.; Liu, Y.; Wang, Y.; Xie, G.; Liu, Y., Near-infrared emission of dinuclear iridium complexes with hole/electron transporting bridging and their monomer in solution-processed organic light-emitting diodes. *Dye. Pigment.* **2018,** *149*, 315-322.

73. Kim, H. U.; Jang, H. J.; Choi, W.; Park, S.; Park, T.; Lee, J. Y.; Bejoymohandas, K. S., Aggregation-induced phosphorescence enhancement in deep-red and near-infrared emissive iridium(III) complexes for solution-processable OLEDs. *J. Mater. Chem. C* **2020,** *8* (14), 4789-4800.

74. Palmer, J. H.; Durrell, A. C.; Gross, Z.; Winkler, J. R.; Gray, H. B., Near-IR Phosphorescence of Iridium(III) Corroles at Ambient Temperature. *J. Am. Chem. Soc.* **2010,** *132* (27), 9230-9231.

75. Kritchenkov, I. S.; Chelushkin, P. S.; Sokolov, V. V.; Pavlovskiy, V. V.; Porsev, V. V.; Evarestov, R. A.; Tunik, S. P., Near-Infrared $[Ir(N^C)_2(N^N)]^+$ Emitters and Their Noncovalent Adducts with Human Serum Albumin: Synthesis and Photophysical and Computational Study. *Organomet.* **2019,** *38* (19), 3740-3751.

76. Wang, L.; Yin, H.; Cui, P.; Hetu, M.; Wang, C.; Monro, S.; Schaller, R. D.; Cameron, C. G.; Liu, B.; Kilina, S.; McFarland, S. A.; Sun, W., Near-infrared-emitting heteroleptic cationic iridium complexes derived from 2,3-diphenylbenzo[*g*]quinoxaline as in vitro theranostic photodynamic therapy agents. *Dalton Trans.* **2017,** *46* (25), 8091-8103.

77. Kautsky, H., Quenching of luminescence by oxygen. *Trans. Faraday Soc.* **1939,** *35* (0), 216-219.

78. Kearns, D. R.; Khan, A. U., Sensitized Photooxygenation Reactions and the Role of Singlet Oxygen. *Photochem. Photobiol.* **1969,** *10* (3), 193-210.

79. Shafikov, M. Z.; Kozhevnikov, D. N.; Bodensteiner, M.; Brandl, F.; Czerwieniec, R., Modulation of Intersystem Crossing Rate by Minor Ligand Modifications in Cyclometalated Platinum(II) Complexes. *Inorg. Chem.* **2016,** *55* (15), 7457-7466.

80. Hsu, C.-C.; Lin, C.-C.; Chou, P.-T.; Lai, C.-H.; Hsu, C.-W.; Lin, C.-H.; Chi, Y., Harvesting Highly Electronically Excited Energy to Triplet Manifolds: State-Dependent Intersystem Crossing Rate in Os(II) and Ag(I) Complexes. *J. Am. Chem. Soc.* **2012,** *134* (18), 7715-7724.

81. Kutta, R.-J.; Langenbacher, T.; Kensy, U.; Dick, B., Setup and performance of a streak camera apparatus for transient absorption measurements in the ns to ms range. *Appl. Phys. B* **2013,** *111* (2), 203-216.

82. Kutta, R.-J.; Kensy, U.; Dick, B., Transient Absorption. In *Chemical Photocatalysis*, König, B., Ed. De Gruyter: Leipzig, 2013; pp 295–318.

83. Hedley, G. J.; Ruseckas, A.; Samuel, I. D. W., Ultrafast Intersystem Crossing in a Red Phosphorescent Iridium Complex. *J. Phys. Chem. A* **2009,** *113* (1), 2-4.

84. Tang, K.-C.; Liu, K. L.; Chen, I. C., Rapid intersystem crossing in highly phosphorescent iridium complexes. *Chem. Phys. Lett.* **2004,** *386* (4–6), 437-441.

85. Hedley, G. J.; Ruseckas, A.; Samuel, I. D. W., Ultrafast luminescence in $Ir(ppy)_3$. *Chem. Phys. Lett.* **2008,** *450* (4), 292-296.

86. Messina, F.; Pomarico, E.; Silatani, M.; Baranoff, E.; Chergui, M., Ligand-Centred Fluorescence and Electronic Relaxation Cascade at Vibrational Time Scales in Transition-Metal Complexes. *J. Phys.Chem. Lett.* **2015,** *6* (22), 4475-4480.

87. Pomarico, E.; Silatani, M.; Messina, F.; Braem, O.; Cannizzo, A.; Barranoff, E.; Klein, J. H.; Lambert, C.; Chergui, M., Dual Luminescence, Interligand Decay, and Nonradiative Electronic Relaxation of Cyclometalated Iridium Complexes in Solution. *J. Phys. Chem. C* **2016,** *120* (30), 16459-16469.

88. Chen, T.; Zheng, L.; Yuan, J.; An, Z.; Chen, R.; Tao, Y.; Li, H.; Xie, X.; Huang, W., Understanding the Control of Singlet-Triplet Splitting for Organic Exciton Manipulating: A Combined Theoretical and Experimental Approach. *Sci. Rep.* **2015,** *5* (1), 10923.

89. Schmidt, K.; Brovelli, S.; Coropceanu, V.; Beljonne, D.; Cornil, J.; Bazzini, C.; Caronna, T.; Tubino, R.; Meinardi, F.; Shuai, Z.; Brédas, J.-L., Intersystem Crossing Processes in Nonplanar Aromatic Heterocyclic Molecules. *J. Phys. Chem. A* **2007,** *111* (42), 10490-10499.

90. Brédas, J.-L.; Beljonne, D.; Coropceanu, V.; Cornil, J., Charge-Transfer and Energy-Transfer Processes in π-Conjugated Oligomers and Polymers: A Molecular Picture. *Chem. Rev.* **2004,** *104* (11), 4971-5004.

91. Shafikov, M. Z.; Martinscroft, R.; Hodgson, C.; Hayer, A.; Auch, A.; Kozhevnikov, V. N., Non-Stereogenic Dinuclear Ir(III) Complex with a Molecular Rack Design to Afford Efficient Thermally Enhanced Red Emission. *Inorg. Chem.* **2021,** *60* (3), 1780-1789.

92. Shafikov, M. Z.; Pander, P.; Zaytsev, A. V.; Daniels, R.; Martinscroft, R.; Dias, F. B.; Williams, J. A. G.; Kozhevnikov, V. N., Extended ligand conjugation and dinuclearity as a route to efficient platinum-based near-infrared (NIR) triplet emitters and solution-processed NIR-OLEDs. *J. Mater. Chem. C* **2021,** *9*, 127-135.

93. Sajoto, T.; Djurovich, P. I.; Tamayo, A. B.; Oxgaard, J.; Goddard, W. A.; Thompson, M. E., Temperature Dependence of Blue Phosphorescent Cyclometalated Ir(III) Complexes. *J. Am. Chem. Soc.* **2009,** *131* (28), 9813-9822.

94. Sun, Q.; Mosquera-Vazquez, S.; Lawson Daku, L. M.; Guénée, L.; Goodwin, H. A.; Vauthey, E.; Hauser, A., Experimental Evidence of Ultrafast Quenching of the ^{3}MLCT Luminescence in Ruthenium(II) Tris-bipyridyl Complexes via a ^{3}dd State. *J. Am. Chem. Soc.* **2013,** *135* (37), 13660-13663.

95. Zhou, X.; Burn, P. L.; Powell, B. J., Bond Fission and Non-Radiative Decay in Iridium(III) Complexes. *Inorg. Chem.* **2016,** *55* (11), 5266-5273.

96. Gnanasekaran, P.; Yuan, Y.; Lee, C.-S.; Zhou, X.; Jen, A. K. Y.; Chi, Y., Realization of Highly Efficient Red Phosphorescence from Bis-Tridentate Iridium(III) Phosphors. *Inorg. Chem.* **2019,** *58* (16), 10944-10954.

97. Schinabeck, A.; Rau, N.; Klein, M.; Sundermeyer, J.; Yersin, H., Deep blue emitting Cu(I) tripod complexes. Design of high quantum yield materials showing TADF-assisted phosphorescence. *Dalton Trans.* **2018**.

98. Kozhevnikov, V. N.; Durrant, M. C.; Williams, J. A. G., Highly Luminescent Mixed-Metal Pt(II)/Ir(III) Complexes: Bis-Cyclometalation of 4,6-Diphenylpyrimidine As a Versatile Route to Rigid Multimetallic Assemblies. *Inorg. Chem.* **2011,** *50* (13), 6304-6313.

99. Brooks, J.; Babayan, Y.; Lamansky, S.; Djurovich, P. I.; Tsyba, I.; Bau, R.; Thompson, M. E., Synthesis and Characterization of Phosphorescent Cyclometalated Platinum Complexes. *Inorg. Chem.* **2002,** *41* (12), 3055-3066.

100. Shavaleev, N. M.; Adams, H.; Best, J.; Edge, R.; Navaratnam, S.; Weinstein, J. A., Deep-Red Luminescence and Efficient Singlet Oxygen Generation by Cyclometalated Platinum(II) Complexes with 8-Hydroxyquinolines and Quinoline-8-thiol. *Inorg. Chem.* **2006,** *45* (23), 9410-9415.

101. Turnbull, G.; Williams, J. A. G.; Kozhevnikov, V. N., Rigidly linking cyclometallated Ir(III) and Pt(II) centres: an efficient approach to strongly absorbing and highly phosphorescent red emitters. *Chem. Commun.* **2017,** *53* (18), 2729-2732.

102. Bünzli, A. M.; Bolink, H. J.; Constable, E. C.; Housecroft, C. E.; Junquera-Hernández, J. M.; Neuburger, M.; Ortí, E.; Pertegás, A.; Serrano-Pérez, J. J.; Tordera, D.; Zampese, J. A., Thienylpyridine-based cyclometallated iridium(III) complexes and their use in solid state light-emitting electrochemical cells. *Dalton Trans.* **2014,** *43* (2), 738-750.

103. Henwood, A. F.; Zysman-Colman, E., Luminescent Iridium Complexes Used in Light-Emitting Electrochemical Cells (LEECs). *Top. Curr. Chem.* **2016,** *374*, 36.

104. Yersin, H., *Highly Efficient OLEDs with Phosphorescent Materials*. Wiley-VCH: Weinheim, 2008; p 458.

105. Dobryakov, A. L.; Kovalenko, S. A.; Weigel, A.; Pérez-Lustres, J. L.; Lange, J.; Müller, A.; Ernsting, N. P., Femtosecond pump/supercontinuum-probe spectroscopy: Optimized setup and signal analysis for single-shot spectral referencing. *Rev. Sci. Instrum.* **2010,** *81* (11), 113106.

106. Wilhelm, T.; Piel, J.; Riedle, E., Sub-20-fs pulses tunable across the visible from a blue-pumped single-pass noncollinear parametric converter. *Opt. Lett.* **1997,** *22* (19), 1494-1496.

107. Frisch, M. J.; Trucks, G. W.; Schlegel, H. B.; Scuseria, G. E.; Robb, M. A.; Cheeseman, J. R.; Scalmani, G.; Barone, V.; Mennucci, B.; Petersson, G. A.; Nakatsuji, H.; Caricato, M.; Li, X.; Hratchian, H. P.; Izmaylov, A. F.; Bloino, J.; Zheng, G.; Sonnenberg, J. L.; Hada, M.; Ehara, M.; Toyota, K.; Fukuda, R.; Hasegawa, J.; Ishida, M.; Nakajima, T.; Honda, Y.; Kitao, O.; Nakai, H.; Vreven, T.; Montgomery Jr., J. A.; Peralta, J. E.; Ogliaro, F.; Bearpark, M. J.; Heyd, J.; Brothers, E. N.; Kudin, K. N.; Staroverov, V. N.; Kobayashi, R.; Normand, J.; Raghavachari, K.; Rendell, A. P.; Burant, J. C.; Iyengar, S. S.; Tomasi, J.; Cossi, M.; Rega, N.; Millam, N. J.; Klene, M.; Knox, J. E.; Cross, J. B.; Bakken, V.; Adamo, C.; Jaramillo, J.; Gomperts, R.; Stratmann, R. E.; Yazyev, O.; Austin, A. J.; Cammi, R.; Pomelli, C.; Ochterski, J. W.; Martin, R. L.; Morokuma, K.; Zakrzewski, V. G.; Voth, G. A.; Salvador, P.; Dannenberg, J. J.; Dapprich, S.; Daniels, A. D.; Farkas, Ö.; Foresman, J. B.; Ortiz, J. V.; Cioslowski, J.; Fox, D. J., *Gaussian 09*. Gaussian, Inc.: Wallingford, CT, USA, 2009.

108. Dolomanov, O. V.; Bourhis, L. J.; Gildea, R. J.; Howard, J. A. K.; Puschmann, H., OLEX2: a complete structure solution, refinement and analysis program. *J. Appl. Cryst.* **2009,** *42* (2), 339-341.

109. Peverati, R.; Truhlar, D. G., M11-L: A Local Density Functional That Provides Improved Accuracy for Electronic Structure Calculations in Chemistry and Physics. *J. Phys. Chem. Lett.* **2012,** *3* (1), 117-124.

110. Peverati, R.; Truhlar, D. G., Performance of the M11 and M11-L density functionals for calculations of electronic excitation energies by adiabatic time-dependent density functional theory. *Phys. Chem. Chem. Phys.* **2012,** *14* (32), 11363-11370.

111. Zhao, Y.; Truhlar, D. G., The M06 suite of density functionals for main group thermochemistry, thermochemical kinetics, noncovalent interactions, excited states, and transition elements: two new functionals and systematic testing of four M06-class functionals and 12 other functionals. *Theor. Chem. Acc.* **2008,** *120* (1), 215-241.

112. Zhao, Y.; Truhlar, D. G., A new local density functional for main-group thermochemistry, transition metal bonding, thermochemical kinetics, and noncovalent interactions. *J. Chem. Phys.* **2006,** *125* (19), 194101.

113. Weigend, F.; Ahlrichs, R., Balanced basis sets of split valence, triple zeta valence and quadruple zeta valence quality for H to Rn: Design and assessment of accuracy. *Phys. Chem. Chem. Phys.* **2005,** *7* (18), 3297-3305.

114. Weigend, F., Accurate Coulomb-fitting basis sets for H to Rn. *Phys. Chem. Chem. Phys.* **2006,** *8* (9), 1057-1065.

115. Cossi, M.; Rega, N.; Scalmani, G.; Barone, V., Energies, structures, and electronic properties of molecules in solution with the C-PCM solvation model. *J. Comput. Chem.* **2003,** *24* (6), 669-681.

116. Sheldrick, G., SHELXT - Integrated space-group and crystal-structure determination. *Acta Cryst. A* **2015,** *71* (1), 3-8.

117. Burla, M. C.; Caliandro, R.; Camalli, M.; Carrozzini, B.; Cascarano, G. L.; De Caro, L.; Giacovazzo, C.; Polidori, G.; Siliqi, D.; Spagna, R., IL MILIONE: a suite of computer programs for crystal structure solution of proteins. *J. Appl. Cryst.* **2007,** *40* (3), 609-613.

118. Spek, A., PLATON SQUEEZE: a tool for the calculation of the disordered solvent contribution to the calculated structure factors. *Acta Cryst. C* **2015,** *71* (1), 9-18.

119. Uson, I.; Sheldrick, G. M., An introduction to experimental phasing of macromolecules illustrated by SHELX; new autotracing features. *Acta Cryst. D* **2018,** *74* (2), 106-116.

120. Blume, M.; Watson, R. E.; Peierls, R. E., Theory of spin-orbit coupling in atoms I. Derivation of the spin-orbit coupling constant. *Proc. R. Soc. A* **1962,** *270* (1340), 127-143.

Acknowledgements

At this point, I would like to acknowledge everyone who collaborated and helped me during my doctoral research.

My sincerest gratitude goes to…

…Dr. Rafał Czerwieniec for the opportunity to carry out this project and supervising my research.

…Prof. Dr. Hartmut Yersin for the opportunity to start my scientific carrier at the research frontline of the field of photoluminescent transition metal complexes and also for many scientific discussions and advice.

…Prof. Dr. Patrick Nürnberger and Prof. Dr. Bernhard Dick for the opportunity to work at and use the facilities of the "Institut für Physikalische und Theoretische Chemie, Universität Regensburg" and for discussions of my research results.

…Dr. Valery N. Kozhevnikov and his research group, Northumbria University (UK), for close and very fruitful collaboration and, in particular, for the synthesis of all the Ir(III) complexes investigated and discussed in this work.

…Dr. Alfiya F. Suleymanova, University of York (UK), for collaboration in design and synthesis of ditopic ligands.

…Dr. Roger-Jan Kutta and Fabian Brandl for collaboration in carrying out the transient absorption spectroscopy measurements and analysis of the obtained data.

…Prof. Dr. Konrad Kowalski and his research group, University of Łódź (Poland), for collaboration in carrying out the bio-imaging studies.

…. Dr. Michael Bodensteiner and x-ray department of the central analytical services of Universität Regensburg for carrying out the single crystal x-ray diffraction experiments.

…Prof. Dr. Dmitry N. Kozhevnikov, Ural Federal University (Russia), for acquainting me with the challenges in the field of photoluminescent materials and igniting interest in me to pursue a scientific carrier.

…Frau Andrea Nömeier and Frau Madlene von Sanden for giving me the kind assistance that I needed to carry the bureaucratic, organizational and technical aspects of my work.

…All the members of the research group for all the help and the good times that we spent together.

…My family for keeping faith in me and for the support in my endeavors.

Thank You!

Declaration

I hereby declare that the present work was carried out by myself and that I did not use any other sources or resources than those given.

Regensburg, _____

Marsel Z. Shafikov _____